Evolution and Dynamics of Cold Gas in Simulated Galaxies

Master's Thesis at the Faculty of Physics
Ludwig-Maximilians-Universität München

Submitted by
Jan Bendix Hagedorn

Supervised by
PD Dr. Klaus Dolag
Dr. Rhea-Silvia Remus
Dr. Umberto Maio

Munich, 3rd of August 2021

Entwicklung und Dynamik des kalten Gases in simulierten Galaxien

Masterarbeit an der Fakultät für Physik
Ludwig-Maximilians-Universität München

Eingereicht von
Jan Bendix Hagedorn

Betreut von
PD Dr. Klaus Dolag
Dr. Rhea-Silvia Remus
Dr. Umberto Maio

München, den 03.08.2021

Contents

1 Introduction **1**
1.1 Observational Methods of Gas Detection 1
1.2 Gas Cooling 3
1.3 Observations of Cold Gas 4
1.4 Galaxy Formation and Growth 6

2 Simulations **9**
2.1 Full Cosmological Simulation 10
2.2 Zoom Simulations 11
    2.2.1 Zoomed Initial Conditions 11
    2.2.2 Choice of Objects 12
    2.2.3 Merger Trees 12

3 The Chemical Network **15**
3.1 Hydrogen and Helium Chemistry 15
3.2 Metal Treatment 16
3.3 UV Background Radiation 19
3.4 Shielding 21

4 Cold Gas Properties in a Cosmological Context **23**
4.1 Cosmological Densities 24
4.2 Effects on Galaxy Formation and Evolution 27

5 Cold Gas Evolution in Individual Galaxies **33**
5.1 Cold Gas Content 34
5.2 Gas Distribution and Dynamics 38
5.3 Effects on Star Formation 44
5.4 Resolution Study 49
5.5 Impact of the UV Background Model 50

6 Discussion & Conclusion **53**

References **55**

List of Figures **60**

List of Tables **65**

A Asin **67**

Acknowledgements **75**

Chapter 1

Introduction

Cold dense gas is the fuel for star formation in our Universe. In the densest regions of galaxies, gas clouds exceeding the Jeans mass become unstable and collapse under their own gravity until they are fragmented into a multitude of small clumps that will eventually ignite nuclear fusion in their cores and become stars. This process arguably shapes the Universe as we experience it. Stars were the first things humans saw when they began turning their eyes to the sky. Now we know that without stars, life as we know it would never have existed in the first place, much less developed eyes to turn skyward. But when and where stars form and how they assemble into galaxies all depends on the dynamics and evolution of the cold gas from which they are born.

Understanding the complex interplay between cold gas, in particular molecular gas, and stars as they evolve over cosmic times requires the study of galaxies. They are the birthplace of stars and home to most of the cold gas in our Universe, and the evolution of their molecular gas and stellar components are tied to the physical processes at the core of cosmic star formation. Figure 1.1, taken from Tacconi et al. 2020, provides an overview of scaling relations between molecular mass, stellar mass, star formation rate, and redshift for observed galaxies. It shows for instance that the presence of molecular gas and star formation go hand in hand, and that molecular gas masses have been decreasing in the recent history of the Universe.

However, if molecular gas is necessary in driving the star formation we observe, or if it is merely produced under the same circumstances that birth stars, cannot easily be understood from these observations. Simulations of the formation and evolution of galaxies in their cosmological context can shed light on the causality at play here, if they successfully model the underlying physical principles and reproduce galaxies as we observe them. One of these principles, and a cornerstone of hydrodynamic cosmological simulations, is gas cooling, the theoretical basis of which is briefly outlined further below in Section 1.2. Throughout this thesis, and in computational astrophysics generally, simulations are compared to observational data, in order to determine their success in modeling physical processes. The following Section 1.1 is meant to provide some context for the observational data used as a reference in this work.

1.1 Observational Methods of Gas Detection

The gas in our Universe, unlike stars, does not do observers the favor of emitting vast amounts of black body radiation for easy detection. What radiation it does emit depends heavily on its composition and temperature. An additional factor, in all astronomical observations, is the distance between the observer and the source, which determines how far the emitted radiation is redshifted to higher wavelengths due to the expansion of space between the two.

Hot gas, in which particles are generally ionized, can be observed in the UV and X-ray regimes of the electromagnetic spectrum. This high energy radiation has a continuous

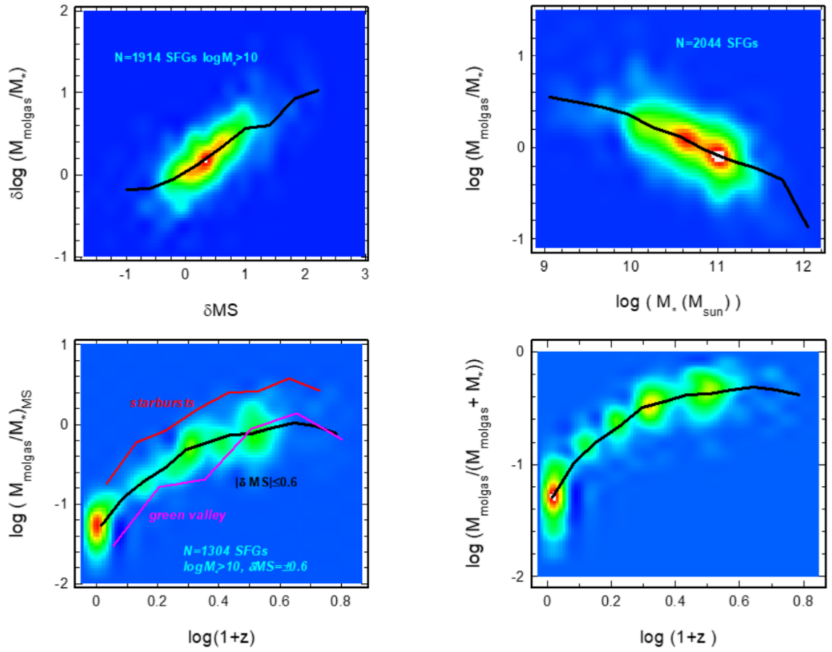

Figure 1.1: Overview of scaling relations of galactic molecular gas and stellar mass from Tacconi et al. 2020 (their Figure 5). Top left: Scaling relation of the molecular gas to stellar mass fraction M_{molgas}/M_* with the offset in specific star formation rate from the star forming main sequence of galaxies. Top right: M_{molgas}/M_* scaling relation with stellar mass. Bottom left: M_{molgas}/M_* scaling relation with redshift. Bottom right: Scaling relation of the molecular to total mass $M_{\text{molgas}}/(M_{\text{molgas}} + M_*)$ with redshift. The black lines denote the binned averages of the distributions.

and a discreet component. The former is due to free electrons either being accelerated by interactions with other charged particles in the plasma, which produces bremsstrahlung, or being captured by ions. The latter results from bound electrons transitioning between levels within an ion, which produces photons with energies equal to the difference between the two levels. Since the Earth's atmosphere absorbs high energy photons long before they reach the surface, modern X-ray telescopes are mounted on satellites and operate in orbit around Earth.

In the cold gas phase, free electrons are much rarer, and only lower energy states within atoms and molecules can be thermally excited. As a result, the cold gas emits only in discreet frequency bands, and at lower energies. Neutral atomic hydrogen, for instance, emits photons with a wavelength of 21 cm that can be detected with radio telescopes, owing to a transition between two hyper fine structure levels of its ground state that have different spin alignments between the sole proton and electron in the atom. For this low energy radiation the Earth's atmosphere is transparent, so that radio telescopes can be built on the surface of the planet, allowing for much larger structures. Prime examples are interferometric arrays consisting of many individual dishes, like the Atacama Large Millimeter Array (ALMA), or large single-dish telescopes, like the now defunct Arecibo Telescope.

Molecular gas in the Universe consists mostly of H_2 which is difficult to observe in emission at low temperatures. Due to it consisting of two identical atoms, molecular hydrogen has no permanent dipole moment, which means its higher vibrational and rotational states are difficult to excite. For this reason observed H_2 masses and densities are almost always inferred from other tracers of molecular gas, most commonly the carbon monoxide molecule (CO), which has a weak permanent dipole and thus much more accessible excited rotational and vibrational states. This creates additional uncertainties through assumptions made regarding the ratio of CO to H_2 in the molecular gas, which have to be made based on data only available for the local Universe.

A further challenge for observations in the emission spectrum of gas comes from the fact that within a gas cloud radiation is absorbed in the same narrow bands that it is emitted in. If a cloud is optically thick for a certain wavelengths, meaning the mean free path of a photon at this wavelength is smaller than the size of the cloud, then observations of the cloud's emission will only probe a comparatively thin layer on its surface. Any radiation originating from deeper within the cloud will be absorbed before emerging from the cloud to reach the observer. This means that the measured radiation intensity no longer corresponds to the amount of emitting gas in the cloud, which can be an issue for observing high density regions like molecular clouds. Observing less abundant molecules or isotopes in the gas mixture for which the cloud is not optically thick can circumvent this problem (see for example Bešlić et al. 2021).

In contrast, much of the gas in our Universe resides at very low densities, and thus faces the opposite problem. Its emission spectrum is extremely faint, making its detection a challenge. Instead, the presence and abundance of such thin gas can be determined via its absorption of radiation from background sources, such as quasars, the after glow of gamma ray bursts (Bolmer et al. 2019), fast radio bursts (Prochaska and Zheng 2019), or background galaxies (Cooke and O'Meara 2015). Such measurements probe the density of absorbing gas integrated along the line of sight to the background source, and as such are more suited for estimating global cosmic gas densities. This requires compiling measurements from many different background objects, in order to account for variations across the cosmos reflected in the individual line of sight measurements. Where the intensity of emitted radiation scales with the inverse distance from the source squared, making far away faint sources all but impossible to detect, absorption suffers from no such scaling. The sensitivity of this technique is thus not redshift dependant, which can be a great benefit in the attempt to probe high redshifts. One of the most commonly used absorption lines for this technique is the Lyman-α line, which corresponds to the electronic transition from the ground state into the first excited state in HI, and can therefore be used to trace the abundance of neutral atomic hydrogen in the Universe. For a more detailed review of gas detection through absorption features see Péroux and Howk 2020.

1.2 Gas Cooling

To facilitate its collapse, the gas has to rid itself of the thermal energy supporting it against its own gravitational pull. At the extremely low densities most of the gas in the Universe resides at, the only way to effectively shed energy is the emission of radiation. Two colliding gas particles may transfer energy from one to the other, lifting it to an excited state. When this state decays via the emission of a photon, there is a chance for this photon to escape the gas cloud and in doing so remove some of its thermal energy. Of course the inverse process of a gas particle capturing a photon from outside the cloud and distributing its energy via collisions is also possible. Which of these processes dominates, cooling or heating, ultimately decides if a cloud can collapse into stars or if it is dispersed by radiation.

Atomic hydrogen accounts for over 90% of the gas in the Universe. At temperatures above 10^4 K, it can be thermally excited and act as an effective coolant. In the cold gas, however, at temperatures below 10^4 K, the energy of the average gas particle collision becomes too low to excite the hydrogen atoms, and it ceases to cool the gas any further. For stars to form, other gas species have to take over in the cooling process. Molecules in particular are much easier to excite because their more complex geometry allows for vibrational and rotational modes with energies relatively close to the ground state. As can be expected from the abundance of hydrogen, the most common species of molecular gas in the Universe are the hydrogen molecule (H_2) and the hydrogen-deuterium molecule (HD). Next to the hydrogen based molecules, atoms of much heavier elements, also called metals in astrophysics, play an important part in gas cooling. The energy gap between the occupied electronic states and their excited counterparts is much smaller in these metals so that thermal excitation remains a possibility even at lower temperatures. Metals were not a part of the primordial gas mix since they are only produced by stars over the course of their lives. The effectivity of gas cooling thus depends on the history of local star formation in addition to the multitude of parameters that alter cooling processes directly. Because both metals and molecules make up only a tiny fraction of the gas in our Universe, small fluctuations in their abundances can greatly affect the overall cooling efficiency in cold gas where they act as the primary coolants.

In cosmological simulations, which aim to simulate the history of the Universe from the dawn of structure formation, it is impossible to resolve these microscopic processes. Doing so would push the requirements for memory and computational power beyond the abilities of any computer available or imaginable. Instead, simulations rely on sub-resolution models that predict the net effect of unresolvable processes on an entire region of the Universe represented by a single resolution element. This is not only true for cooling, a process on the atomic scale, but even for star formation which begins on the scale of the Jeans instability. These models rely on theoretical predictions and observational data to make their calculations. However, they still have to make some simplifying assumptions to keep computational complexity at manageable levels.

The common simplification for the multitude of cooling processes in the typical gas mix is to gather them under the umbrella of a single multivariable cooling function Λ, which describes the net energy loss per unit time and volume of the gas. For a given set of variables such as density, temperature, and metallicity, the cooling function can be calculated from theoretical models for the relevant cooling processes like the collisions described above, but also Compton scattering and bremsstrahlung effects. Performing these calculations at every timestep in a large simulation for every resolution element would be far too expensive computationally, so instead the function is interpolated from a set of pre-calculated values. The number of values contained in such cooling tables is limited by the available computer memory, setting a limit for the precision of the interpolation. The time needed for an interpolation depends on the number of variables fed into the cooling function, with each additional variable adding a step to the interpolation process.

In the cold gas the abundances of the primary coolants can fluctuate strongly with even relatively minor changes in the environment, and an interpolated cooling function may be unable to capture changes due to these shifts in the chemical composition of the gas. The model tested in this thesis was developed by Maio et al. 2007 as an alternative approach to the standard sub-grid cooling in the low temperature regime. It features a chemical network tracking the abundances of important coolants and any relevant gas species they can be created from or transformed into by chemical reactions. With this information at hand at every timestep in the simulation, it is no longer necessary to interpolate a total cooling function for the entire gas mix. Instead, the contributions from individual species are summed up to their net effect on gas cooling. Details on the model and its implementation into cosmological simulation are presented in Chapter 3. The main objective of this thesis is to compare this chemical network implementation of low temperature cooling to the standard approach in a variety of cosmological simulations, which are described in Chapter 2. Of particular interest in this are the model's effects on galaxy formation and evolution, which are discussed in Chapters 4 & 5.

1.3 Observations of Cold Gas

In addition to improving cooling at low temperatures, the chemical network provides another boon to cosmological simulations. By tracking the abundances of individual gas species,

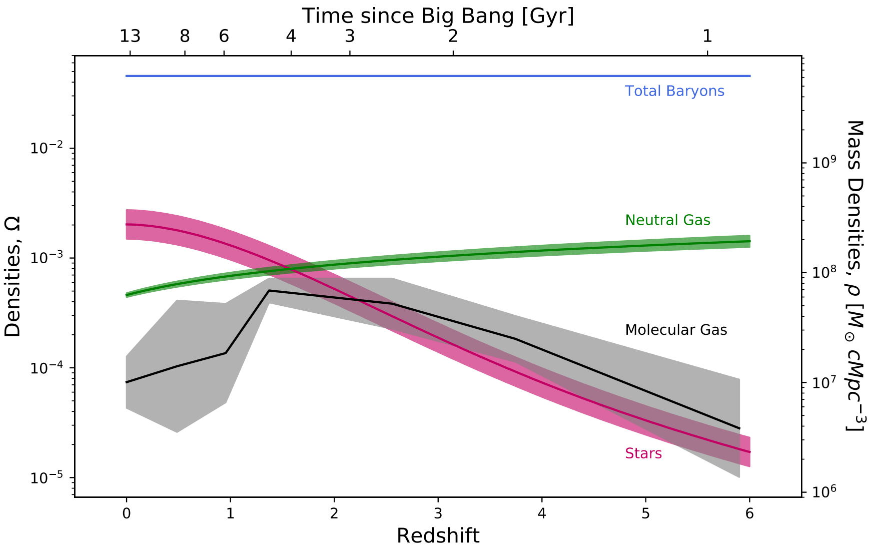

Figure 1.2: Cosmic density evolution of neutral atomic and molecular hydrogen, as well as stars in our Universe from Péroux and Howk 2020 (their Figure 4).

their cosmological density evolution and the mass fractions they account for in galaxies can be directly assessed from the simulation output. These data are otherwise only obtainable through post-processing schemes that require additional model assumptions.

With every new generation of astronomical instruments, observations of the molecular and cold gas content of our Universe as outlined above have become more precise. Current observations constrain the cosmic density of H_2 in the Universe up to redshifts of about z=5-6 (Riechers et al. 2019, Garratt et al. 2021). The constraints on the cosmic density evolution of neutral atomic hydrogen (HI) are even stronger, with data available up to redshifts of about 5 (Rhee et al. 2017). For a comprehensive overview of observations regarding cosmic baryon evolution see Péroux and Howk 2020, whose results on cosmic baryon evolution from a compilation of data are shown in Figure 1.2. They find a steadily declining amount of neutral atomic hydrogen between z=6 and z=0, and a peak in molecular gas density between z=2 and z=1, that coincides with the highest star formation rate densities. The shaded areas, indicating the uncertainties of the respective measurements, help quantify the observational constraints on neutral and molecular hydrogen abundance mentioned above.

With the chemical network, simulations gain additional points of comparison to this wealth of observational data which can be used to further develop the model. Producing cosmological density data comparable to the above mentioned requires the simulation of a cosmological volume, or box, large enough to be representative of the Universe as a whole. The results of testing the chemical network in such simulations are presented in Chapter 4.

As for the cold gas content of galaxies there are extensive surveys of both the HI (Catinella et al. 2010) and H_2 (Saintonge et al. 2011) masses up to redshifts of 0.5 and over a range of $10^9 - 10^{11.5} M_\odot$ in stellar mass. With their large samples and high completeness, these studies can determine scaling relations for H_2 or HI mass fractions, which are both found to decrease with stellar mass for instance. In nearby galaxies recent observations resolve the structure of molecular gas on the scale of 100 pc (Bešlić et al. 2021). This provides an excellent reference for cosmological zoom-in simulations which, with the addition of the chemical network, can track the HI and H_2 mass evolution of a galaxy in much greater detail than a cosmological box. Different implementations of the model were tested in a suite of such zoom simulations, and are compared to the available data in Chapter 5.

At lower redshifts, gas chemistry and as a consequence cooling become potentially much more complicated than in the primordial Universe. Pollution of the primordial hydrogen-helium-mixture with dust opens new formation channels for molecular gas through catalytic reactions on the surface of dust grains. It is possible that in order to accurately model the balance in the chemical network these have to be accounted for. Comparing the abundances of molecular gas in the model to observational data could help determine the significance of this problem and if an addition of dust to the chemical network is necessary. Another potential future expansion of the chemical network is to include CO, which would allow a direct comparison to observations of molecular gas without relying on the CO to H_2 conversion factor.

1.4 Galaxy Formation and Growth

The presence or absence of gas shapes galaxies in more ways than just in situ star formation. Structure formation and growth in our Universe is hierarchical, meaning that from the initial density perturbations small objects grow first and combine over time into larger objects. A galaxy grows more massive by accreting additional matter, which generally happens in one of two ways: Either by mergers with other galaxies, or by the smooth accretion of gas from the surrounding medium. In the first case a distinction is often made between major mergers of two galaxies with similar masses, and minor mergers where a galaxy merges with a significantly smaller galaxy. The lines between the sizes in these definitions, and even between those of the smallest of mergers and the largest of clumps in smooth accretion, can be somewhat blurry. They are generally chosen in such a way, that they reflect the varying impact the different modes of accretion can have on a galaxy's evolution.

A simple estimate using the Virial theorem can be made to determine the merger induced growth in size of a galaxy, consisting only of stars in this example (following Naab et al. 2009). If the galaxy initially has a mass M_i, a gravitational radius $r_{g,i}$, an internal velocity dispersion $\langle v_i^2 \rangle$ and a total energy E_i, with a kinetic part $K_i = M_i \langle v_i^2 \rangle / 2$ and a potential part $W_i = -M_i^2 G / r_{g,i}$, these quantities are linked by the Virial theorem as follows:

$$\begin{aligned} E_i = K_i + W_i = -K_i &= \frac{1}{2} W_i \\ -\frac{1}{2} M_i \langle v_i^2 \rangle &= -\frac{1}{2} \frac{M_i^2 G}{r_{g,i}}. \end{aligned} \tag{1.1}$$

Now let this galaxy accrete some mass of stars M_a with total energy E_a, gravitational radius $r_{g,a}$ and internal velocity dispersion $\langle v_a^2 \rangle$. It is useful to define the ratio of masses between the two systems as $\eta = M_a / M_i$, and the ratio of their velocity dispersions as $\epsilon = \langle v_a^2 \rangle / \langle v_i^2 \rangle$. The total energy of the system after accretion is then given by

$$\begin{aligned} E_f &= E_i + E_a \\ &= -\frac{1}{2} M_i \langle v_i^2 \rangle - \frac{1}{2} M_a \langle v_a^2 \rangle \\ &= -\frac{1}{2} M_i \langle v_i^2 \rangle (1 + \eta \epsilon) \\ &= -\frac{1}{2} M_f \langle v_f^2 \rangle, \end{aligned} \tag{1.2}$$

where $M_f = (1 + \eta) M_i$ is the final mass of the system. From this, it follows for the final velocity dispersion $\langle v_f^2 \rangle$ that

$$\langle v_f^2 \rangle = \frac{1 + \eta \epsilon}{1 + \eta} \langle v_i^2 \rangle. \tag{1.3}$$

From Equation 1.1 it follows that $r_g \propto M / \langle v^2 \rangle$ so that the final radius of the system is given by

$$r_{g,f} = \frac{(1 + \eta)^2}{1 + \eta \epsilon} r_{g,i}. \tag{1.4}$$

With Equation 1.4 it is possible to determine the growth of a galaxy through a series of accretion events. Consider first a galaxy which doubles its mass in a single major merger with another galaxy of equal size. In this case $\eta = 1$ and $\epsilon = 1$ so that the resulting final radius has twice the initial value. If the same galaxy instead doubles its mass ($\eta = 1$) by accreting multiple small systems, such that $\langle v_a^2 \rangle \ll \langle v_i^2 \rangle$ and consequently $\epsilon \ll 1$, then Equation 1.4 yields and increase in size by a factor of 4. This effect of growth through a multitude of minor mergers has been suggested as the driving factor in massive elliptical galaxies reaching the sizes at which they are observed today (Naab et al. 2009, Hilz et al. 2012).

The above derivation assumes single component galaxies consisting only of stars. In real world processes this is most applicable to the accretion of stellar material that has been stripped of its gaseous counterpart by hydrodynamical effects. Such gas poor mergers are called 'dry' and find their counterpart in 'wet' mergers between objects with high gas fractions. Bringing gas into the mix adds a dissipative component, through which some of the energy in a merger can be shed, resulting generally in a less pronounced increase in size (Hilz et al. 2012). It should be noted, that this excursion into galaxy mergers only scratches the surface of the complicated topic. Many more parameters than the ones presented here may influence the outcome of a merger, and finer distinctions into merger sub-categories with distinct effects on galaxy evolution can be made (see for instance Karademir et al. 2019.)

The galaxies we observe today owe their appearance to the complex interplay between mergers and in-situ star formation. When and where stars form within a galaxy, and how compact or extended it is as a result, all affect the outcome of any future mergers it might experience. Capturing this rich history of galaxy formation in simulations requires models for gas dynamics and star formation that can accurately reproduce the wide range of different galaxies observed. The chemical network model tested in this thesis aims to improve our understanding of gas dynamics, cooling, and star formation, and thus represents one step forward in this process.

Chapter 2

Simulations

For this thesis I aim to test an alternative low temperature cooling model in a variety of cosmological simulations. The goal is to understand its effects on the dynamics and evolution of cold gas in the galaxies populating these simulations. This should help determine the models functionality at the typical resolutions obtainable in cosmological studies and its ability to predict cooling behavior and chemical evolution in non-primordial gas at lower redshifts. All simulations discussed in this thesis were performed with the OpenGadget-3 code which is based on GADGET-2 (Springel 2005). It employs a Tree-Particle Mesh (Tree-PM) method for gravitational computations and a Smoothed Particle Hydrodynamics (SPH) method for the treatment of gas physics. To better highlight and put into context the features of the alternative chemical network approach to cooling I provide an overview of the basic aspects of cosmological simulations with Gadget and details on the specific simulations used in my tests.

The formation of stars from the gravitational collapse of gas clouds is a vitally important process even for structure formation on galactic scales where stellar feedback plays an important role. For cosmological simulations it is impossible to resolve this process spatially and thus they have to rely on some measure of 'sub-grid' modeling to approximate the life cycle and feedback of stars. For an SPH code like Gadget this means that every gas particle, each of which represents a region larger than the Jeans scale of gravitational collapse, has to form stars 'internally' when some conditions are met. In the model applied to the simulations used in this work, it then splits some of its mass off into a new star particle which in turn represents a whole population of stars formed in the region. The simplest criterion for such internal star formation is a density threshold for the gas particle but additional criteria such as the convergence of the local gas flow may have to be met. Because the whole population of stars is represented by a single particle, feedback such as supernova explosions or stellar winds have to be calculated as the average effect of such a population. This in turn means that the distribution of stellar masses within the population has to be known since for example the assumed supernova rate will depend on the number of massive stars in the population. For the simulations presented here the initial mass function (IMF) used to distribute stellar masses at the point of star formation is adapted from Chabrier 2003.

In general, the IMF will depend on the gas phase metallicity at the time of star formation. Interstellar gas is enriched with metals by stellar feedback, another process that is approximated in a sub-grid approach (Dolag et al. 2017). The main modes of enrichment are supernovae, winds from massive stars and stars at the end of their lifetimes on the so-called asymptotic giant branch. How effective this enrichment is, or the yield of the particular processes, has to be fed to the sub-grid model. In this thesis yields for supernovae of type Ia were taken from Thielemann et al. 2003, those for massive stars follow Nomoto et al. 2013, and those for asymptotic giant branch stars follow Karakas and Lattanzio 2007.

The gas phase metallicity also plays a role in the cooling of gas, particularly at low

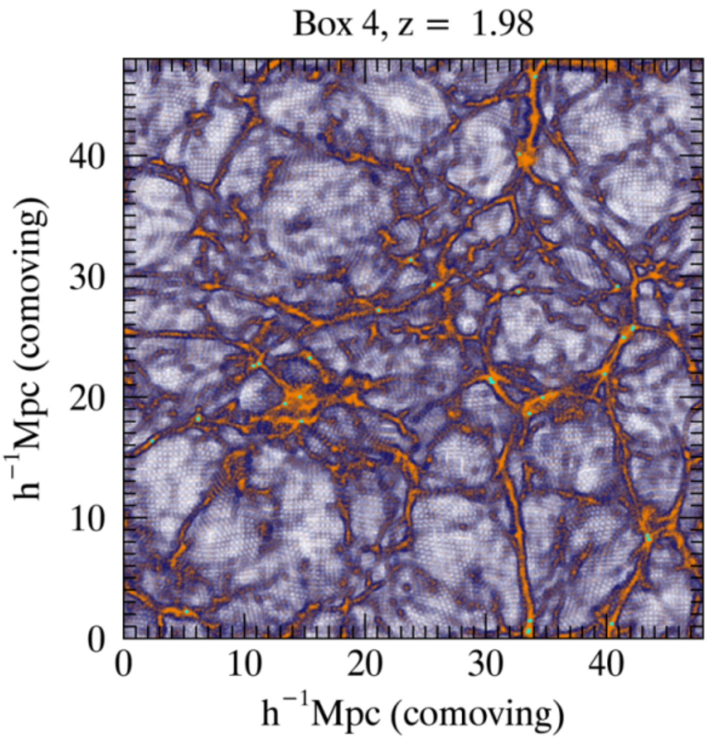

Figure 2.1: A 500 kpc slice through the center of Magneticum Box 4. Dark matter particles are depicted in purple, gas in orange and stars in cyan.

temperatures where it forms stars. In general, gas cooling in simulations is described by a singular cooling function that can depend on a range of parameters like temperature, density, background radiation and gas metallicity. Computing the cooling function for a set of parameters is too computationally intensive to perform for each particle at each timestep so it is instead interpolated from tabulated pre-computed values. This cooling scheme is altered by the additional chemical network model tested in this work, particularly at low temperatures. This is discussed in more detail in Chapter 3.

2.1 Full Cosmological Simulation

A cosmological box is the closest a simulation can get to reproducing our entire Universe. As the name suggests it consists of a cubic volume that is initialized with a density distribution inferred from observations of our own cosmos or more specifically the cosmic microwave background. In the simplest approach the box is populated with dark matter only which is computationally much easier to treat since it only interacts gravitationally. Studying the formation and dynamics of galaxies, however, is only possible by adding the primordial gas component to the initial conditions. This distribution of dark matter and gas is then evolved according to the chosen implementation of the laws of gravity and hydrodynamics. Periodic boundary conditions are used for the interactions so that the finite box volume can reproduce even long range gravitational interactions and to avoid unphysical modes of collapse at the box limits.

The size of the cosmological box limits the mass of structures that can form within it. Smaller boxes do not cover the scales of density perturbations from which the most massive structures form and can thus not reproduce them. On the other end of the mass scale resolution is the limiting factor. Since both higher resolution and larger box sizes require more computational resources, cosmological simulations have to strike a balance between the two.

Box 4 of the Magneticum simulation covers a (48 Mpc)^3 volume with ca. 10^7 dark matter particles in the high resolution (HR) run. This makes it one of the smallest cosmological boxes in the Magneticum Pathfinder project, but ideally suited to higher resolutions which are necessary to study galaxy properties. The resulting resolution in the dark matter component is approximately 91 particles per Mpc^3 each with a mass of $m_{\mathrm{dm}} = 6.90 \cdot 10^8\ M_\odot$. As with all Magneticum simulations, Box 4's initial conditions include gas accounting for 16.8 % of the total matter density $\Omega_0 = 0.272$. The number of gas particles is also of the order of 10^7. All simulations of Box 4 discussed here assume a ΛCDM cosmology with $\Omega_\Lambda = 0.728$ and $h = 0.704$ and are initialized at $z = 60$.

A cosmological box provides a representative sample region of the universe both for the analysis of global quantities like cosmological densities and the statistical distribution of galaxy properties. Galaxies in Box 4 were identified using the SubFind algorithm (Springel et al. 2001, Dolag et al. 2009) which identifies structures in SPH simulations using a friends-of-friends (FoF) method. Each FoF-group identified by SubFind is further split into sub halos by analyzing overdensities within the group, each of which is expected to host a galaxy or dwarf galaxy equivalent. Of these sub halos, the most massive is identified as the main halo of the FoF-group. Depending on group mass this arrangement can correspond to a galaxy cluster with a central BCG or a small isolated galaxy with satellites.

2.2 Zoom Simulations

Cosmological simulations always have to compromise between higher resolution and larger box sizes. The former allows to simulate physical processes to smaller scales and resolve more details in the resulting structures while the latter ensures a more accurate distribution of galaxy masses and environments. Zoom simulations attempt to improve the terms of this compromise by re-simulating a region of a cosmological box containing an object of interest with higher resolution embedded in the lower resolution box. Thus in principle one can resolve details in the structure without removing it from its cosmological environment and consequently altering its formation history.

The accuracy to which long range gravitational interactions such as tidal forces can be reproduced depends on the angular resolution. This means that the spatial and mass resolution can be decreased with distance from the target object without losing accuracy as long as the angular resolution stays constant. Far away from the target region the resolution can even be lower than in the parent simulation which can be achieved by binning particles on a spherical grid.

2.2.1 Zoomed Initial Conditions

The basis for such simulations are zoomed initial conditions (ICs) which have to be created from the original initial conditions of the parent cosmological box. The ICs used for this work were created using the ZIC code developed by Tormen et al. 1997. This is an iterative process in which a Lagrangian volume around the target object is identified and its contents replaced by high resolution particles in the ICs. A first naive guess at the shape of the necessary initial volume will usually lead to a contamination of the final region with low resolution particles after evolving the modified ICs. This contamination is problematic because the low resolution particles have a much higher mass than particles in the high resolution region and thus act as massive compact perturbers with no physical counterpart. The choice for an initial high resolution region thus needs to be adapted until the region of interest is no longer contaminated.

Scaling up the resolution in the target region alone does not produce suitable ICs. In addition, the initial density perturbations from which structure grows in the cosmological simulation need to be extended to the high resolution region. This requires perturbations on scales too small to be reproduced in the resolution of the parent simulation to be added to the perturbation power spectrum. If the power spectrum calculated for the parent simulation does not extend to such small scales an extension needs to be computed. This limits the increase in resolution that can be gained for the target region relative to the parent simulation. Local tidal forces on the high resolution region are reproduced by a shell of particles sampled at the low resolution of the parent simulation. The resulting difference in mass between the neighboring high and low resolution regions creates an additional limit on the resolution that can be gained by zooming, albeit a softer one. If this difference becomes too large, it will be likely that unphysical interactions in the boundary layer influence the target region. Outside this shell the resolution can be gradually reduced by binning particles on a spherical grid, such that a constant angular resolution is maintained. This ensures that long range forces are reproduced consistently while keeping the number of particles, and thus the computational complexity, to a minimum.

The parent simulation for the zooms performed for this work is the dark matter only Dianoga simulation. Thus, in order to study gas physics and its effect on the formation of stars and galaxies, the zoom region needs to be populated with baryons in addition to the present dark matter. To preserve the total mass of the high resolution region and its distribution a gas particle has to be split off of each dark matter particle and displaced by the mean inter particle distance within the high resolution region while conserving its momentum. This ensures the resulting density distribution matches the one prescribed by the cosmological initial conditions. In the boundary region between the zoom volume and the low resolution box dark matter particles are not split and thus remain more massive which helps decrease the mass difference to the neighboring low resolution shell.

2.2.2 Choice of Objects

As discussed above, a zoom-in region contains a target object and its neighborhood. The specific size of this neighborhood is determined by how isolated the galaxy is. To ensure all relevant close range interactions are modeled at sufficient resolution, neighboring galaxies with masses similar to the target mass need to be included in the high resolution region. It is thus computationally cheaper to re-simulate field and void galaxies which are less likely to have many close neighbors of this kind.

The galaxies chosen as targets for zoom simulations in this thesis are a $\sim 9 \cdot 10^{11}\ M_\odot$ object dubbed Asin (Bittner 2018) and a $\sim 1 \cdot 10^{13}\ M_\odot$ object dubbed Dfrogin (Schlachtenberger 2014). Both have been re-simulated in zoom-ins for previous work and thus sets of ZIC were available for a range of resolutions. From these previous simulations we know that the target object in Asin is a late type galaxy at low redshifts and has a companion of almost equal mass ($\sim 8 \cdot 10^{11}\ M_\odot$). The more massive Dfrogin is expected to lose its disk after $z \sim 2$ and evolve into an early type galaxy at low redshifts.

2.2.3 Merger Trees

Tracing the target object back to its formation redshift requires building a merger tree for the simulation. This involves identifying the particles that are bound to a halo and finding the structure which contains most of those particles in subsequent outputs. The tree building algorithm used here identifies these descendants not only for the next snapshot but for the one after as well. This helps to trace halos that are temporarily 'dissolved' during close encounters, meaning the particles previously identified by SubFind as part of the halo are erroneously attributed to a different halo. From these descendant files a complete merger tree for all halos in the zoom simulation is then constructed.

For a target object in a given snapshot the main progenitor is considered to be the halo

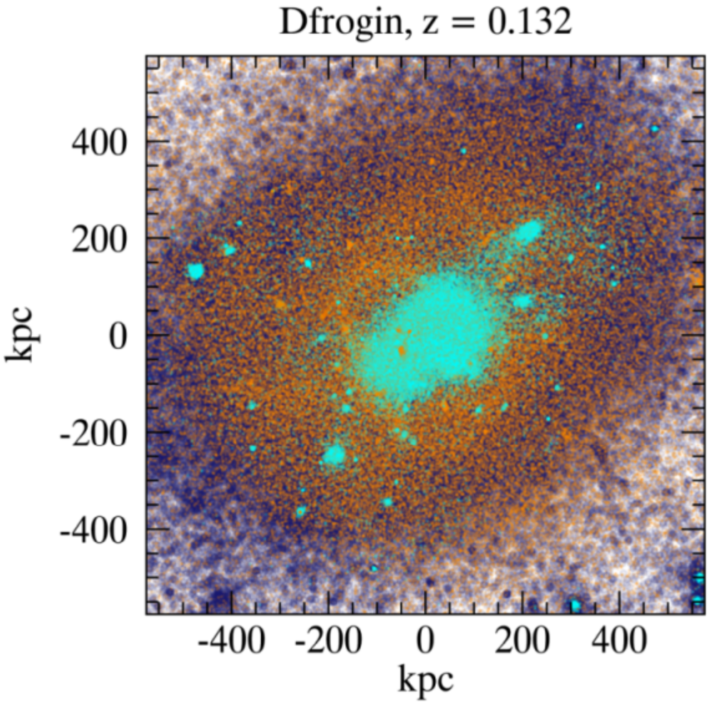

Figure 2.2: Visualization of the Zoom-in target object Dfrogin at low redshift. Shown is a volume of $(R_{\mathrm{vir}})^3$ centered on the galaxy. Dark matter particles are depicted in purple, gas in orange and stars in cyan.

in the previous snapshot that contains the majority of the target's member particles. The algorithm gives a higher weight to the most bound particles of a halo in this process, which allows it to track a halo's position through a merger where some of its particles may be attributed to the merging halo by SubFind. For the analysis done in this thesis exact halo positions are not of interest, but the mass evolution of the halo is. Thus when 'walking the tree' for the target object of a zoom simulation, i.e. the most massive galaxy in the region at $z = 0$, to its formation redshift I switch to the main halo in the FoF-group of the progenitor in every snapshot. In most cases this procedure should return the majority of particles that make up the target in each snapshot, even when it is going through a merger.

Chapter 3

The Chemical Network

At temperatures below 10^4 K, atomic hydrogen is no longer an effective coolant and gas cooling is dominated by molecules and heavier elements. These gas species are much less common in the Universe than the ubiquitous atomic hydrogen, and their relative abundances vary with local conditions. Thus below this temperature threshold the particular chemical balance in the gas at any moment in time has a much greater impact on cooling. The model used in this thesis employs a chemical network to track the relative abundances of the most important gas species as they develop over time. These abundances can then be used to calculate each individual species' contribution to the cooling function directly at each timestep instead of relying on interpolations of tabulated values.

3.1 Hydrogen and Helium Chemistry

A chemical network consists of individual species and the reactions that create and destroy them. Species include both the atoms present in the gas and the molecules they can combine to as well as any relevant ionized state. If one considers only primordial chemistry, as was the case when this model was first developed by Maio et al. 2007, the only elements playing a significant role are hydrogen, deuterium and helium. In addition to these three atomic species, the five ion species H^+, H^-, D^+, He^+ and He^{2+} and the four molecules H_2, H_2^+, HeH^+ and HD are included in the network. For each of these 12 species the model assigns a number density n at each timestep.

Every possible chemical reaction between these species can be assigned a reaction rate k that will depend on temperature. The set of species and reaction rate coefficients together form the chemical network. In practice some reactions or species are insignificant for the evolution of the network as a whole in the regime covered by the simulation and can be neglected in a reasonable approximation to save computational resources.

The rate of change of the number density of a single species can be expressed in terms of the number densities and reaction rate coefficients of all species as follows:

$$\frac{\mathrm{d}n_i}{\mathrm{d}t} = \sum_p \sum_q k_{pq,i} n_p n_q - \sum_j k_{ji} n_j n_i. \tag{3.1}$$

The first term describes the creation of the species i from reactions of other species q and p and thus the summation effectively runs over all possible combinations that result in such a reaction. The second term describes the destruction of the species via reactions with other species j. It is helpful to define the creation and destruction coefficients C_i and D_i from these terms.

$$\begin{aligned} C_i &= \sum_p \sum_q k_{pq,i} n_p n_q, \\ D_i &= \sum_j k_{ji} n_j. \end{aligned} \tag{3.2}$$

With equations 3.1 and 3.2 the change of the number density of a single species over a single timestep can be expressed in discretized form as

$$\frac{n_i^{t+\Delta t} - n_i^t}{\Delta t} = C_i^{t+\Delta t} - D_i^{t+\Delta t} n_i^{t+\Delta t}, \tag{3.3}$$

so that the number density of the species at the later time $t + \Delta t$ is given by

$$n_i^{t+\Delta t} = \frac{C_i^{t+\Delta t} \Delta t + n_i^t}{1 + D_i^{t+\Delta t} \Delta t}. \tag{3.4}$$

The resulting system of equations needs to be solved at each time t to compute the evolution of the network over the next timestep Δt. For an exact computation, the creation and destruction coefficients at the time $t + \Delta t$ are needed. To circumvent this problem one can first approximate the result using the coefficients computed at time t for some species and use the result to get a better approximation for the remaining species. Since some species are more prone to rapid changes in their abundances or more reactive to changes in abundance of a different species, the sequence in which to update the different species can affect the quality of the resulting approximation. This process can be iterated to mimic a backwards differentiation scheme (Anninos et al. 1997). In practice the timesteps are small enough that the coefficients at time $t + \Delta t$ can be substituted with those computed for the current time to a very good approximation cutting down on computation time.

Each gas species contributes to cooling through various processes the relative importance of which depends on gas density and temperature. For hydrogen and helium the contributions from collisional ionization, excitation, and recombination are implemented based on rates from Hui and Gnedin 1997, while Compton scattering and bremsstrahlung effects are based on the work of Black 1981. Cooling due to molecular hydrogen in its neutral and singly ionized states is calculated based on the rates from Galli and Palla 1998. Lastly, the contribution from the HD molecule follows the function given in Lipovka et al. 2005.

While tracking all species in the chemical network is necessary to accurately predict their relative abundances, some play an insignificant role in cooling compared to the dominant coolants. Which species dominate the cooling and heating processes depends on gas temperature and density as well as the relative abundances of the species in question, and the abundance of collision partners such as electrons. For an example configuration with a hydrogen number density of 1 cm^{-3} and fractional species abundances of $f_{\mathrm{H}_2} = 10^{-5}$, $f_{\mathrm{H}_2^+} = 10^{-13}$, $f_{\mathrm{HD}} = 10^{-8}$ and $f_{\mathrm{e}} = 10^{-4}$ for the relevant coolants Maio et al. 2007 show the temperature dependence of the individual species contributions in their Figure 2 which is reproduced here in Figure 3.1.

3.2 Metal Treatment

With metal enrichment through stellar feedback, primarily supernovae, heavier elements play an increasingly important role in cooling. While metal enrichment is part of the base line stellar evolution and feedback model as described in Chapter 2, metal cooling is only implemented through a metallicity parameter in the cooling function. In the chemical network

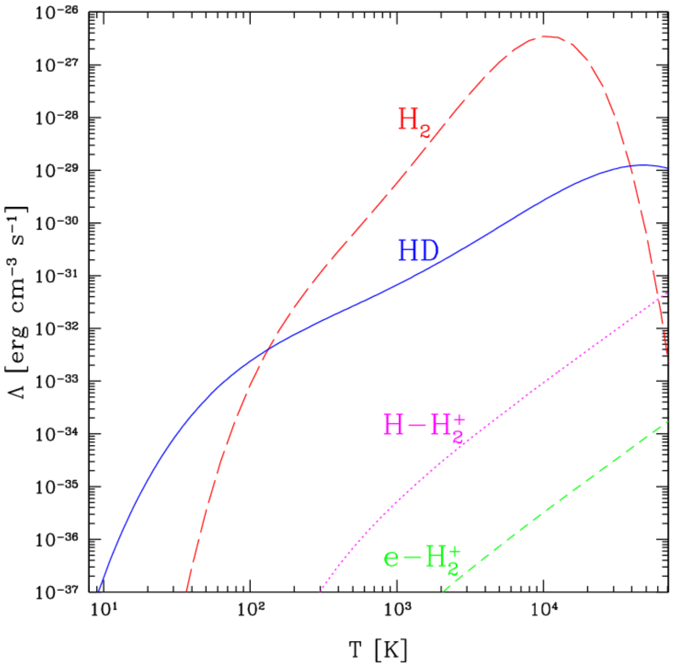

Figure 3.1: Cooling contributions of HD, H_2, and H_2^+ as implemented in the chemical model shown for a range of temperatures at a fixed hydrogen number density of 1 cm^{-3}. Taken with kind permission from Maio et al. 2007 (their Figure 2). Note that the H_2^+ contribution is split into the contributions from collisions with neutral atomic hydrogen and electrons respectively with both fits only valid for $T < 10^4$ K.

metal species are treated as multilevel systems and their contribution to gas cooling is calculated from transitions between levels. The model used here includes oxygen, carbon, silicon and iron which are the most common metals released by stars. Oxygen and carbon are mainly produced in supernovae of type II, while silicon and iron stem mostly from type Ia supernovae.

It is assumed that carbon, silicon, and iron are completely ionized because their ionization energies lie below that of hydrogen (13.6 eV) and therefore within the spectrum of the UV background. Oxygen on the other hand has an ionization potential of 13.62 keV and is thus assumed to be mostly neutral as hydrogen is so abundant in the Universe that any photons with energies above 13.6 eV will be absorbed in the process of ionizing hydrogen atoms long before interacting with any of the much less abundant metals.

At the very low densities generally considered in cosmological simulations, thermodynamical equilibrium cannot be assumed for the population of the multiple excitation levels present for each metal. Instead the steady state has to be calculated from the constraints of balance in each state and conservation of the total particle number for each species. Balance in an excitation state is achieved if the number of transitions into the state is equal to that of transition out of the state, which can be expressed as

$$n_i \sum_{j \neq i} P_{ij} = \sum_{j \neq i} n_j P_{ji}, \tag{3.5}$$

where the left hand side refers to the depopulation of the ith level with number density n_i and P_{ij} being the transition probability from state i to state j. The right hand side refers to the population of the ith level from the jth with the probability P_{ji} for such a transition. The transition probabilities can be calculated from the collision rates for induced transition and the Einstein coefficients for spontaneous transition. As for the requirement of particle number conservation, it is simply stated as

$$\sum_i n_i = n_{\text{tot}}. \tag{3.6}$$

The rate of transition between levels i and j induced by collisions with some partner with number density n_x is defined as

$$n_i n_x \gamma_{ij} \equiv n_i n_x \langle u\sigma_{ij} \rangle = n_i n_x \int u\sigma_{ij} f(u) d^3u, \tag{3.7}$$

where σ_{ij} is the collision cross section, $f(u)d^3u$ the particle velocity distribution function and the integration runs over the entire velocity space. For the inverse process the corresponding factor γ_{ji} is related to this by

$$g_i \gamma_{ij} = g_j \gamma_{ji} e^{-\beta \Delta E_{ji}}, \tag{3.8}$$

with the level multiplicities g and the energy difference between levels ΔE_{ji} for $j > i$ and $\beta = (kT)^{-1}$. In addition, each possible spontaneous transition from the ith level to a lower level j yields an additional term $n_i A_{ij}$ to the sum in (3.5) with the Einstein coefficient for spontaneous emission A_{ij}.

An n-level system is thus constrained by $n - 1$ independent equations following from Equation 3.5 and one additional independent equation from particle number conservation. For the metal treatment in this model, ionized carbon (CII) and silicon (SiII) are approximated as two-level systems, while neutral oxygen (OI) and ionized iron (FeII) are approximated as five-level systems following Santoro and Shull 2006.

For the example of a two-level system where collisional excitation is due to interactions with hydrogen atoms and electrons, the corresponding system of equations would be

$$\begin{aligned} &n_1 + n_2 = n_{\text{tot}}, \\ &n_1 n_{\text{H}} \gamma_{12}^{\text{H}} + n_1 n_{\text{e}} \gamma_{12}^{\text{e}} - n_2 n_{\text{H}} \gamma_{21}^{\text{H}} - n_1 n_{\text{e}} \gamma_{21}^{\text{e}} - n_2 A_{21} = 0, \end{aligned} \tag{3.9}$$

where the sub or superscript e denotes quantities relating to interactions with electrons and H denotes those involving hydrogen atoms. Solving for the level populations n_1 and n_2 relative to the total number of particles yields

$$\frac{n_1}{n_{\text{tot}}} = \frac{\gamma_{21}^{\text{H}} + \gamma_{21}^{\text{e}} n_{\text{e}}/n_{\text{H}} + A_{21}/n_{\text{H}}}{\gamma_{12}^{\text{H}} + \gamma_{21}^{\text{H}} + (\gamma_{12}^{\text{e}} + \gamma_{21}^{\text{e}}) n_{\text{e}}/n_{\text{H}} + A_{21}/n_{\text{H}}}, \tag{3.10}$$

$$\frac{n_2}{n_{\text{tot}}} = \frac{\gamma_{12}^{\text{H}} + \gamma_{12}^{\text{e}} n_{\text{e}}/n_{\text{H}}}{\gamma_{12}^{\text{H}} + \gamma_{21}^{\text{H}} + (\gamma_{12}^{\text{e}} + \gamma_{21}^{\text{e}}) n_{\text{e}}/n_{\text{H}} + A_{21}/n_{\text{H}}}. \tag{3.11}$$

Metal contributions to cooling come from spontaneous transitions out of excited states. For the example of the two-level system the contribution to cooling would be

$$\Lambda = n_2 A_{21} \Delta E_{21}. \tag{3.12}$$

Plugging Equation 3.11 into this yields

$$\Lambda = \frac{\gamma_{12}^{\text{H}} + \gamma_{12}^{\text{e}} n_{\text{e}}/n_{\text{H}}}{\gamma_{12}^{\text{H}} + \gamma_{21}^{\text{H}} + (\gamma_{12}^{\text{e}} + \gamma_{21}^{\text{e}}) n_{\text{e}}/n_{\text{H}} + A_{21}/n_{\text{H}}} n_{\text{tot}} A_{21} \Delta E_{21}. \tag{3.13}$$

For systems with more than two levels the contribution to the cooling function is simply the sum of the individual level contributions

$$\Lambda = \sum_{i \geq 1} \sum_{0 \leq j < i} n_{\text{i}} A_{ij} \Delta E_{ij}, \tag{3.14}$$

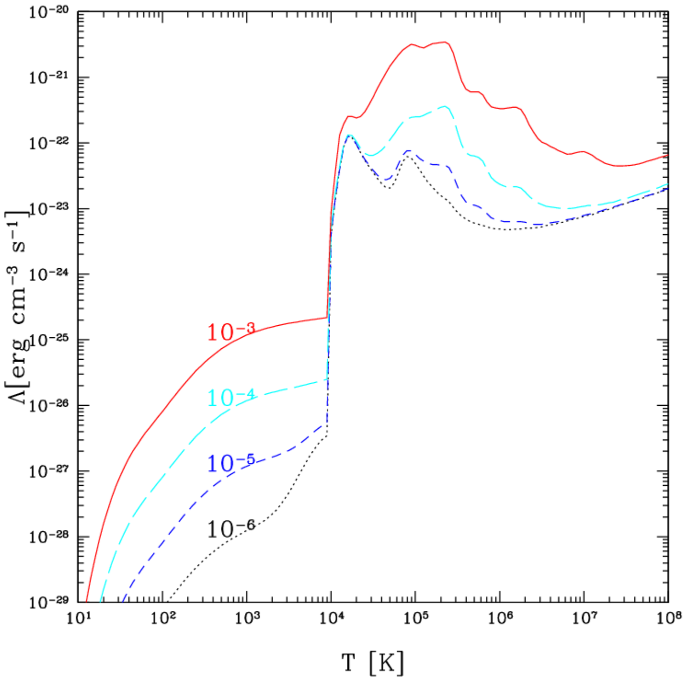

Figure 3.2: Total cooling from the chemical network as a function of temperature for a hydrogen density of 1 cm^{-3}, a H_2 fraction of 10^{-5}, and a HD fraction of 10^{-8}. The different curves represent metal abundances of 10^{-3}, 10^{-4}, 10^{-5}, and 10^{-6} respectively as labeled in the plot. This figure was taken from Maio et al. 2007 (their Figure 4).

which can be computed in much the same manner as shown in Equation 3.13. The contributions from these line transitions combined with those from the chemical network then replace the interpolated cooling functions at temperatures below 10^4 K to better account for the significant fluctuations in abundance of the low temperature coolants. Figure 3.2 shows the net effect of cooling from molecules and metals as a function of temperature for a set of chemical network model parameters and different metal abundances.

3.3 UV Background Radiation

In addition to the local density and temperature, the chemical network has to take into account the background radiation permeating our Universe. This radiation, also called the UV background for its most relevant wavelength, is produced by massive bright stars and the accretion of gas onto black holes in so-called active galactic nuclei. In the simulation this background is implemented as a uniform radiation field with a spectrum based on modelling done by Haardt and Madau 2012, who use a radiative transfer code to match the background inferred from observations. Such an implementation of the UV background is present even in simulations without a chemical network, such as the base line runs performed for this work, where it affects gas temperature and ionization state.

When coupled to the chemical network, in addition to heating the gas, the UV background can directly destroy some species by ionizing them or breaking apart molecules. In practice the coupling of a UV background to the chemical network adds destruction terms to the coefficient in Equation 3.2 to model these processes. In addition heating terms have to be added when calculating the cooling and heating effects of the individual gas and metal species.

Two other models for the UV background by Puchwein et al. 2019 and Faucher-Giguère 2020 are tested in this thesis. Compared to the Haardt and Madau 2012 background, both include new observational data as further constraints for their models. Figure 3.3 shows

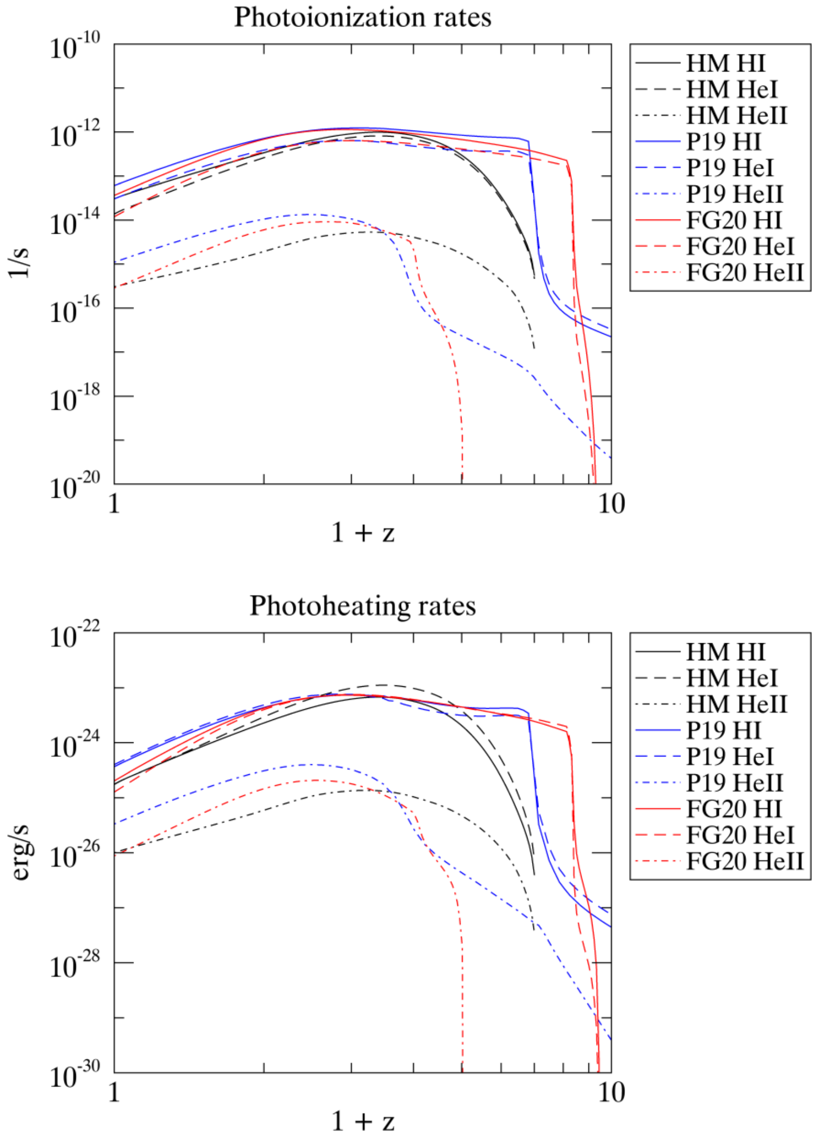

Figure 3.3: Comparison of photoionization (top) and -heating (bottom) rates for HI, HeI and HeII in the three different UV background models. Haardt and Madau 2012 in black, Puchwein et al. 2019 in blue, and Faucher-Giguère 2020 in red.

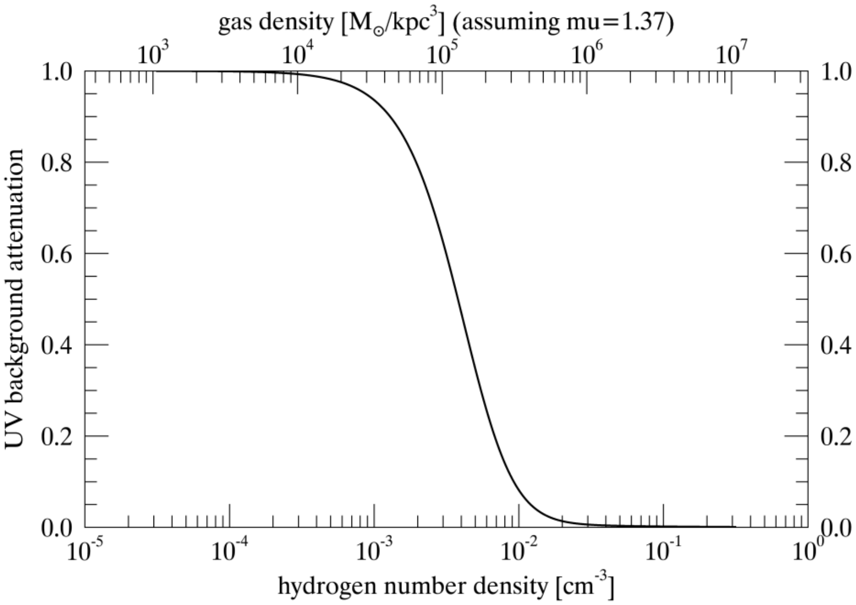

Figure 3.4: Visualization of the HI self-shielding implementation into the chemical network model. The intensity of the UV background is attenuated by a density dependant factor. Total hydrogen number densities as used in the model computations are shown on the lower x-axis while approximate corresponding physical densities are shown above.

the rates of photoionization and photoheating for neutral atomic hydrogen (solid lines) and helium (dashed lines), as well as singly ionized helium (dash-dotted lines) in the different UV background models. The most notable difference in the newer models is the earlier and steeper onset in the rates for HI and HeI when compared to the default model, which has a more gradual increase for both.

3.4 Shielding

Shielding is a crucial process for molecule formation in a Universe permeated by ionizing background radiation. It occurs when the column density in a gas region becomes large enough for the gas to be optically thick with respect to the UV background. Effectively the radiation is absorbed by the electrons in the outer layer of atoms in the process of ionization until there is so little left that any atoms further in will not experience any background radiation in that particular band. For one gas species to shield another, their spectra have to overlap so that the relevant wavelengths are absorbed. This means that in principle any gas can act as a shield for particles of its own species, this is called self-shielding.

The simulation does not resolve the individual sources of the UV background and instead approximates it as homogeneous and isotropic. It also does not resolve individual gas clouds for which realistic column densities could be computed. Particles in SPH should be seen as tracers for the local density, temperature etc. fields rather than actual clumps of matter. This means calculating a column density for a single particle would ignore the fact that there might well be sources of UV background radiation ‘within’ the ‘particle’. Thus, to estimate the effect of shielding, simulations have to model its net effect on the entire region represented by an SPH gas particle.

This chemical network model approximates the shielding effects of HI and H_2 by attenuating the UV background by a density dependent factor (Maio 2021, in prep.). The basic assumption here is that above a certain density the local gas is expected to form clouds with sufficient column densities to shield part of the gas and negate the effect of the UV background on the chemistry. Figure 3.4 shows the attenuation curve used in this model. Internally the model calculates the attenuation based on hydrogen number density (HI and H_2) but approximate mass densities are given for context and comparison to later plots. The H_2 contribution to shielding in the model is implemented according to Draine and Bertoldi 1996 while the HI contribution is based on the work of Rahmati et al. 2013.

Chapter 4

Cold Gas Properties in a Cosmological Context

Magneticum Box 4 was chosen for this project because it is large enough to allow for an analysis of cosmological and global galaxy properties but small enough to support the necessary resolution and additional cooling module without the computation time becoming prohibitively large. A suite of four simulations was set up to test the chemical network model. The first has no chemical network but only the 'standard' cooling and stellar evolution models used in previous simulations with OpenGadget-3, and serves as a baseline for comparison with the test runs. It is referred to as 'LT' for Luca Tornatore, the developer of the stellar evolution and feedback module used in this run. Of the remaining three, one has the primordial chemical network coupled to the UV background only, while the other two contain an additional model for HI and H_2 self-shielding. They are labeled 'UM', 'UM_shield' and 'UM_shield2' for Umberto Maio, the developer of the aforementioned chemical network module. The latter two different density thresholds for the onset of star formation. For the second shielding run the threshold was increased by a factor of 10 compared to the default used in the other simulations, in order to allow the gas to reach densities at which HI shielding becomes effective. Further details on key simulation parameters across the different runs are listed in Table 4.1. It should be noted that the chemical network runs did not reach a final redshift of 0 due to technical issues unrelated to the chemical network model itself. Thus, the data gathered from these simulations should not be affected by this.

Simulation Name	**LT**	**UM**	**UM_shield**	**UM_shield2**
Resolution	HR	HR	HR	HR
Chemical Network	No	Yes	Yes	Yes
Shielding	No	No	Yes	Yes
SF Threshold	0.5	0.5	0.5	5.0
Final Redshift	0	1.2	1.7	2.0

Table 4.1: Simulation parameter comparison for all Box 4 runs.

With the introduction of the chemical network it is possible to track the evolution of the cosmological densities of different hydrogen species, most notably HI and H_2, which previously could only be acquired through post processing schemes. In order to test the performance of the different cooling models, I first compare the evolution of cosmological densities between the different simulations. The amount of neutral atomic and molecular hydrogen formed over the course of the simulation can be compared to the ever increasing wealth of observational data for our own Universe to gauge how accurately the different models reproduce its formation history. Stellar densities similarly depend on the implementation of cooling and serve as an additional point of comparison to the base model, which does not track the individual

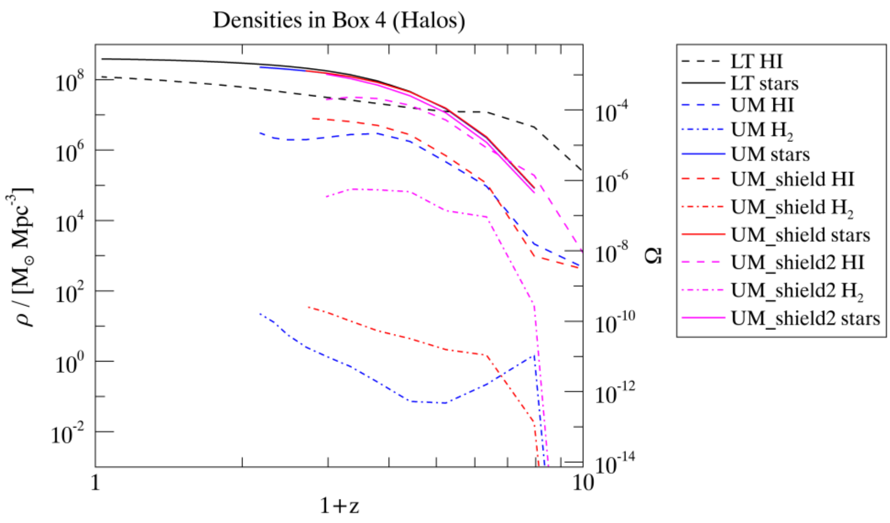

Figure 4.1: Redshift evolution of comoving cosmic densities for the four different runs of Box 4. LT is the reference run without the chemical network, UM denotes the base chemical network model with coupling to the UVB, UM_shield includes HI and H_2 self-shielding on top of the base model, and UM_shield2 includes a higher density threshold for star formation.

gas species. The second, more indirect, mode of comparison is comprised of distributions of various galaxy properties such as their mass-size or mass-angular momentum relations which shed light on how the formation and evolution of structure changes in the new model.

4.1 Cosmological Densities

Figure 4.1 shows the redshift evolution of cosmic densities of molecular and atomic hydrogen as well as stars for the four different simulations. Only particles bound in halos were considered for the mass calculations, but the masses were nonetheless divided by the entire box volume. This should constitute a reasonable approximation since most mass is concentrated in the halos, and indeed the differences are negligible after the formation of the first galaxies in the simulations. In addition, it should be more comparable to observations, since the low surface brightness medium between halos is well below detection limits especially at high redshifts. The choice of only bound particles explains the rapid increase in all densities between redshift 9 and 6; it is a consequence of the first halos assembling. This redshift, at which the first halos are detected by the SubFind algorithm, can be expected to increase with resolution.

For the baseline model without chemical network, no molecular hydrogen densities could be computed since the simulation does not track them. Neutral atomic hydrogen densities are instead calculated in a built-in post-processing scheme from gas density, temperature, and the spectrum of ionizing background radiation, in what is essentially a very simplified chemical network including only neutral and ionized hydrogen as described by Katz et al. 1996. For all three simulations with chemical network, the densities for individual gas species can be computed directly from the output of the network, taking into account the mean molecular mass for the local gas mix. One clear difference between the atomic hydrogen densities found for these different approaches of the baseline and chemical network models can be seen immediately from the dashed lines in Figure 4.1. While the density of atomic hydrogen increases gradually with time in the baseline model, there are signs of a downturn, or at least flattening, of the corresponding curve in all runs with the chemical network around

$z \approx 3$. It should be noted, however, that in the non-shielding run there follows an increase in the HI density after redshift 2, and that this simulation is the only one with chemical network to run to these redshifts. Comparing the three implementations of the chemical network it can be seen that the addition of shielding has only a small effect on the overall HI abundance initially, but significantly softens the peak observed at $z \approx 3$ in the non shielding run. Increasing the density threshold for star formation has a much more pronounced effect on the HI density, adding about an order of magnitude across all redshifts compared to the shielding model with the default threshold.

By far the most striking difference between the three different implementations of the chemical network is in the evolution of molecular hydrogen plotted as dash-dotted lines in Figure 4.1. With the addition of HI and H_2 self-shielding there is about an order of magnitude more H_2 present at lower redshifts than without (red dash-dotted line compared to blue dash-dotted line). Increasing the density threshold for star formation not only adds another ~ 3 orders of magnitude but also flattens out the increase with decreasing redshift and even shows a hint of reversing that trend altogether at lower redshifts (see the pink dash-dotted line). Meanwhile the overall density of stars is barely affected, and its redshift evolution remains completely unchanged between the different configurations of the chemical network.

The increase in neutral and molecular hydrogen abundance with the addition of shielding is explained directly by the attenuation of the UV background which would otherwise be able to ionize HI and dissociate H_2, effectively adding a term to their respective destruction coefficients. Lifting the threshold for star formation allows gas to reach higher densities before converting mass into stars, which in turn disperse gas via the implemented feedback. This has an immediate effect on the abundance of both HI and H_2, since their formation is much more effective at higher densities. The density threshold for H_2 formation is higher than that for HI formation, and consequently the highest density regions in the Universe account for a larger fraction of the former than the latter. These high density regions are exactly what the increase in star formation threshold density aims to add to the simulation, which is why its effect is more pronounced on the H_2 density. It is important to keep in mind that the chosen density threshold for star formation does not directly correspond to a physical threshold, since the actual fragmentation and collapse of gas clouds into stars cannot be resolved in cosmological simulations. Instead the choice is determined by the limits of the implemented gas cooling beyond which any further cooling necessary to form stars has to be assumed.

While with the addition of the chemical network, low temperature and high density cooling should in principle be modelled accurately so that increasing the threshold for star formation is unproblematic, it is still possible to result in over cooling and consequently over clumping of matter. Figure 4.1 clearly shows that the overall abundance of stars (solid lines) at lower redshifts is only mildly affected by the threshold increase, which suggests the threshold increase does not affect the overall star formation rate significantly. Merely the onset of star formation is somewhat delayed. As for possible over cooling effects, the matter distribution within galaxies has to be analysed, which is done in Section 4.2.

In Figure 4.2 the redshift evolution of cosmic densities is compared to observational data. The aforementioned change in the evolution of the HI density with the inclusion of shielding and star formation threshold density increase brings the second shielding run closest to the high redshift observations obtained from Rhee et al. 2017. However, it barely exceeds the base line run even at its peak and both fall short of the observations by almost an order of magnitude. The latter manages to match HI observations at low redshifts, but in doing so produces a reversed trend in evolution with a continuous increase in HI density with time where observations actually show a slight decrease. While all chemical network models show the initial HI density increase slow down or reverse at a redshift of about 3, there is no data for the low redshift range which could be compared to the base model.

The cosmic star formation in the baseline cooling model and all chemical network models

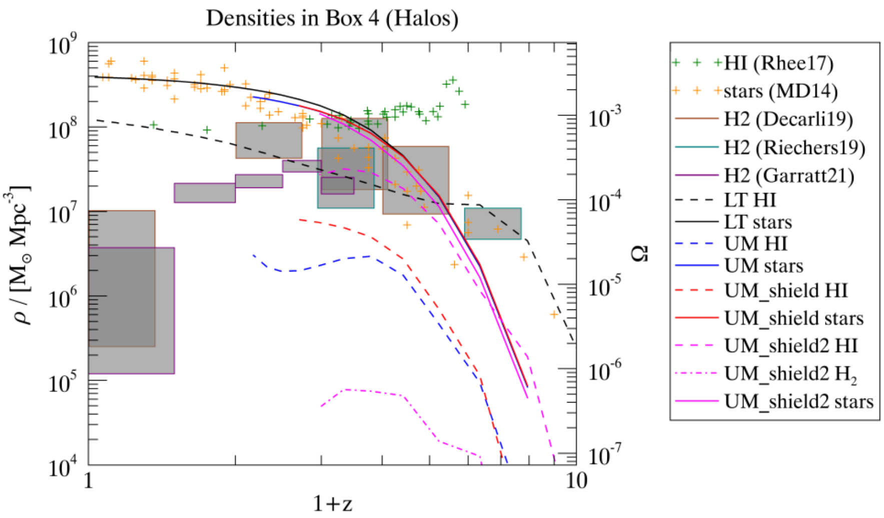

Figure 4.2: Redshift evolution of comoving cosmic densities in the different simulations compared with data. Stellar mass densities are from a range of observations compiled by Madau and Dickinson 2014. HI densities are selected from Rhee et al. 2017 and references therein. The boxes represent 2σ confidence intervals from for the given redshift ranges from ASPECS (Decarli et al. 2019) and COLDz (Riechers et al. 2019). Note the different density range compared to Figure 4.1.

agree with observational data adapted from Madau and Dickinson 2014 (yellow plus signs in Figure 4.2). Any differences in star formation between the models due to their different cooling implementations can thus be considered insignificant, at least on cosmological scales.

As for H_2, it is obvious that even the second shielding run, which produced the highest molecular hydrogen densities, falls short of what is observed in our Universe. The difference to observational data from spectroscopic surveys with ALMA (Decarli et al. 2019) and VLA (Riechers et al. 2019) at radio frequencies, and WFCAM in the sub-millimeter regime (Garratt et al. 2021), is about a factor of 10^3. A possible explanation for this could be the relatively low resolution of the simulation. Molecular hydrogen predominantly forms in dense regions, the largest of which have sizes on the order of a few hundred pc, whereas the gravitational softening in this simulation is on the order of 1 kpc. This means that even the largest of these giant molecular clouds are not resolved, and densities are instead averaged over larger regions and thus lower than they would be in resolved molecular clouds. If these lower densities fail to pass certain density thresholds at which shielding and molecule formation become effective, this could result in less molecular gas being formed overall. To test this hypothesis, future testing would need to explore higher resolutions in a cosmological context. Even increasing the star formation density threshold by a factor of 10 is not sufficient to counteract the effects of resolution observed here. This, in combination with the lack of HI discussed above, suggests other adaptations of the model may be necessary to account for lower resolutions and recover the full functionality of the chemical network in this regime. Caution needs to be taken in doing this, since in addition to increasing cosmological densities they may affect properties of galaxies and their evolution.

While it is clear that the chemical network model, at this resolution, predicts neither the cosmological density evolution of HI nor of H_2 as they are observed in our Universe, it remains to be seen how it compares to alternative approaches available to cosmological simulations. Figure 4.3 shows the cosmic density evolution of neutral atomic hydrogen in more detail, and in comparison to data obtained from other cosmological simulations in post-processing schemes. The shaded orange area corresponds to a range of values obtained by Rahmati

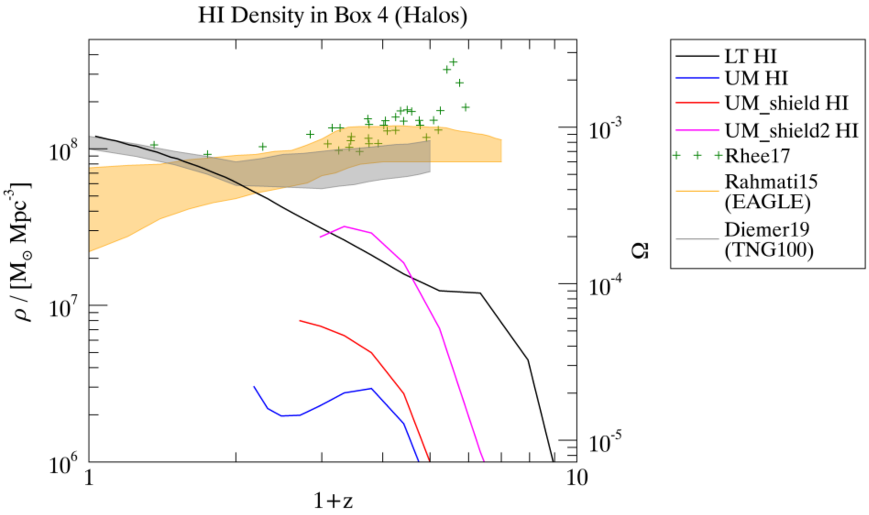

Figure 4.3: Redshift evolution of comoving cosmic HI density the different runs compared to data and other cosmological simulations. The range given by Rahmati et al. 2015 is obtained from post-processing of the EAGLE simulation, while Diemer et al. 2019 use Illustris TNG100.

et al. 2015 from variations of the EAGLE cosmological simulation (Schaye et al. 2014, Crain et al. 2015), which also uses the Gadget-3 code. The gray range is taken from Diemer et al. 2019, who apply a variety of models to obtain HI fractions for the IllustrisTNG100 simulation (Nelson et al. 2019), which uses the moving-mesh code Arepo. The observational data used for reference is the same as in Figure 4.2. Both simulations I compare to here fail to match observations across the entire redshift range. The EAGLE results show better agreement with high redshift observations but fall short at lower redshifts, while the IllustrisTNG data are a better match at low redshifts but do not capture the evolution at high redshifts well. Both, however, reach agreement with observations on the order-of-magnitude level over the entire redshift range, which the chemical network approach tested here fails to do. It should be noted that the post-processing schemes used in both references require additional model assumptions and have to be tuned to observations. They also crucially do not allow this data to be used in real-time to affect star formation or cooling. With this in mind, the chemical network's failure to match neutral and atomic hydrogen abundances compared to post-processing methods should not be cause to abandon the model, but to adapt it to function at this resolution.

4.2 Effects on Galaxy Formation and Evolution

In addition to enabling studies of cosmological densities, the full box provides a large number of galaxies with a wide range of masses. This allows for a statistical analysis of galaxy properties which can shed light on how the implementation of the chemical network affects galaxy formation and evolution.

Figure 4.4 shows the distribution of stellar masses among the galaxy population, also called the stellar mass function (SMF), for the test runs of Box 4. All models show reasonable agreement with observational data from Tomczak et al. 2014 (green shaded area). The first shielding runs (red squares) and the chemical network run without shielding (blue crosses) additionally match the curve of a double Schechter fit to the data (green line) by Tomczak et al. 2014. All four runs produce a greater number of halos at the high mass end than expected from observations, but it should be noted that the highest mass bins only contain

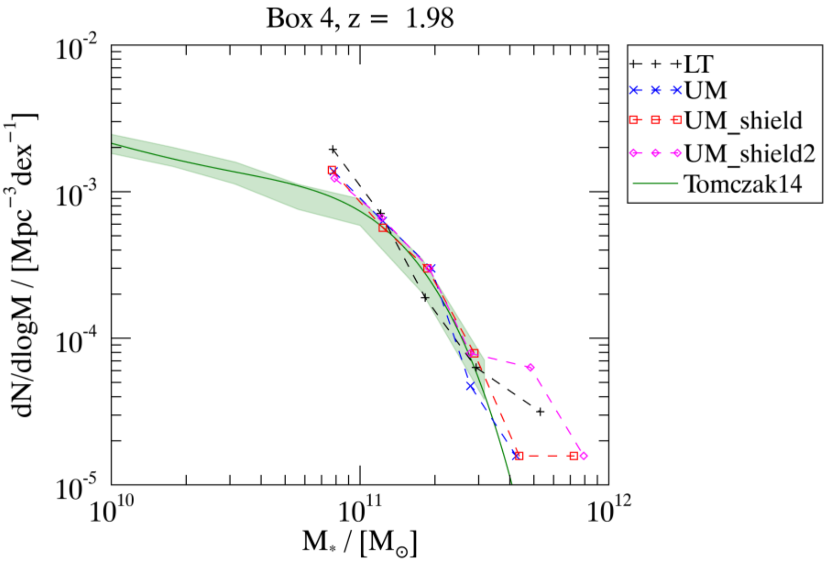

Figure 4.4: Stellar mass function (SMF) of galaxies in Box 4 with $M_* > 10^{11}\ M_\odot$. The green line is a double Schechter fit to ZFOURGE/CANDELS data from Tomczak et al. 2014. The green shaded area covers the data range and scatter.

a few halos each and are thus subject to low number statistics. In addition the highest mass bins in the simulations lie beyond the range in which the fit is constrained by observational data. Only galaxies with $M_* > 5 \cdot 10^{10}\ M_\odot$ from the simulations were selected to limit resolution effects on galaxy properties. This lower mass limit corresponds to about $1.5 \cdot 10^3$ star particles in the smallest galaxies. For the comparison to observational data the lowest mass bin was set at $M_* > 10^{10.75}\ M_\odot$, slightly above the initial mass cut, in order to match the mass binning employed by Tomczak et al. 2014. In the lowest mass bin, the simulations all overshoot the observed SMF. Whether this is due to resolution issues or if other effects lead to overproduction of stars in low mass halos is beyond the scope of this work. It has been suggested that this well-known problem is due to the implementation of stellar winds in the simulation, which assumes a constant velocity for the ejected gas (Hirschmann et al. 2014).

Simulation Name	**LT**	**UM**	**UM_shield**	**UM_shield2**
$N(M_* > 5 \cdot 10^{10}\ M_\odot)$	305	231	241	211
$N(\mathrm{SFR} = 0)$	105	114	118	55
$N_{\mathrm{quiescent}}$	136	130	135	59
Quenched Fraction	0.445	0.563	0.560	0.280

Table 4.2: Comparison of the total number of galaxies above the mass cut and with zero star formation, as well as the number of quiescent galaxies and the corresponding quenched fraction, between all four simulations at redshift 2. The criterion for quiescence, SSFR/$H(z) < 0.3$, was adapted from Franx et al. 2008.

Figure 4.5 shows the relation between stellar mass (M_*) and star formation rate (SFR) for all galaxies in all four test runs with $M_* > 5 \cdot 10^{10}\ M_\odot$ at $z \approx 2$. The total number of halos clearing the mass threshold at this redshift is about 30-40% lower in the runs with the chemical networks (see Table 4.2), their distribution in the $M_* -$ SFR plane is practically unchanged. The bulk of star forming galaxies lie along the star forming main sequence when compared to observational data, represented by a fit from Pearson et al. 2018, with some quenched galaxies residing at lower SFRs in the diagram. Thus, it seems that the alternative

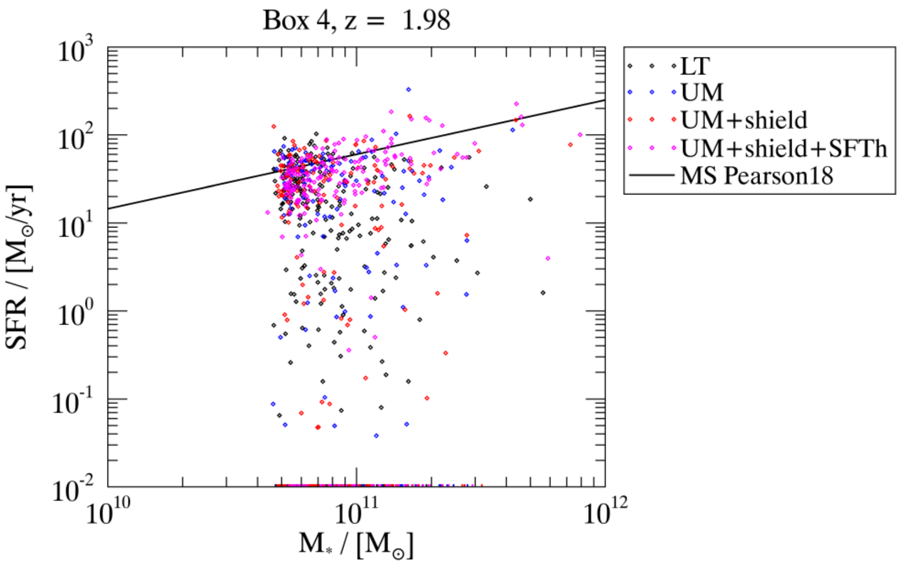

Figure 4.5: Comparison of the stellar mass - star formation rate distribution of galaxies in the different test runs and the observed star forming main sequence of galaxies at this redshift (Pearson et al. 2018). Galaxies with no ongoing star formation at this redshift are represented by the vertical dashes at the bottom of the plot.

cooling model slightly inhibits the formation of galaxies in the mass range considered here but those galaxies contain and produce the same amount of stars as in the base line run.

The same appears to hold true for other global galaxy properties. Figure 4.6 shows the specific angular momentum (j_*) of the stellar component in relation to its mass for the same subset of halos as in Figure 4.5. While values for individual galaxies may change between runs, the overall distribution exhibited by the population remains virtually the same. Note that all models produce a distribution of galaxies that seems heavily skewed towards ellipticals rather than disc galaxies when compared to our own Universe. This is likely an effect of the relatively low resolution of these simulations, at which stellar discs are not resolved.

Expanding this analysis to halo properties beyond the stellar component alone, Figure 4.7 shows the stellar mass fraction against the total halo mass within the radius where the density exceeds 200 times the mean background density in the simulation (M_{200}). The stellar mass fraction is scaled by the cosmic baryon fraction $\Omega_\mathrm{b}/\Omega_\mathrm{m} = 0.168$ used throughout all runs. Again, the statistical distributions are very similar between all models.

Reproducing these global halo parameter distributions is an important step in successfully implementing cooling via the chemical network. The model used as a base line here has its sub grid physics set up to produce galaxies as they are observed in our reality, as evidenced by the model agreement with the observations shown here. If the alternative cooling treatment were to result in significant deviations from these relations, this would hint at a failure of the model to mimic some of the relevant physical processes in galaxy formation. These global properties, however, do not reveal much about the internal structure and matter distribution within the galaxies. A detailed analysis in this direction is difficult at this resolution, and care needs to be taken in separating physical effects from those produced by softening at the resolution limit.

Figure 4.8 shows the mass-size relation of the stellar component of all galaxies in Box 4 above the lower mass limit. This simple measure for the compactness of galaxies gives some insight into their internal structure. It should be noted once again that the complete populations exhibiting more elliptical or early type like features is likely a consequence of the low resolution and thus present in all runs. The base line model and the first two

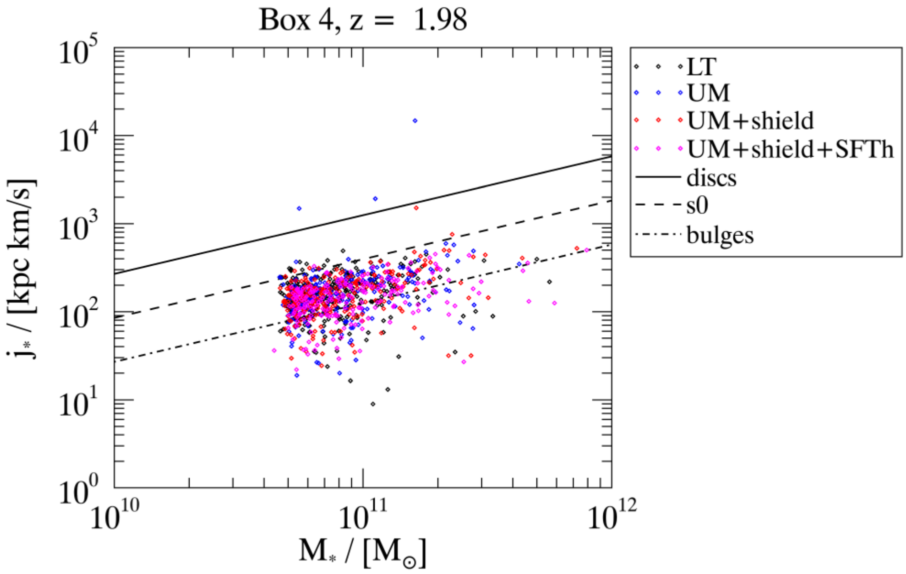

Figure 4.6: The stellar mass - stellar angular momentum distribution of galaxies in the different test runs of Box 4. The lines separating different galaxy morphologies are adapted from (Teklu et al. 2015) and scaled to $z = 2$ according to theoretical predictions by Obreschkow et al. 2015.

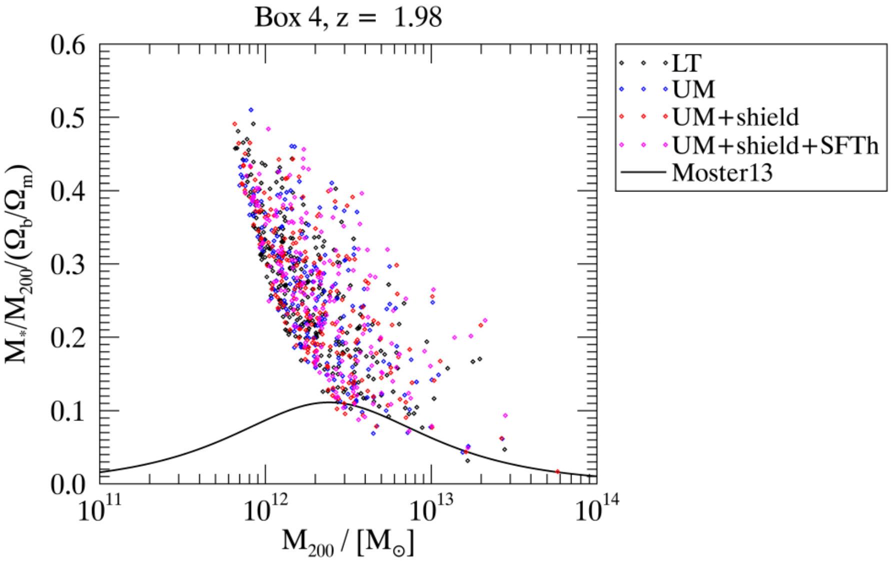

Figure 4.7: Comparison of the halo mass - stellar mass distribution of galaxies in the different test runs. Also shown is an empirical model prediction by Moster et al. 2012. Only main halos are shown in this comparison because overdensity based radii like R200 cannot be determined for sub halos and consequently neither can the corresponding masses.

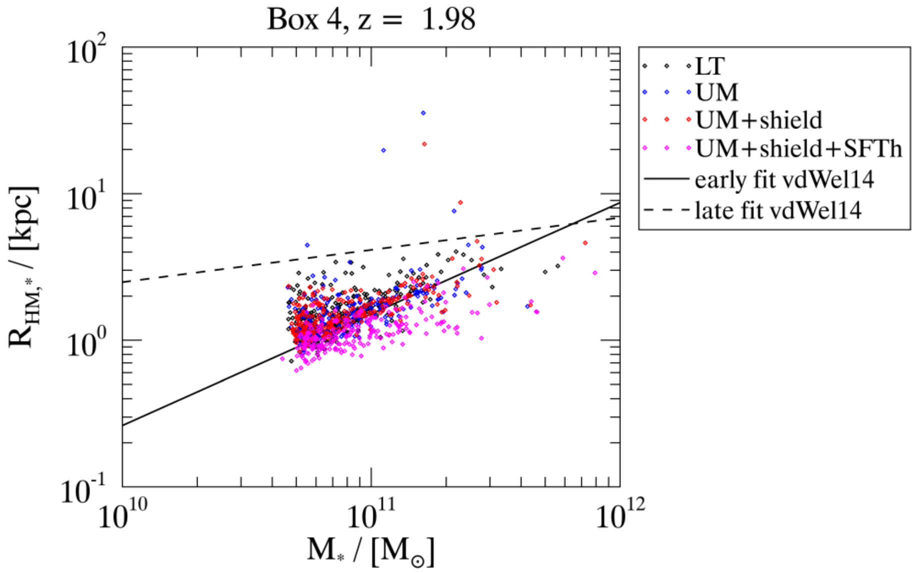

Figure 4.8: Comparison of the stellar mass - stellar half-mass radius distribution of galaxies in the different test runs of Box 4 with observations at this redshift (van der Wel et al. 2014).

runs with the chemical network again show no discernible difference in their overall galaxy properties and match observations, while the second shielding run on average shows lower stellar half mass radii $R_{\mathrm{HM},*}$ at fixed stellar masses. In addition to producing more compact galaxies, the resulting scaling relation between M_* and $R_{\mathrm{HM},*}$ is also noticeably flatter than the corresponding fit to observations by van der Wel et al. 2014. The shift in the mass-size relation is likely an effect of over cooling due to the increased density threshold for star formation in the second shielding run, which was deemed necessary to reach more realistic abundances of molecular hydrogen. This suggests that the density threshold cannot be used as a sole parameter to adapt the model to lower resolutions without breaking galaxy formation and evolution, arguably the core aspect of cosmological simulations. Whether this problem remains at higher resolutions, where the stellar mass-size relation should not exhibit the same overall bias toward more compact ellipticals, will have to be answered in future studies.

It is worth noting that the second shielding run was able to reproduce many of the observed distributions of global galaxy properties rather well while actually forming overly compact galaxies. In particular among the tested cooling implementations it best matched the curve of the stellar mass function which is often used as a benchmark for simulations. This should act as a cautionary tale not to rely solely on global galaxy properties like the SMF to tune simulations but to take into account the distribution of matter within galaxies as well.

Chapter 5

Cold Gas Evolution in Individual Galaxies

Where the cosmological box supplied a great number of halos, zoom simulations focus on a single target and its environment. In the process we trade a sample of galaxies representative of the population in the Universe at large for a detailed look at the formation history and evolution of a single one in its cosmological context. This should provide insight as to when and where cold and molecular gas forms in a galaxy, and how this affects the evolution of its stellar component.

In addition, the zoom-ins may help answer questions left open by the resolution limits of the cosmological box. Besides the very clear issues in trying to analyze galaxy morphologies and the evolution of cold gas within individual halos at box resolution, it is also possible that increasing the resolution would affect the overall fraction of molecular gas. Molecules require high density environments to form, which may be beyond what the resolution of our Box 4 runs permits. This section aims to resolve these matters by analyzing the results of two suits of zoom simulations at a resolution about 25 times that of Box 4.

Simulation Name	**LTDef**	**LT5**	**UMDef**	**UM5**	**SHDef**	**SH5**	**SHnoUVB**
Chemical Network	No	No	Yes	Yes	Yes	Yes	Yes
UV Background	Yes	Yes	Yes	Yes	Yes	Yes	No
Shielding	No	No	No	No	Yes	Yes	Yes
SF Threshold [cm^{-3}]	2.0	5.0	2.0	5.0	2.0	5.0	5.0

Table 5.1: Simulation parameter comparison for the different model implementations in the cosmological zoom-in runs of Dfrogin at the 25x resolution.

In order to test the chemical network and HI self-shielding models, as well as the effect of an increased density threshold for star formation, a suit of six zoom simulations was initialized with identical initial conditions derived from the Dianoga dark matter only simulation for each target. This suite covers three different sub grid implementations of gas cooling. The base line model (labeled LT) interpolates the cooling function from tabulated values based on temperature, density and metallicity as described in Chapter 2. In the second variation (labeled UM) contributions from individual gas species are taken into account with the addition of the chemical network as described in Chapter 3. For the third implementation (labeled SH) HI self-shielding is added to the chemical network. All three models were run with two different star formation density thresholds. The fourth variation is run with no UV background, to serve as an indicator of how effective molecular gas formation is in the model. This can be thought of as the maximum possible shielding effect, since shielding effectively attenuates the UV background, but is of course unphysical. A resolution corresponding approximately to 25 times the base resolution of Box 4 (25x) was chosen as the compromise

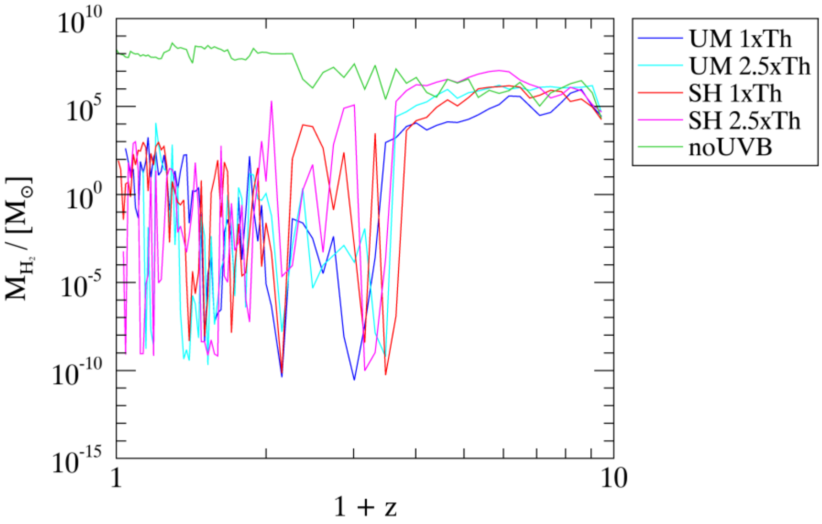

Figure 5.1: Comparison of Dfrogin's molecular hydrogen mass evolution with redshift in the five different runs with the chemical network at 25x resolution.

between increased detail and the feasibility of running multiple simulations in order to test model variations.

For the most part, this chapter will focus on Dfrogin which is about a factor of 10 more massive than Asin, the other candidate. The greater number of particles in Dfrogin paint a somewhat more detailed picture of the distribution of matter in the galaxy throughout its evolution, making it the better choice for a detailed analysis. Since the results concerning the chemical network model from the Asin runs agree with those of Dfrogin presented here, they are not discussed separately, but can be found in Appendix A.

5.1 Cold Gas Content

Figure 5.1 shows the redshift evolution of the molecular gas mass of the target object Dfrogin in the four runs with chemical network cooling. It is immediately clear that, at redshifts below ~ 3, any differences between the runs are overshadowed by rapid changes over several orders of magnitude in mass. This is an indicator that the total mass of molecular hydrogen (M_{H_2}) is very low, such that small changes affect it disproportionately. Indeed, when comparing Dfrogin to galaxies observed at low redshifts in the xGASS (Catinella et al. 2010) and COLD GASS (Saintonge et al. 2011) surveys, as is done in Figure 5.2, we see that Dfrogin lies at least five orders of magnitude below the surveyed galaxies in molecular gas mass throughout the redshift range of the surveys (z = 0-0.5). During the rapid changes in molecular gas mass at these redshifts, it even falls as far as 20 orders of magnitude below observations, which essentially means it is completely depleted of molecular gas. This is underlined by the variations in the maximum molecular hydrogen fraction ($f_{H_2,\mathrm{max}}$) of all gas particles in the galaxy shown in Figure 5.3. In all runs with a UV background this maximum reaches the model imposed floor of 10^{-20} at some redshifts. There is no significant difference between the models with shielding and those without at redshifts below $\sim$ 3, neither in total H_2 mass nor maximum H_2 fraction. This suggests that the shielding implementation does not work effectively at the 25x resolution. Interestingly, even in the run with no UV background radiation in the model the H_2 levels do not rise to what is observed at lower redshifts. This means that no amount of shielding can match observations in this configuration of the chemical network, since it only serves to attenuate the UV background. Most likely

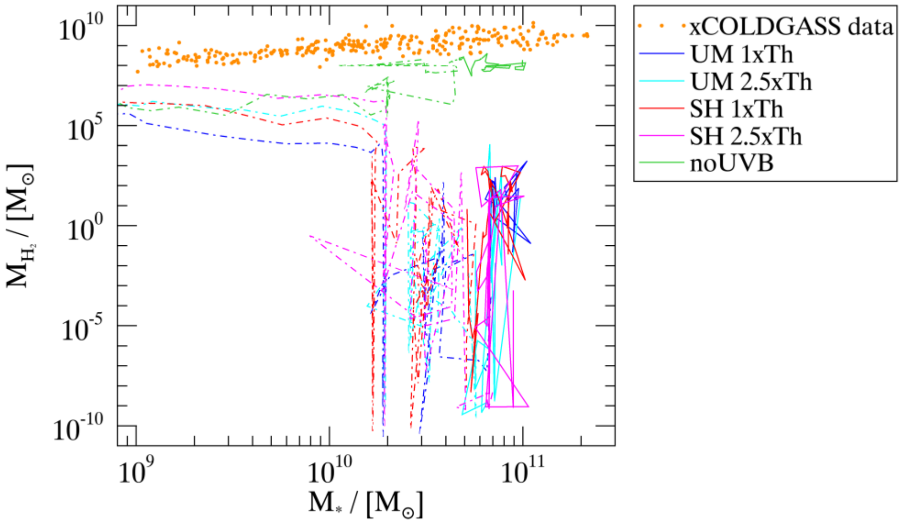

Figure 5.2: Comparison of Dfrogin's track in the M_*-M_{H_2} diagram with observations from the COLD GASS survey (Saintonge et al. 2011). The part of the track for each model that lies within the redshift range of the data (0-0.5) is represented by a solid line, while dashed lines show the evolution at higher redshifts and are thus not directly comparable to the data.

other formation channels for molecular gas, like dust catalyzed processes, would be needed to achieve agreement here.

Figure 5.4 shows Dfrogin compared to the same combined xGASS and COLD GASS data with the neutral atomic hydrogen mass (M_{HI}) plotted against stellar mass. For the chemical network runs Dfrogin's track in the M_*-M_{HI} plane shows the same characteristics as that in the M_*-M_{H_2} plane, with stable gas mass levels at low redshifts and erratic, fast changing M_{HI} at low redshifts. The gap between peaks in the simulated galaxy's evolution and xGASS data is noticeably smaller here than in H_2, but nonetheless clearly present. The base line runs match the xGASS data well, mirroring the agreement found at low redshifts in the full cosmological box. In the test run without UV background a similar agreement with the data is reached, suggesting that the shielding mechanism, in principle, can bridge the gap between chemical network and observations. However, it should be noted once again that this run corresponds to every gas particle experiencing the maximum effect of shielding, which of course does not in any way reflect the physical reality. While the results for the H_2 masses clearly suggest that an adaptation of the chemical network is necessary, it seems at least possible that an increase in resolution, and the resulting more effective shielding, could bring the model predictions for HI in line with observations.

For a clearer representation of how the galaxy evolves with time Figure 5.5 shows Dfrogin's HI mass by redshift. Any differences between the chemical network models at higher redshifts, where the HI mass is still relatively stable, barely exceed the range of fluctuations within the models. Interestingly, the dividing line is not between shielding and non-shielding models, as was the case for H_2, but between low and high star formation threshold density. However, given the even smaller magnitude of the effect here than in the M_{H_2} evolution, it is difficult to draw any conclusions from this. The rapid fluctuations at lower redshifts ranging over several orders of magnitude, much like the fluctuations in H_2 levels, suggest that the galaxy contains mostly hot gas with very low HI levels, such that small fluctuations in absolute HI mass have severe effects relative to the total.

From this it is already clear that even at 25 times the resolution of the cosmological box, the chemical model still fails to accurately predict the abundance of cold gas in galaxies. It

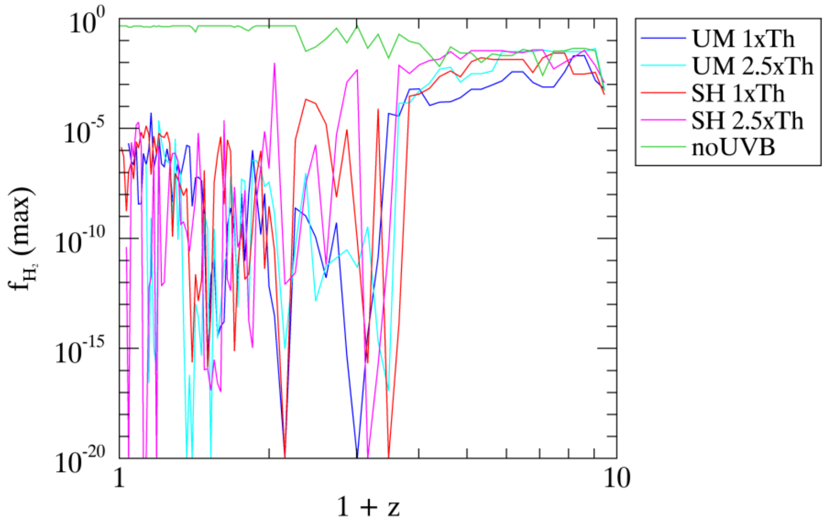

Figure 5.3: Maximum molecular hydrogen fraction in gas particles bound to Dfrogin by redshift. Note that the model imposes a floor of 10^{-20} on species abundances.

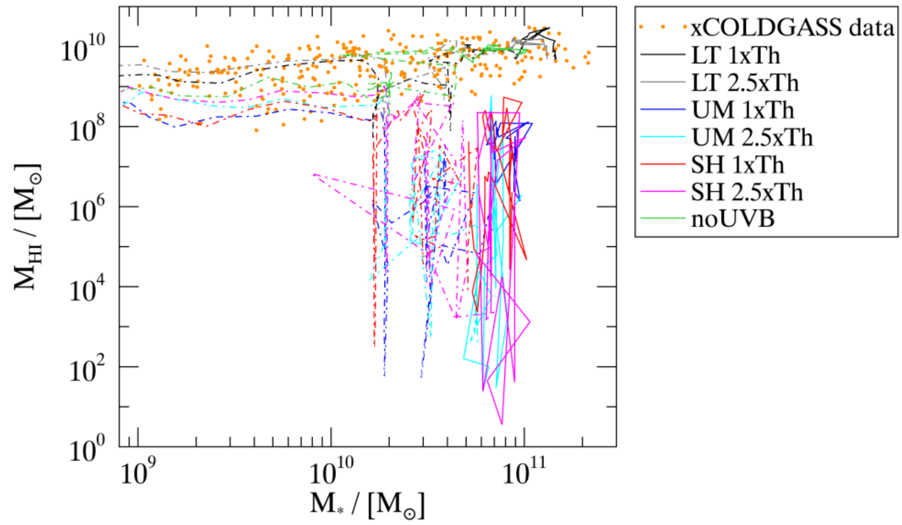

Figure 5.4: Comparison of Dfrogin's track in the M_*-M_{HI} diagram with observations from the xGASS survey (Catinella et al. 2010). The part of the track for each model that lies within the redshift range of the data (0-0.5) is represented by a solid line, while dashed lines show the evolution at higher redshifts and are thus not directly comparable to the data.

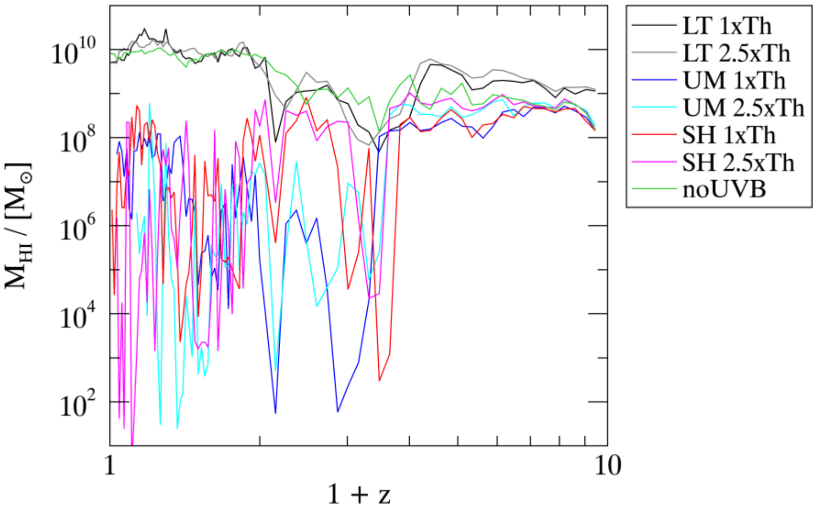

Figure 5.5: Comparison of Dfrogin's neutral atomic hydrogen mass evolution with redshift between all seven runs at 25x resolution.

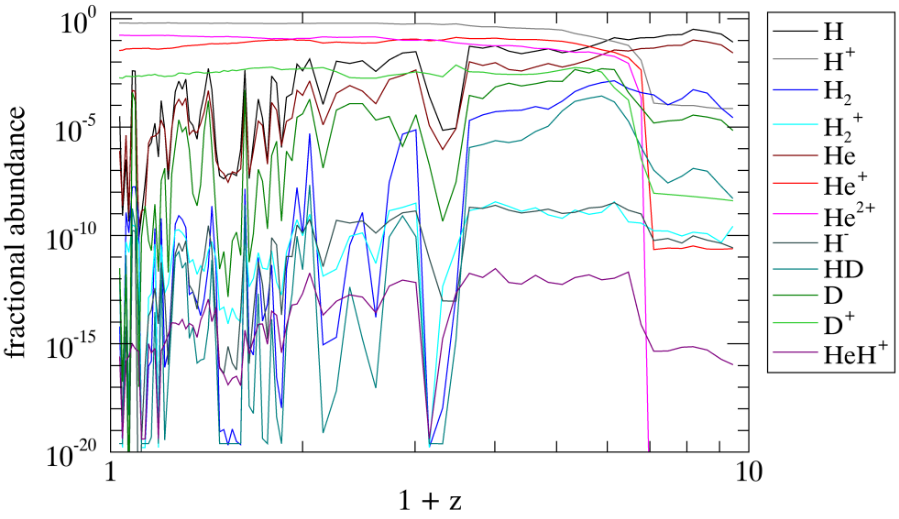

Figure 5.6: Redshift evolution of the abundances in Dfrogin of all chemical network species for the SH5 run.

remains to be seen how cooling, and as a consequence star formation, is affected by this. As shown in Chapter 3, H_2 is only partially responsible for low temperature cooling, and for some range of typical conditions is not even the dominant coolant. In principle, it would thus be of great interest to compare the abundance of other gas species directly to observations, but due to the lack of observational data, this is not possible for the likes of HD and other crucial coolants. However, the other molecules in the network, in particular HD and H_2^+, require conditions to reach stable abundances in the cold gas phase that are similar to those for molecular hydrogen. This can be seen in Figure 5.6 where the abundance curves of both HD and H_2^+ follow similar patterns to that of H_2.

5.2 Gas Distribution and Dynamics

A direct comparison between local gas density in Dfrogin and the required threshold for effective HI self-shielding is necessary to ascertain where in the galaxy shielding plays a role. To this end, Figure 5.7 shows the evolution of Dfrogin's radial gas density profile over a range of redshifts. Up to about $z = 3$ all models are in agreement, but between $z = 3$ and $z = 2$ the chemical network variations lose significant amounts of gas particularly towards the center. This is also reflected in the evolution of the overall gas mass of the galaxy shown in Figure 5.8. As a consequence, none of the chemical network models reach densities above 10^4 $M_\odot \mathrm{kpc}^{-3}$ after $z = 2$ at the length scales imposed by the radial binning process. For HI self-shielding to be effective the model requires physical gas densities of $\gtrsim 10^5$ $M_\odot \mathrm{kpc}^{-3}$ as can be seen in Figure 3.4. These low average densities might be the reason why there is no significant difference in H_2 evolution after $z = 2$ between the shielding and non-shielding runs.

Radially binning particles to calculate a density has the disadvantage of smearing out small high density regions, thus lowering the peak densities reached by the resulting profile. The first panel of Figure 5.9 shows the gas density used in Gadget's internal calculations, transformed into physical units, for all particles with $T > 10^4$K projected in the x-y-plane. While the same trend of drastically dropping densities throughout the galaxy after $z = 3$ remains clearly visible, this visualization also shows that small pockets of cold gas with densities above the threshold for effective shielding remain even down to the lowest redshifts. However, these account for only a small fraction of the total gas mass, explaining why shielding has a negligible effect on the total H_2 mass at lower redshifts. The second panel shows the abundance ration of molecular to atomic hydrogen in the same subset of gas. Regions with a high [H_2/HI] tend to correspond to regions of high physical gas density which is expected, given that high densities facilitate H_2 formation and HI self-shielding. So while it is true that the radial binning concealed some small high density regions in which shielding should be somewhat effective, the two dimensional density maps reinforce the notion that the vast majority of gas in the zoomed-in galaxies at 25x resolution experience practically no shielding. Indeed, there is practically no cold gas left in the galaxy at $z = 0$. The two dimensional visualization also shows the halo noticeably disrupted around $z = 2$ which explains the erratic radial density profile for that redshift in Figure 5.7.

To get a better idea of how the cold gas evolves differently across the suite of simulations, Figure 5.10 shows the same distribution and density projections as Figure 5.9 for all runs. Only in the base runs (first two rows) and the test run without UV background (last row) does Dfrogin retain significant levels of cold gas at low redshifts. Moreover, where in the base runs the cold gas is surrounded by an ‘atmosphere’ of hot gas (grey points in Figure 5.10), the chemical network runs show an irregular, and much thinner, structure in the hot gas. The base runs also show a much higher number of hot gas particles in the galaxy, which matches the result of the halo gas mass comparison in Figure 5.8, but nonetheless goes against any expectations for the chemical network model. A possible explanation for this behavior might

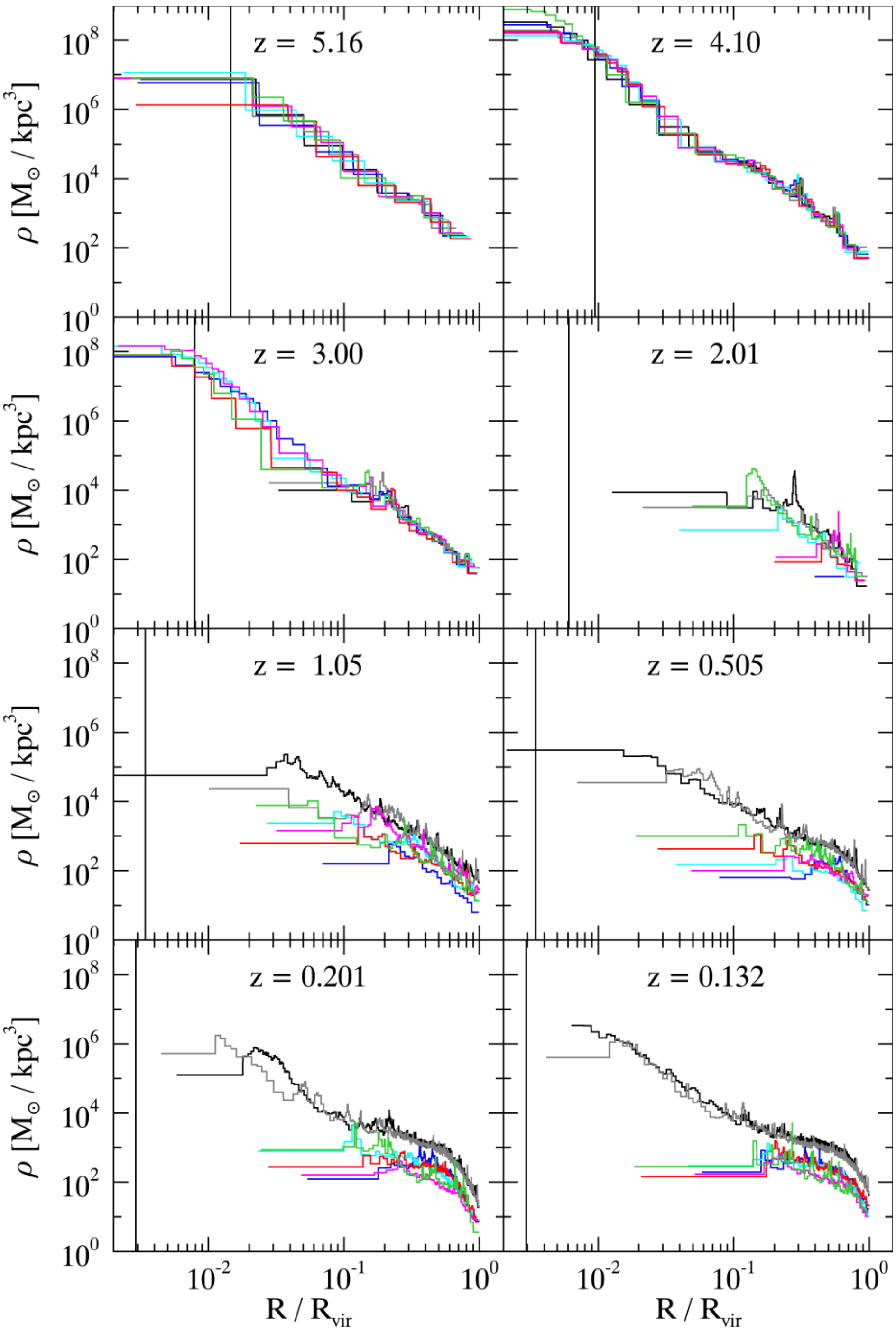

Figure 5.7: Radial gas density profiles of Dfrogin at selected redshifts on a double log-scale. Each bin contains 200 gas particles. The color scheme for the seven different runs is the same as in Figure 5.2 with the addition of black and gray lines for the LTDef and LT5 base runs respectively. The vertical black line denotes the physical softening for gas particles at that redshift.

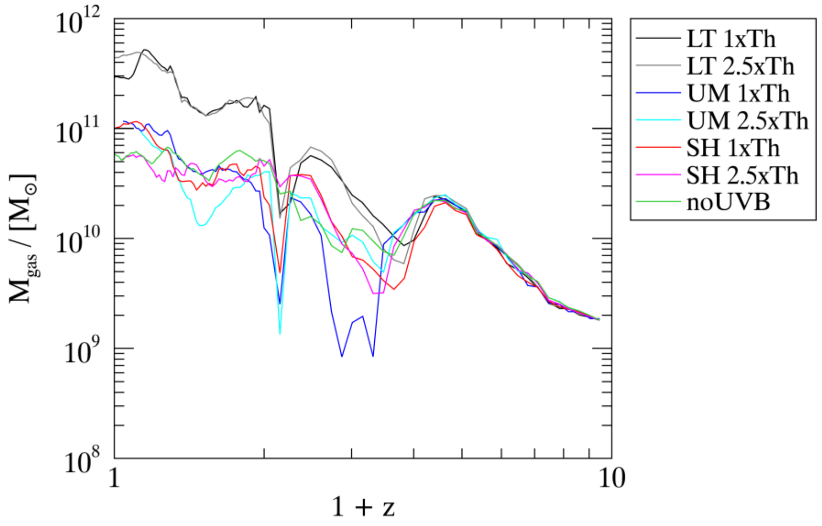

Figure 5.8: Comparison of the total bound gas mass evolution with redshift in the seven different runs of Dfrogin at 25x resolution.

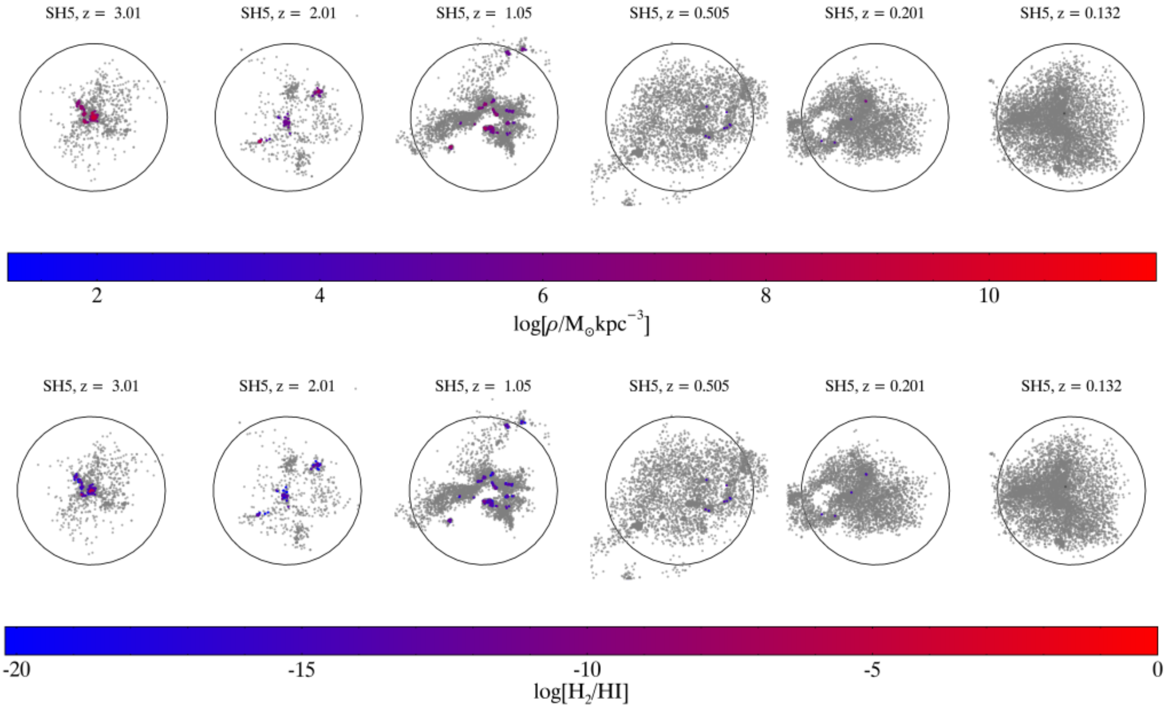

Figure 5.9: Physical density of cold gas (top) and abundance ratio of molecular to atomic hydrogen (bottom) for the SH5 run of Dfrogin. Particles colored according to the scale have $T > 10^4$K while gray particles correspond to hot gas. Positions are scaled to the Virial radius, indicated by the black circle, at each redshift.

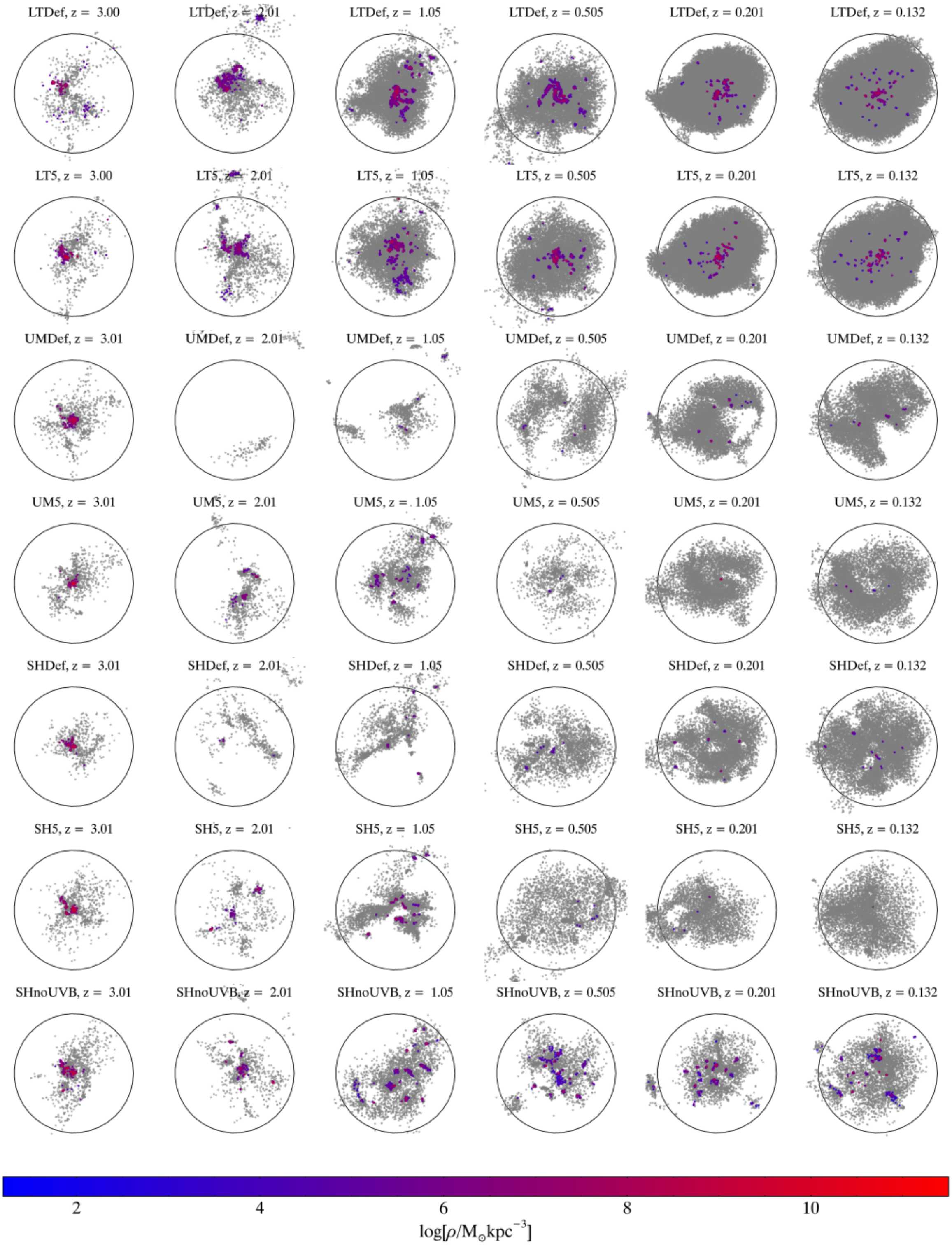

LTDef, z = 3.00
LTDef, z = 2.01
LTDef, z = 1.05
LTDef, z = 0.505
LTDef, z = 0.201
LTDef, z = 0.132
LT5, z = 3.00
LT5, z = 2.01
LT5, z = 1.05
LT5, z = 0.505
LT5, z = 0.201
LT5, z = 0.132
UMDef, z = 3.01
UMDef, z = 2.01
UMDef, z = 1.05
UMDef, z = 0.505
UMDef, z = 0.201
UMDef, z = 0.132
UM5, z = 3.01
UM5, z = 2.01
UM5, z = 1.05
UM5, z = 0.505
UM5, z = 0.201
UM5, z = 0.132
SHDef, z = 3.01
SHDef, z = 2.01
SHDef, z = 1.05
SHDef, z = 0.505
SHDef, z = 0.201
SHDef, z = 0.132
SH5, z = 3.01
SH5, z = 2.01
SH5, z = 1.05
SH5, z = 0.505
SH5, z = 0.201
SH5, z = 0.132
SHnoUVB, z = 3.01
SHnoUVB, z = 2.01
SHnoUVB, z = 1.05
SHnoUVB, z = 0.505
SHnoUVB, z = 0.201
SHnoUVB, z = 0.132

Figure 5.10: Physical density of cold gas in all test runs of Dfrogin from $z = 3$ to $z = 0.13$. Particles colored according to the scale have $T > 10^4$K while gray particles correspond to hot gas. Positions are scaled to the Virial radius, indicated by the black circle, at each redshift.

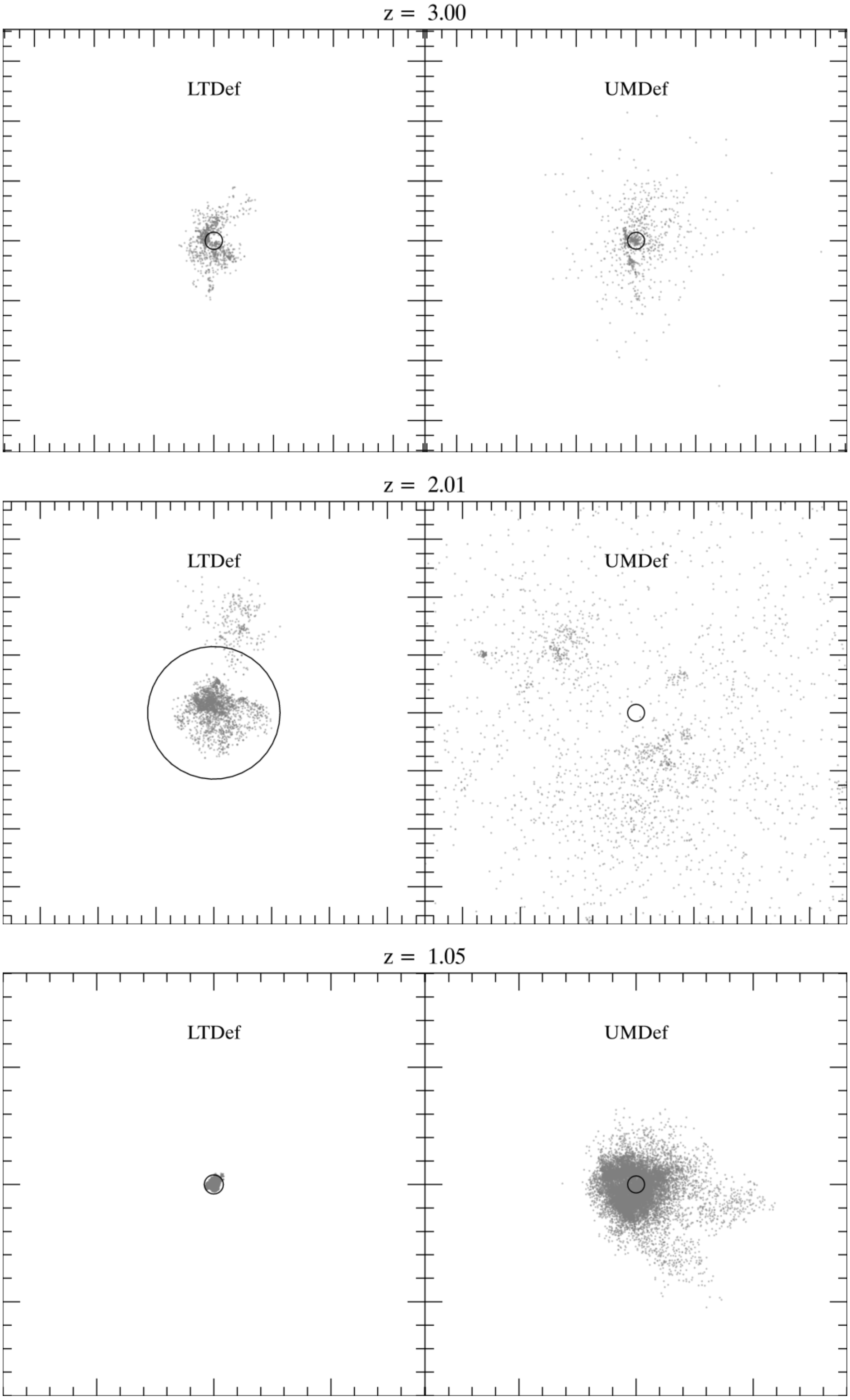

Figure 5.11: Spatial distribution of hot gas particles that are identified in the LTDef run as part of the target halo Dfrogin, shown for both the LTDef and UMDef simulations. Black circles indicate the virial radius of the respective galaxy. Note that the large virial radius for the LTDef run in the middle panel is likely due to an ongoing merger at this redshift. The range of both plots is identical and covers a $(50R_{\mathrm{vir,UMDef}})^2$ square in code units.

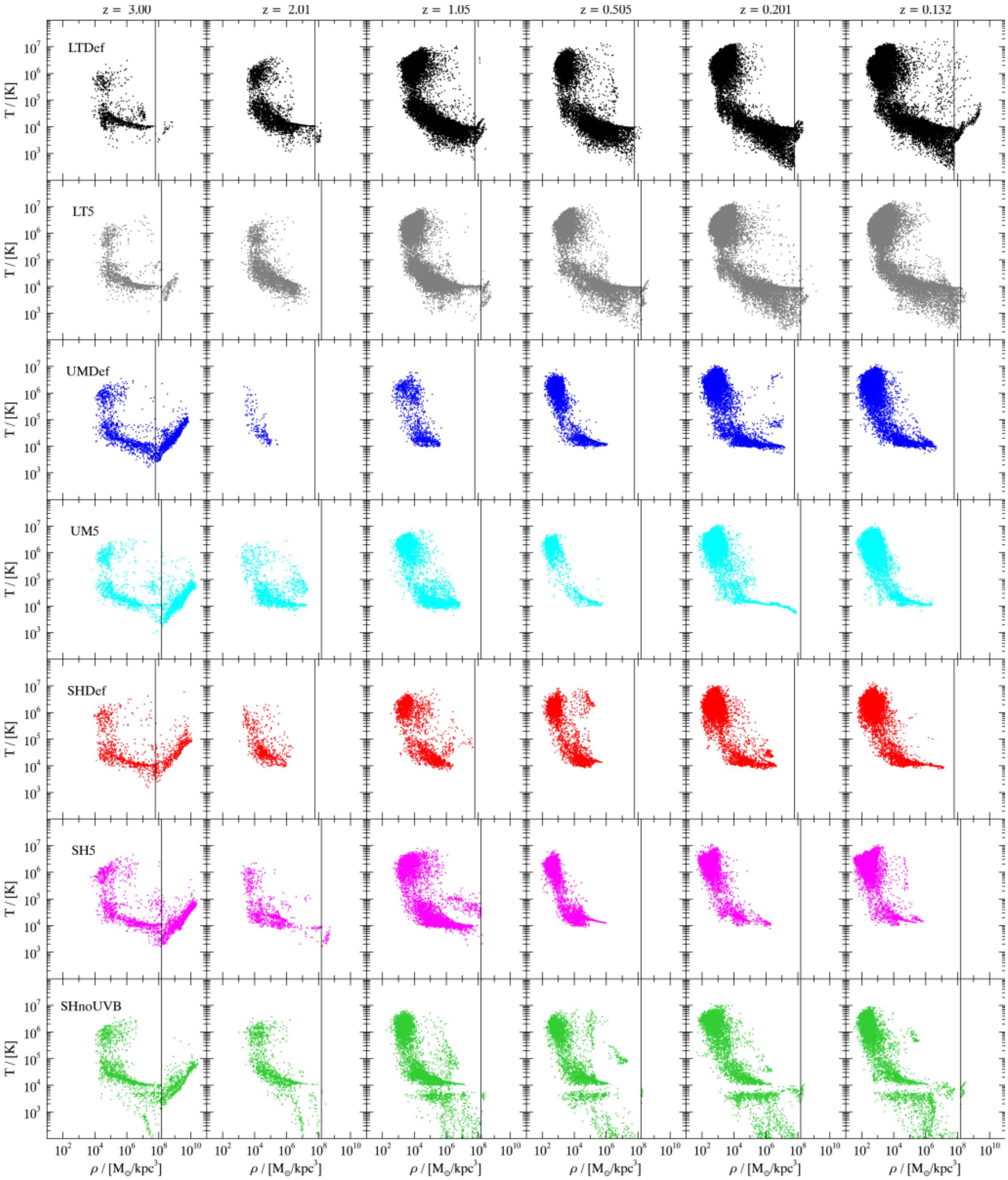

Figure 5.12: Phase diagram of gas in all test runs of Dfrogin from $z = 3$ to $z = 0.13$. From top to bottom the models shown are: LTDef, LT5, UMDef, UM5, SHDef, SH5, and SHnoUVB all in the familiar color scheme. The vertical black line denotes the density threshold for star formation in each model assuming the average molecular mass to be 1.22.

be the interaction of stellar feedback with the chemical network. Since the model is added to the code parallel to the existing stellar evolution module, their interaction is not guaranteed to be self-consistent. Star formation may become excessive at an early redshift before the feedback can affectively slow it down. A similar process is imaginable for feedback from gas accretion onto the central black hole in the galaxy. If gas cooling is too efficient, it could provide so much matter for the black hole to accrete that the resulting feedback disrupts the entire galaxy. The disruptive event observed in the SH5 run at $z = 2$ is present to varying degrees in all chemical network runs, and could also be explained by either of these feedback effects.

To better understand the magnitude and nature of this disruption, I identified the SPH particles that make up Dfrogin's hot atmosphere in the base run LTDef, and located them in the chemical network run UMDef. While the evolution of individual particles is different between different runs, all simulations share the same initial conditions, so that the bulk of the particles should end up in the same target halo in each of them. Thus, the distribution of hot gas as shown in Figure 5.11 should serve as a reasonable approximation of what happens to the 'hot atmosphere' of Dfrogin in the chemical network runs. At redshift 3, before the complete disruption, both versions of the galaxy have a somewhat comparable extended hot gas component. This drastically changes at redshift 2 in the UMDef run, where the particles bound to Dfrogin in the LTDef run are scattered outwards to several tens of virial radii. In the LTDef run a merger can be seen at this redshift, which causes the virial radius to extend much further than in any of the other snapshots shown here. While there is once again a more recognizable structure at redshift 1, the hot gas in the UMDef run still extends far beyond Dfrogin's virial radius, which is why so little of it is found bound in the halo (Figure 5.10).

Looking at Dfrogin's gas component in the density - temperature space should reveal whether it provided the conditions necessary for excessive star formation or black hole accretion in the lead-up to its disruption. Figure 5.12 shows such phase diagrams for all gas bound in Dfrogin at the same redshifts as selected for the cold gas maps before. Indeed, in all chemical network runs there is far more gas in the star forming branch, left of the dividing line that denotes the star formation density threshold, at redshift 3 than in the base line runs. At redshift two we see the disruption taking hold, with less overall gas remaining in the chemical network runs and lower maximum gas densities, particularly in the non-shielding runs.

5.3 Effects on Star Formation

Having established the cold gas content of the zoom simulations to be severely lacking in both HI and H_2 and generally hotter and thinner than expected, it remains to be seen how the star formation fueled by this reservoir evolves over the course of the simulation, and if it is indeed the culprit in the galaxy's disruption. Figure 5.13 shows the total galactic star formation rate of Dfrogin with redshift. Once again the chemical network and base models diverge at a redshift of about 3. In the base model Dfrogin continues to form stars intermittently and at lower values than reached during the peak between redshifts 4 and 3. The chemical network models show the same peak, after which star formation remains at somewhat higher levels than in the base runs, before it ceases almost entirely except for occasional single snapshot peaks. Only the test run without UV background has the galaxy continuing star formation down to very low redshifts, much like the base model although with slightly smaller peak values. Star formation in the chemical network is exceeding the levels observed in the base line runs at redshift 3, which is consistent with the impression gained from the phase diagrams. Little ongoing star formation in the chemical network models at lower redshifts is also expected, given the temperature and density of the gas at these times.

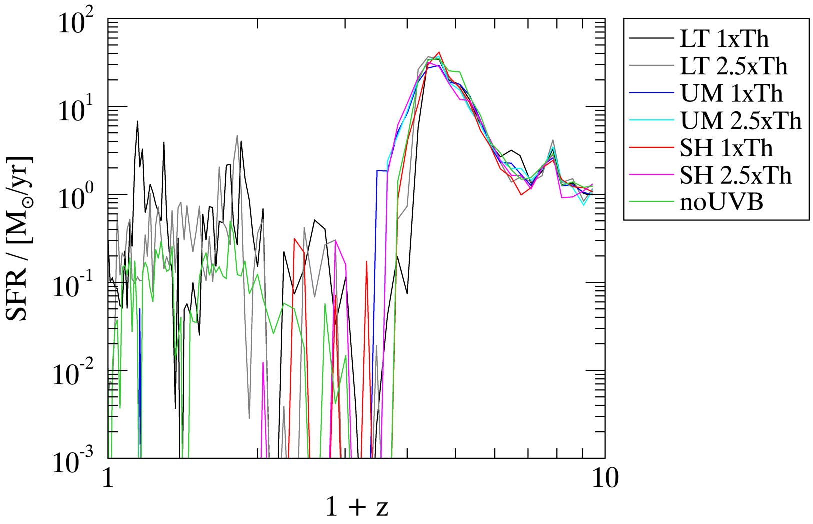

Figure 5.13: Comparison of Dfrogin's star formation rate evolution with redshift between all seven runs at 25x resolution. Any data points below the lower limit of the plot correspond to zero star formation in the entire galaxy at that redshift.

When comparing the resulting evolutionary track in a stellar mass star formation rate (M_*-SFR) diagram to observations, as is done in Figure 5.14, the lack of star formation at lower redshifts is even clearer to see. Even in the test run without UV background Dfrogin exhibits less star formation at low redshift than in the base model, indicating once again that photoionization and photoheating are not the only factors in the excessive removal of gas mass from the galaxy. In principle, gas could be removed by star formation transforming it into stellar mass. To rule out the possibility one only has to take a look at Figure 5.15 which shows the evolution of Dfrogin's total baryonic mass ($M_* + M_{\mathrm{gas}}$) with redshift. All implementations of the chemical network model stay behind the base runs in baryonic mass after $z = 2.5$, even the run without UV background. This once again points to disruption and ejection of the gas from the galaxy.

While the zoom simulations do not permit a statistical analysis of the mass size relation, the target galaxy's track in the M_*-$M_{\mathrm{HM},*}$ plane can still provide valuable insight. Comparing the galaxy's position in the M_*-$M_{\mathrm{HM},*}$ plane at a single fixed point in time between different runs directly can be difficult, because mergers and close encounters significantly alter the calculated size of the galaxy, and such events may not happen at the exact same time in different runs. However, a systematic difference between models affecting galaxy morphology, as might be the case with the disruption of the gas component discussed above, should lead to significant changes to evolution tracks in the mass-size plane. Figure 5.16 shows the evolution tracks of the Dfrogin and Asin target galaxies in the M_*-$M_{\mathrm{HM},*}$ plane for all test runs at redshifts below 2.75, with fits to observational data from van der Wel et al. 2014 for reference. The most notable change in the chemical network runs is that Dfrogin grows to at least twice the size compared to the base line runs, despite its stellar mass remaining lower. This fits with the picture of a gas poor galaxy that presented itself throughout the analysis so far. The gas poor or 'dry' mergers such a galaxy would predominantly experience, would grow its size much more than gas rich 'wet' mergers would, as has been shown in numerical simulations (Hilz et al. 2012). Asin, the second zoom-in target, also has a lower stellar mass at the end of its evolution in the chemical network runs compared to its base line simulation, but it does not show the same increase in size as Dfrogin. Given its much smaller mass compared to Dfrogin, it is expected to experience fewer mergers throughout its evolution,

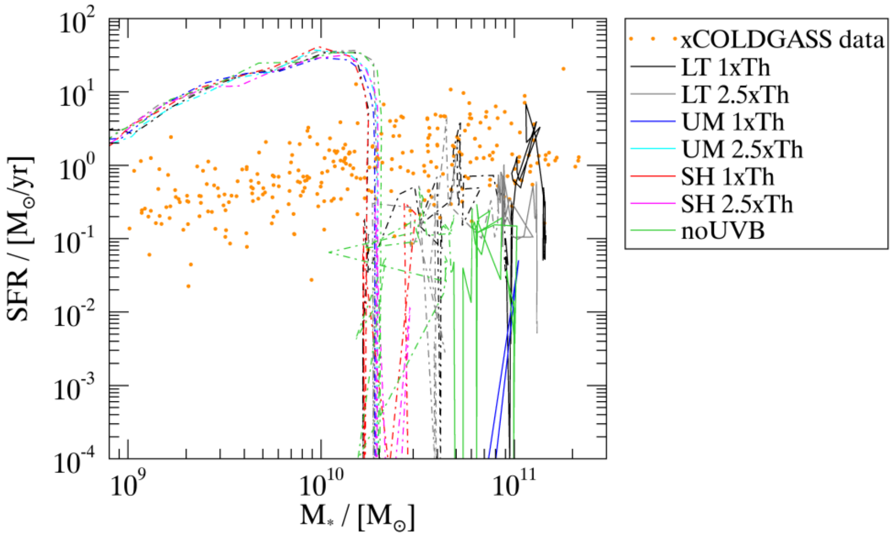

Figure 5.14: Comparison of Dfrogin's track in the M_*-SFR diagram with xGASS and xCOLDGASS data (Catinella et al. 2010, Saintonge et al. 2011). The part of the track for each model that lies within the redshift range of the data (0-0.5) is represented by a solid line while dashed lines show the evolution at higher redshifts and are thus not directly comparable to the data.

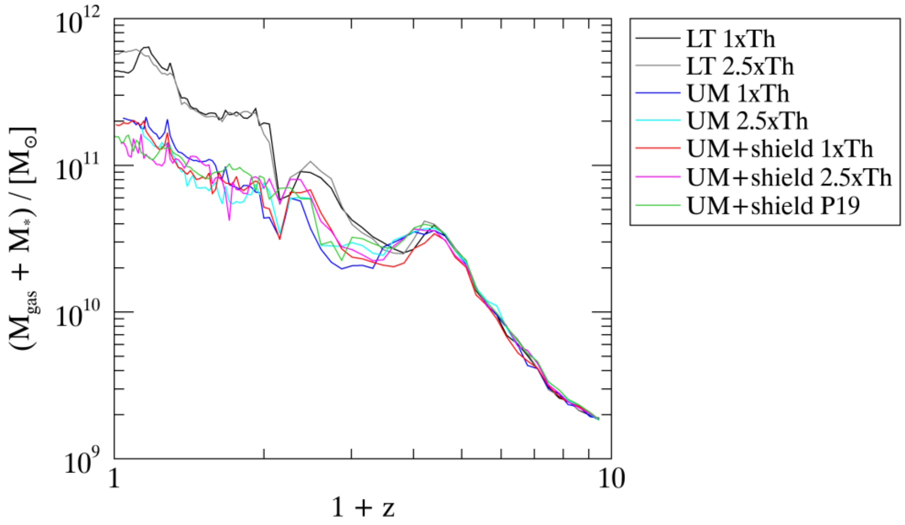

Figure 5.15: Comparison of Dfrogin's total baryonic mass (gas + stars) evolution with redshift between all seven runs at 25x resolution.

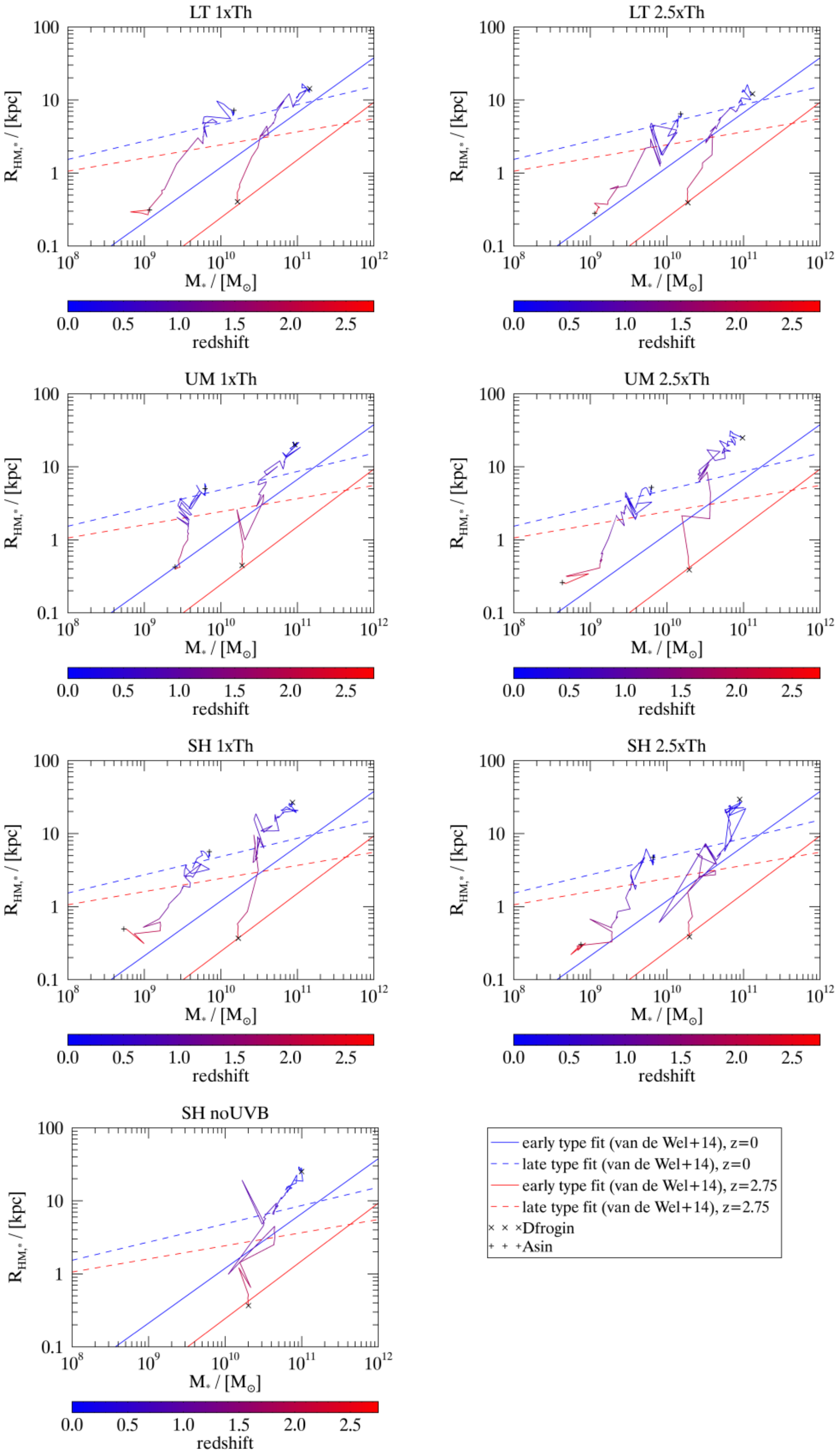

Figure 5.16: Evolution of the Dfrogin and Asin target galaxies in the M_*-$R_{\mathrm{HM},*}$ plane at 25x resolution for the different test runs. Also shown are fits to observations by van der Wel et al. 2014 for early type galaxies (solid lines) late types (dashed lines) for redshifts 0 (blue) and 2.75 (red). Note that no test run without UV background was performed for Asin. which is why it is missing in the last panel.

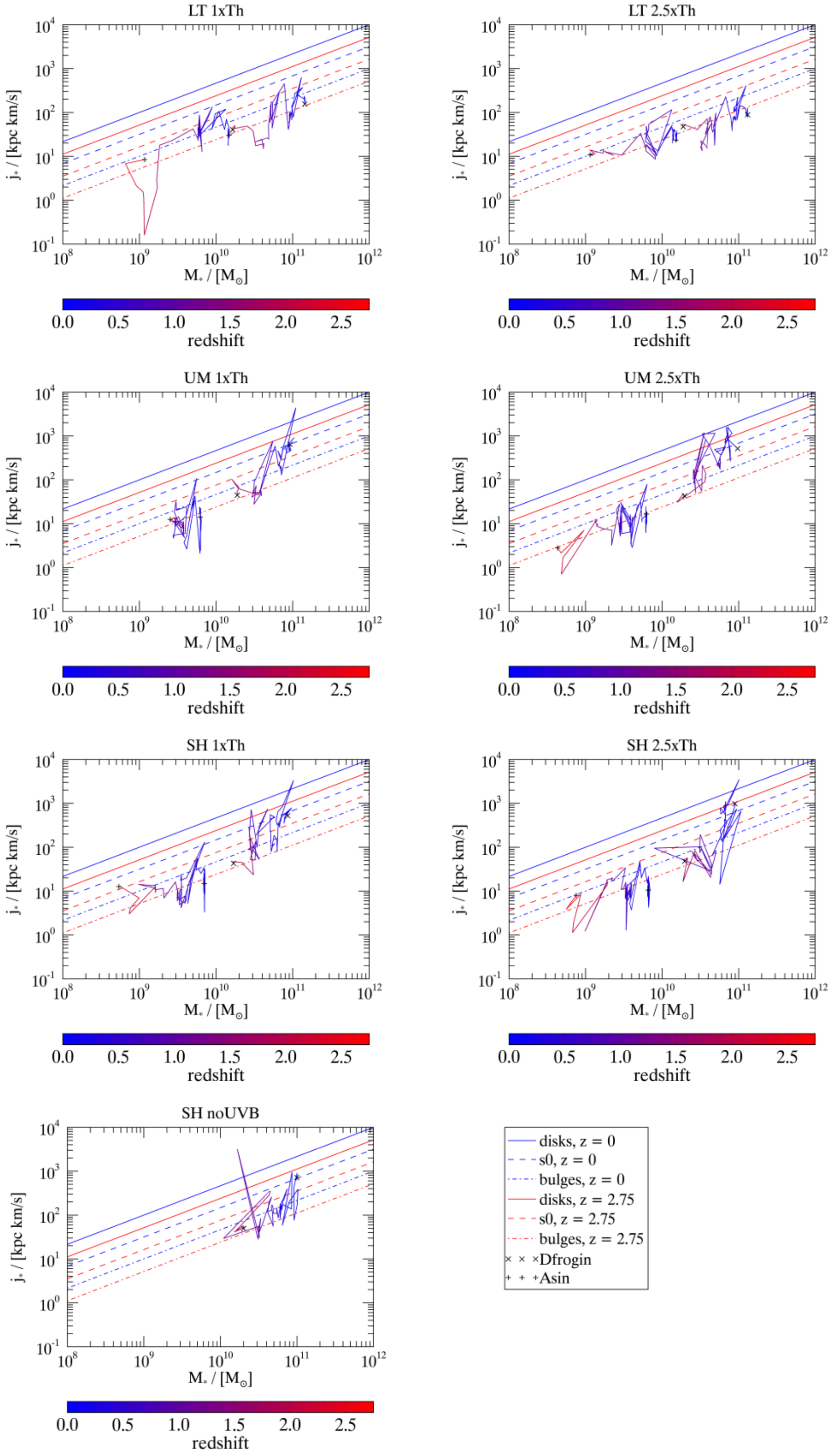

Figure 5.17: Evolution of the Dfrogin and Asin target galaxies in the M_*-j_* plane at 25x resolution for the different test runs. Also shown are scaling relations for disks, s0 type galaxies, and pure bulges from Teklu et al. 2015. Blue lines indicate where these relations lie at redshift 0, while red lines show them scaled to redshift 2 according to Obreschkow et al. 2015.

particularly with galaxies smaller than itself. These latter minor mergers have been found to have a strong effect on the growth of massive ellipticals at later times (Naab et al. 2009). Assuming Asin indeed undergoes fewer mergers, the effect of the overall galaxy population being more gas poor or 'dry' would have less of an effect on its growth.

Figure 5.17 shows the same two galaxies as they evolve in the plane of stellar mass and specific stellar angular momentum. Neither galaxy consistently reaches a specific angular momentum indicative of a disk at that redshift in any of the test runs, even though they clearly are in the disk range of the mass size relation at $z = 0$. Dfrogin generally seems to end its evolution with more specific stellar angular momentum in the chemical network runs compared to the base runs. However, most notable is how erratic the evolutionary tracks of both Asin and Dfrogin are in the M_*-j_* plane.

5.4 Resolution Study

Despite the challenges with the chemical network model implementation at lower redshifts, the zoom simulations may still provide valuable insight into the effect of resolution on the evolution of molecular gas. To this end, test runs of Dfrogin with chemical network and shielding implemented were performed at four different resolution levels. These levels are based on the parent simulation Dianoga and denoted 1x, 10x, 25x, and 250x after their respective increase in mass resolution compared to the base. The resulting dark matter particle masses can be found in Table 5.2. Also listed are the default density thresholds for star formation, which change along with the density level that the simulation can effectively resolve. For each resolution level, except the highest one (250x), two runs were performed, one with the default density threshold, and one with the threshold increased by a factor of about 2. This allows for a comparison the relative effects of resolution and the density threshold increase. Due to time constraints only one test run was performed at the highest resolution, and the implementation with increased star formation threshold was chosen. The single high resolution run crashed around redshift 2.5, due to the necessary timestep length falling short of the lower limit imposed by Gadget.

Resolution	**1x**	**10x**	**25x**	**250x**
m_{DM} $[M_\odot]$	$8.3 \cdot 10^8$	$8.3 \cdot 10^7$	$3.3 \cdot 10^7$	$3.3 \cdot 10^6$
m_{gas} $[M_\odot]$	$1.5 \cdot 10^8$	$1.5 \cdot 10^7$	$6.2 \cdot 10^6$	$6.2 \cdot 10^5$
Default SF Th. [cm^{-3}]	0.5	1.0	2.0	5.0

Table 5.2: Dark matter and gas particle masses and default star formation density threshold in the four resolution levels of the study.

Figure 5.18 shows the evolution of molecular hydrogen mass with redshift in the entire high resolution region for all runs in the resolution test suite. The high resolution region was chosen as the subject of this study over the target galaxy alone in order to minimize the effect of Dfrogin's particular evolution path. Since the 250x run only provides data up to a redshift of about 2.5, finding a clear analogue for the progenitor of the target galaxy at redshift 0 becomes difficult. Even picking the galaxy closest to the position of the progenitor found in lower resolution runs provides no guarantee, that this galaxy would have turned out to be the main progenitor of the target at low redshifts. With the choice of the entire target region this is of no concern, and any boost to H_2 production and shielding due to the increased resolution should still be visible in the data. While the resulting H_2 masses still show significant and rapid fluctuations at low redshift, their evolution is much smoother at earlier times for all but the lowest resolution runs. There, the total H_2 mass in the region drops to the model imposed floor as early as redshift 5. Comparing those runs with resolutions above the base shows the expected increase in H_2 mass with resolution. The 2.5 times increase between 10x and 25x

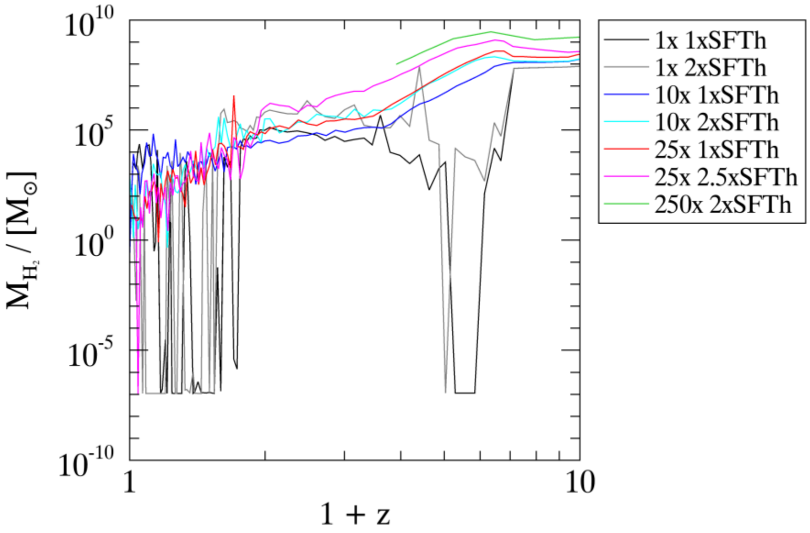

Figure 5.18: H_2 mass evolution with redshift in the target region containing Dfrogin across the seven different variations of resolution and star formation density threshold. Note that while the red and pink lines still correspond to the previous SHDef and SH5 runs respectively, all other colors now represent different simulations than in previous figures.

has an effect comparable in magnitude to an increase in star formation threshold density by a factor of 2. With a resolution increase by a factor of 10 between the 25x run (pink line) and 250x run (green line), the H_2 mass still increases significantly. Whether this increase suffices to bring H_2 levels up to what is found in observations cannot be discerned from this, however, because the 250x resolution run did not proceed far enough past the crucial redshift 3. Thus, it cannot be concluded that it would not exhibit the same erratic behavior at later times than the lower resolution runs. Likewise, it cannot be determined if the model converges with resolution. If it does, then this likely only occurs beyond the resolution level of the 250x run. There is, however, no guarantee that such resolutions would still be feasible for cosmological simulations. In combination with the fact that the resolutions tested here are already of interest for future studies, this further highlights the need for additions to the model if it is to be used in further cosmological simulations.

5.5 Impact of the UV Background Model

The UV background used in all the above simulations, save the test run with no UV background whatsoever, follows Haardt and Madau 2012 as discussed in Chapter 3. Models of the UV background are frequently updated with new constraints from observational data, and two recent models (Puchwein et al. 2019, Faucher-Giguère 2020) are tested as alternatives to the default used so far in this thesis. To this end, Dfrogin was re-simulated two additional times with all parameters matching the SH5 run, except for the UV background tables which were taken from the sources given above.

The top panel of Figure 5.19 shows the evolution of Dfrogin's H_2 mass in the different test runs. All runs with UV background produce the same fluctuations at low redshifts, that the previous sections of this chapter discussed in detail. Even between redshifts 8 and 6, where the earlier onset of the UV background in the two alternative models (see Figure 3.3) comes to bear, the evolution of Dfrogin's H_2 is not notably affected. Much the same result can be seen for the HI mass, as is shown in the bottom panel of Figure 5.19. Thus, it can be

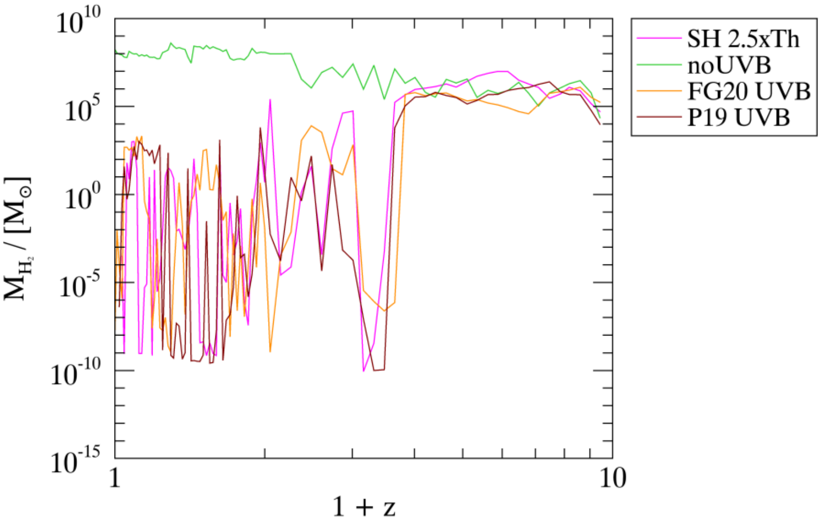

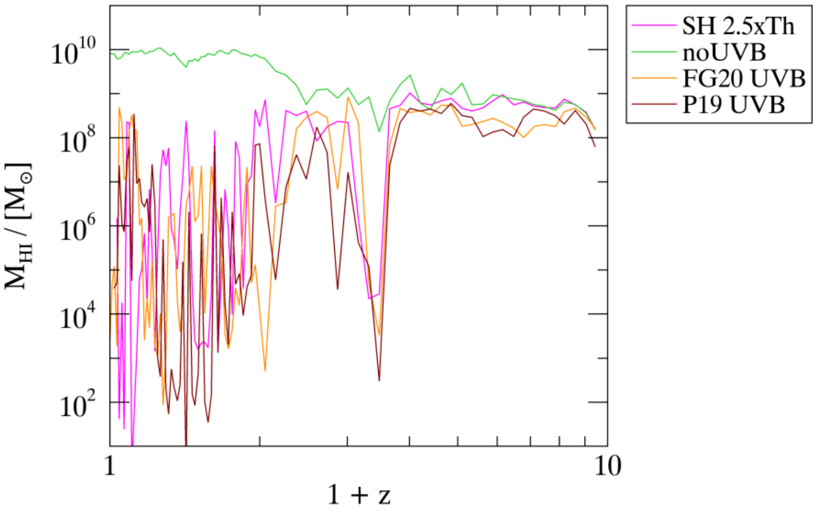

Figure 5.19: Dfrogin's H_2 (top) and HI (bottom) mass evolution with redshift for different implementations of the UV background. The dark red line shows the shielding run with the Puchwein et al. 2019 UV background model and the orange line indicates the run using the Faucher-Giguère 2020 model. In addition to the two new models, the SH5 run (with the Haardt and Madau 2012 model) and the test run without any UV background are shown.

concluded that the chemical network model does not strongly depend on the choice of UV background within the constraints given by observations.

These additional data sets also confirm that the rapid decline in Dfrogin's gas mass must indeed be due to local feedback. If it were caused by heating and ionization from the UV background, then its timing should differ between the three UV background models which have varying onset times.

Chapter 6

Discussion & Conclusion

At the core of this thesis stands a chemical network based low temperature cooling module for the OpenGadget3 code. The module was developed by Maio et al. 2007, and shown to work successfully at high redshifts and for early structure formation. The goal of this work is to gauge the effectiveness of the chemical network for modeling the evolution of galaxies to lower redshifts, and at resolutions feasible for such simulations. Different implementations of the chemical network were tested for both a full cosmological box and zoom-ins over a range of particle resolutions between $m_{\rm dm} = 6.90 \cdot 10^8\ M_\odot$ and $m_{\rm DM} = 3.3 \cdot 10^7\ M_\odot$, in order to determine the impact of a new addition to the module that attempts to capture the impact of HI and H_2 self-shielding from the UV background. The results from both suits of simulations show that the current shielding implementation is not suitable for the tested resolutions.

In the full cosmological simulation at a mass resolution of $m_{\rm dm} = 6.90 \cdot 10^8\ M_\odot$, all model variations predict abundances of neutral atomic hydrogen and molecular hydrogen that fall short of observations. Increasing the star formation density threshold parameter, in order for the simulated gas to reach higher densities and self-shielding to become more effective, proved to have a significant effect on both HI and H_2 abundance. However, at the highest tested values of this parameter, simulations still produce about an order of magnitude less HI and several orders of magnitude less H_2 than observed at redshifts of 6 and below. Meanwhile, galaxies formed in this run are found to be too compact and no longer follow the observed mass-size relation. The process of adapting the model to lower resolutions can thus not solely rely on increasing the star formation density threshold.

Further testing was performed on cosmological zoom-in simulations, in order to extend the study to mass resolutions up to $m_{\rm DM} = 3.3 \cdot 10^7\ M_\odot$. In addition, this allowed access to lower redshifts, and to follow the evolution of cold gas in galaxies in more detail. It was found that the low temperature cooling calculated based on the chemical network output altered the galaxy evolution in the zoom-in simulations drastically. Galactic gas densities after $z \sim 3$ are too low for effective shielding in the model, and the target galaxies consist almost entirely of hot ionized gas at low redshifts. This effect was found to not depend strongly on the chosen implementation of the UV background. An increased resolution might be able to address the problem partially, as smaller regions of high density are resolved instead of averaged over, resulting in higher peak densities. While it seems feasible that more effective shielding could bring HI levels up to what is observed, it is likely that to achieve the same for H_2 would require additional formation channels for molecules to be considered in the chemical network. A prime candidate would be catalyzed reactions on the surface of dust grains, which play an increasing role towards lower redshifts with more dust present in the gas than at the dawn of the Universe.

However, the final state of the zoom-in galaxies in the chemical network runs is likely not only, or even primarily, a consequence of the ineffective self-shielding or UV background radiation. A strong feedback event, that causes a lasting disruption to the galactic gas component, is present at redshifts between 3 and 2 in all chemical network zoom-in runs. This is likely either due to excessive star formation at that redshift, or due to feedback from the central black hole accreting large amounts of gas. The Dfrogin target galaxy showed some signs pointing towards the former, with significantly more star forming gas at $z = 3$ in the chemical network runs compared to the base line runs. Testing the impact of black hole accretion and feedback would require additions to the suite of simulations that are beyond the scope of this thesis, so that the possibility cannot be ruled out at this point. In either case, resolution is unlikely to markedly change the occurrence of the disrupting feedback. Instead, changes to the coupling between star formation and feedback on the one hand and the chemical network on the other hand are probably necessary. As it stands, the chemical network model works as an extension of the base line stellar evolution, feedback, and cooling model by replacing only its low temperature cooling aspects. Star formation does not directly depend on the chemical network output, and stellar feedback likewise is only indirectly coupled via gas temperature. Thus, the cooling provided by the chemical network may lead to excessive star formation, without the resulting feedback being able to ‘push back’ in a consistent manner. The same is true for black hole accretion and feedback. A self-consistent implementation of the model would have to include modes of feedback directly as factors in the evolution of species in the network. Then, the cooling function calculated from the network should accurately reflect the impact of the feedback, and prevent inconsistent levels of cooling that continue to feed gas into the sources of feedback.

That being said, the other major benefit of implementing a chemical network in cosmological simulations besides cooling, is still apparent in this work. Comparing the abundance of HI and H_2 on cosmological scales and in individual galaxies to observations, in order to determine if the simulations correctly capture physical processes, was only possible because of the chemical network. Without the chemical abundances tied directly into the evolution of simulated gas, this additional constraint for cosmological simulations cannot be utilized to the same degree. Future work should thus aim to extend the study presented here to higher resolutions, and to adapt the chemical network model for the resolutions covered in this thesis. The latter will likely require some form of dust treatment to be added to the model, and the implementation of stellar and black hole feedback in a more self-consistent manner.

References

Anninos, Peter, Yu Zhang, Tom Abel, and Michael L. Norman (Aug. 1997). “Cosmological hydrodynamics with multi-species chemistry and nonequilibrium ionization and cooling”. In: *New Astronomy* 2.3, pp. 209–224. ISSN: 1384-1076. DOI: `10.1016/s1384-1076(97)00009-2`.

Bešlić, I, A T Barnes, F Bigiel, J Puschnig, J Pety, C Herrera Contreras, A K Leroy, A Usero, E Schinnerer, S E Meidt, E Emsellem, A Hughes, C Faesi, K Kreckel, F M C Belfiore, M Chevance, J S den Brok, C Eibensteiner, S C O Glover, K Grasha, M J Jimenez-Donaire, R S Klessen, J M D Kruijssen, D Liu, I Pessa, M Querejeta, E Rosolowsky, T Saito, F Santoro, A Schruba, M C Sormani, and T G Williams (June 2021). “Dense molecular gas properties on 100 pc scales across the disc of NGC 3627”. In: *Monthly Notices of the Royal Astronomical Society* 506.1, pp. 963–988. ISSN: 0035-8711. DOI: `10.1093/mnras/stab1776`.

Bittner, Adrian (2018). “Spiral Galaxies in Cosmological Zoom-Simulations”. MA thesis. Ludwig-Maximilians-Universität München.

Black, John H. (Dec. 1981). “The physical state of primordial intergalactic clouds”. In: *Monthly Notices of the Royal Astronomical Society* 197.3, pp. 553–563. ISSN: 0035-8711. DOI: `10.1093/mnras/197.3.553`.

Bolmer, J., C. Ledoux, P. Wiseman, A. De Cia, J. Selsing, P. Schady, J. Greiner, S. Savaglio, J. M. Burgess, and V. D’Elia (Mar. 2019). “Evidence for diffuse molecular gas and dust in the hearts of gamma-ray burst host galaxies”. In: *Astronomy & Astrophysics* 623, A43. ISSN: 1432-0746. DOI: `10.1051/0004-6361/201834422`.

Catinella, Barbara, David Schiminovich, Guinevere Kauffmann, Silvia Fabello, Jing Wang, Cameron Hummels, Jenna Lemonias, Sean M. Moran, Ronin Wu, and Riccardo Giovanelli (Feb. 2010). “The GALEX Arecibo SDSS Survey - I. Gas fraction scaling relations of massive galaxies and first data release”. In: *Monthly Notices of the Royal Astronomical Society* 403.2, pp. 683–708. ISSN: 0035-8711. DOI: `10.1111/j.1365-2966.2009.16180.x`.

Chabrier, Gilles (July 2003). “Galactic Stellar and Substellar Initial Mass Function”. In: *Publications of the Astronomical Society of the Pacific* 115.809, pp. 763–795. DOI: `10.1086/376392`.

Cooke, J. and J. M. O’Meara (Oct. 2015). “A NEW CONSTRAINT ON THE PHYSICAL NATURE OF DAMPED LYMAN ALPHA SYSTEMS”. In: *The Astrophysical Journal* 812.2, p. L27. DOI: `10.1088/2041-8205/812/2/l27`.

Crain, Robert A., Joop Schaye, Richard G. Bower, Michelle Furlong, Matthieu Schaller, Tom Theuns, Claudio Dalla Vecchia, Carlos S. Frenk, Ian G. McCarthy, John C. Helly, Adrian Jenkins, Yetli M. Rosas-Guevara, Simon D. M. White, and James W. Trayford (Apr. 2015). “The EAGLE simulations of galaxy formation: calibration of subgrid physics and model variations”. In: *Monthly Notices of the Royal Astronomical Society* 450.2, pp. 1937–1961. ISSN: 0035-8711. DOI: `10.1093/mnras/stv725`.

Decarli, Roberto, Fabian Walter, Jorge Gónzalez-López, Manuel Aravena, Leindert Boogaard, Chris Carilli, Pierre Cox, Emanuele Daddi, Gergö Popping, Dominik Riechers, Bade Uzgil, Axel Weiss, Roberto J. Assef, Roland Bacon, Franz Erik Bauer, Frank Bertoldi, Rychard Bouwens, Thierry Contini, Paulo C. Cortes, Elisabete da Cunha, Tanio Díaz-Santos, David Elbaz, Hanae Inami, Jacqueline Hodge, Rob Ivison, Olivier Le Fèvre, Benjamin Magnelli, Mladen Novak, Pascal Oesch, Hans-Walter Rix, Mark T. Sargent, Ian Smail, A. Mark Swinbank, Rachel S. Somerville, Paul van der Werf, Jeff Wagg, and Lutz Wisotzki (Sept. 2019). "The ALMA Spectroscopic Survey in the HUDF: CO Luminosity Functions and the Molecular Gas Content of Galaxies through Cosmic History". In: *The Astrophysical Journal* 882.2, p. 138. DOI: `10.3847/1538-4357/ab30fe`.

Diemer, Benedikt, Adam R H Stevens, Claudia del P Lagos, A R Calette, Sandro Tacchella, Lars Hernquist, Federico Marinacci, Dylan Nelson, Annalisa Pillepich, Vicente Rodriguez-Gomez, Francisco Villaescusa-Navarro, and Mark Vogelsberger (May 2019). "Atomic and molecular gas in IllustrisTNG galaxies at low redshift". In: *Monthly Notices of the Royal Astronomical Society* 487.2, pp. 1529–1550. ISSN: 0035-8711. DOI: `10.1093/mnras/stz1323`.

Dolag, K., S. Borgani, G. Murante, and V. Springel (Oct. 2009). "Substructures in hydrodynamical cluster simulations". In: *Monthly Notices of the Royal Astronomical Society* 399.2, pp. 497–514. ISSN: 1365-2966. DOI: `10.1111/j.1365-2966.2009.15034.x`.

Dolag, Klaus, Emilio Mevius, and Rhea-Silvia Remus (Aug. 2017). "Distribution and Evolution of Metals in the Magneticum Simulations". In: *Galaxies* 5.3. ISSN: 2075-4434. DOI: `10.3390/galaxies5030035`.

Draine, B. T. and Frank Bertoldi (Sept. 1996). "Structure of Stationary Photodissociation Fronts". In: *The Astrophysical Journal* 468, p. 269. ISSN: 1538-4357. DOI: `10.1086/177689`.

Faucher-Giguère, Claude-André (Jan. 2020). "A cosmic UV/X-ray background model update". In: *Monthly Notices of the Royal Astronomical Society* 493.2, pp. 1614–1632. ISSN: 0035-8711. DOI: `10.1093/mnras/staa302`.

Franx, Marijn, Pieter G. van Dokkum, Natascha M. Förster Schreiber, Stijn Wuyts, Ivo Labbé, and Sune Toft (Dec. 2008). "Structure and Star Formation in Galaxies out toz= 3: Evidence for Surface Density Dependent Evolution and Upsizing". In: *The Astrophysical Journal* 688.2, pp. 770–788. DOI: `10.1086/592431`.

Galli, Daniele and Francesco Palla (July 1998). "The Chemistry of the Early Universe". In: *Astronomy and Astrophysics* 335, pp. 403–420.

Garratt, T. K., K. E. K. Coppin, J. E. Geach, O. Almaini, W. G. Hartley, D. T. Maltby, C. J. Simpson, A. Wilkinson, C. J. Conselice, M. Franco, R. J. Ivison, M. P. Koprowski, C. C. Lovell, A. Pope, D. Scott, and P. van der Werf (May 2021). "Cosmic Evolution of the H2 Mass Density and the Epoch of Molecular Gas". In: *The Astrophysical Journal* 912.1, p. 62. DOI: `10.3847/1538-4357/abec81`.

Haardt, Francesco and Piero Madau (Feb. 2012). "Radiative transfer in a clumpy universe. IV. New synthesis models of the cosmic UV/X-Ray background". In: *The Astrophysical Journal* 746.2, p. 125. DOI: `10.1088/0004-637x/746/2/125`.

Hilz, Michael, Thorsten Naab, Jeremiah P. Ostriker, Jens Thomas, Andreas Burkert, and Roland Jesseit (Oct. 2012). "Relaxation and stripping – The evolution of sizes, dispersions and dark matter fractions in major and minor mergers of elliptical galaxies". In: *Monthly Notices of the Royal Astronomical Society* 425.4, pp. 3119–3136. ISSN: 0035-8711. DOI: `10.1111/j.1365-2966.2012.21541.x`.

Hirschmann, Michaela, Klaus Dolag, Alexandro Saro, Lisa Bachmann, Stefano Borgani, and Andreas Burkert (June 2014). "Cosmological simulations of black hole growth: AGN luminosities and downsizing". In: *Monthly Notices of the Royal Astronomical Society* 442.3, pp. 2304–2324. ISSN: 0035-8711. DOI: `10.1093/mnras/stu1023`.

Hui, Lam and Nickolay Y. Gnedin (Nov. 1997). "Equation of state of the photoionized intergalactic medium". In: *Monthly Notices of the Royal Astronomical Society* 292.1, pp. 27–42. ISSN: 0035-8711. DOI: `10.1093/mnras/292.1.27`.

Karademir, Geray S, Rhea-Silvia Remus, Andreas Burkert, Klaus Dolag, Tadziu L Hoffmann, Benjamin P Moster, Ulrich P Steinwandel, and Jielai Zhang (May 2019). "The outer stellar halos of galaxies: how radial merger mass deposition, shells, and streams depend on infall-orbit configurations". In: *Monthly Notices of the Royal Astronomical Society* 487.1, pp. 318–332. ISSN: 0035-8711. DOI: `10.1093/mnras/stz1251`.

Karakas, Amanda and John C. Lattanzio (2007). "Stellar Models and Yields of Asymptotic Giant Branch Stars". In: *Publications of the Astronomical Society of Australia* 24.3, pp. 103–117. DOI: `10.1071/AS07021`.

Katz, Neal, David H. Weinberg, and Lars Hernquist (July 1996). "Cosmological Simulations with TreeSPH". In: *The Astrophysical Journal Supplement Series* 105, pp. 19–35.

Lipovka, Anton, Ramona Núñez-López, and Vladimir Avila-Reese (Aug. 2005). "The cooling function of HD molecule revisited". In: *Monthly Notices of the Royal Astronomical Society* 361.3, pp. 850–854. ISSN: 0035-8711. DOI: `10.1111/j.1365-2966.2005.09226.x`.

Madau, Piero and Mark Dickinson (2014). "Cosmic Star-Formation History". In: *Annual Review of Astronomy and Astrophysics* 52.1, pp. 415–486. DOI: `10.1146/annurev-astro-081811-125615`.

Maio, U., K. Dolag, B. Ciardi, and L. Tornatore (Aug. 2007). "Metal and molecule cooling in simulations of structure formation". In: *Monthly Notices of the Royal Astronomical Society* 379.3, pp. 963–973. ISSN: 1365-2966. DOI: `10.1111/j.1365-2966.2007.12016.x`.

Maio, Umberto (2021). In: in preparation.

Moster, Benjamin P., Thorsten Naab, and Simon D. M. White (Dec. 2012). "Galactic star formation and accretion histories from matching galaxies to dark matter haloes ". In: *Monthly Notices of the Royal Astronomical Society* 428.4, pp. 3121–3138. ISSN: 0035-8711. DOI: `10.1093/mnras/sts261`.

Naab, Thorsten, Peter H. Johansson, and Jeremiah P. Ostriker (June 2009). "MINOR MERGERS AND THE SIZE EVOLUTION OF ELLIPTICAL GALAXIES". In: *The Astrophysical Journal* 699.2, pp. L178–L182. DOI: `10.1088/0004-637x/699/2/l178`.

Nelson, Dylan, Volker Springel, Annalisa Pillepich, Vicente Rodriguez-Gomez, Paul Torrey, Shy Genel, Mark Vogelsberger, Ruediger Pakmor, Federico Marinacci, Rainer Weinberger, Luke Kelley, Mark Lovell, Benedikt Diemer, and Lars Hernquist (May 2019). "The IllustrisTNG simulations: public data release". In: *Computational Astrophysics and Cosmology* 6.1, p. 2. ISSN: 2197-7909. DOI: `10.1186/s40668-019-0028-x`.

Nomoto, Ken'ichi, Chiaki Kobayashi, and Nozomu Tominaga (2013). "Nucleosynthesis in Stars and the Chemical Enrichment of Galaxies". In: *Annual Review of Astronomy and Astrophysics* 51.1, pp. 457–509. DOI: `10.1146/annurev-astro-082812-140956`.

Obreschkow, Danail, Karl Glazebrook, Robert Bassett, David B. Fisher, Roberto G. Abraham, Emily Wisnioski, Andrew W. Green, Peter J. McGregor, Ivana Damjanov, Attila Popping, and Inger Jørgensen (Dec. 2015). "Low angular momentum in clumpy, turbulent disk galaxies". In: *The Astrophysical Journal* 815.2, p. 97. DOI: `10.1088/0004-637x/815/2/97`.

Pearson, W. J., Wang, L., Hurley, P. D., Malek, K., Buat, V., Burgarella, D., Farrah, D., Oliver, S. J., Smith, D. J. B., and van der Tak, F. F. S. (2018). "Main sequence of star forming galaxies beyond the Herschelnfusion limit". In: *A&A* 615, A146. DOI: `10.1051/0004-6361/201832821`.

Péroux, Céline and J. Christopher Howk (Aug. 2020). "The Cosmic Baryon and Metal Cycles". In: *Annual Review of Astronomy and Astrophysics* 58.1, pp. 363–406. DOI: `10.1146/annurev-astro-021820-120014`.

Prochaska, J Xavier and Yong Zheng (Jan. 2019). "Probing Galactic haloes with fast radio bursts". In: *Monthly Notices of the Royal Astronomical Society* 485.1, pp. 648–665. ISSN: 0035-8711. DOI: `10.1093/mnras/stz261`.

Puchwein, Ewald, Francesco Haardt, Martin G Haehnelt, and Piero Madau (Jan. 2019). "Consistent modelling of the meta-galactic UV background and the thermal/ionization history of the intergalactic medium". In: *Monthly Notices of the Royal Astronomical Society* 485.1, pp. 47–68. ISSN: 0035-8711. DOI: `10.1093/mnras/stz222`.

Rahmati, Alireza, Andreas H. Pawlik, Milan Raicevic, and Joop Schaye (Feb. 2013). "On the evolution of the HI column density distribution in cosmological simulations". In: *Monthly Notices of the Royal Astronomical Society* 430.3, pp. 2427–2445. ISSN: 0035-8711. DOI: `10.1093/mnras/stt066`.

Rahmati, Alireza, Joop Schaye, Richard G. Bower, Robert A. Crain, Michelle Furlong, Matthieu Schaller, and Tom Theuns (July 2015). "The distribution of neutral hydrogen around high-redshift galaxies and quasars in the EAGLE simulation". In: *Monthly Notices of the Royal Astronomical Society* 452.2, pp. 2034–2056. ISSN: 0035-8711. DOI: `10.1093/mnras/stv1414`.

Rhee, Jonghwan, Philip Lah, Frank H. Briggs, Jayaram N. Chengalur, Matthew Colless, Steven P. Willner, Matthew L. N. Ashby, and Olivier Le Fèvre (Sept. 2017). "Neutral hydrogen (HI) gas content of galaxies at $z \approx 0.32$". In: *Monthly Notices of the Royal Astronomical Society* 473.2, pp. 1879–1894. ISSN: 0035-8711. DOI: `10.1093/mnras/stx2461`.

Riechers, Dominik A., Riccardo Pavesi, Chelsea E. Sharon, Jacqueline A. Hodge, Roberto Decarli, Fabian Walter, Christopher L. Carilli, Manuel Aravena, Elisabete da Cunha, Emanuele Daddi, Mark Dickinson, Ian Smail, Peter L. Capak, Rob J. Ivison, Mark Sargent, Nicholas Z. Scoville, and Jeff Wagg (Feb. 2019). "COLDz: Shape of the CO Luminosity Function at High Redshift and the Cold Gas History of the Universe". In: *The Astrophysical Journal* 872.1, p. 7. DOI: `10.3847/1538-4357/aafc27`.

Saintonge, Amélie, Guinevere Kauffmann, Carsten Kramer, Linda J. Tacconi, Christof Buchbender, Barbara Catinella, Silvia Fabello, Javier Graciá-Carpio, Jing Wang, and Luca Cortese (June 2011). "COLD GASS, an IRAM legacy survey of molecular gas in massive galaxies - I. Relations between H2, HI, stellar content and structural properties". In: *Monthly Notices of the Royal Astronomical Society* 415.1, pp. 32–60. ISSN: 0035-8711. DOI: `10.1111/j.1365-2966.2011.18677.x`.

Santoro, Fernando and J. Michael Shull (May 2006). "Critical Metallicity and Fine-Structure Emission of Primordial Gas Enriched by the First Stars". In: *The Astrophysical Journal* 643.1, pp. 26–37. DOI: `10.1086/501518`.

Schaye, Joop, Robert A. Crain, Richard G. Bower, Michelle Furlong, Matthieu Schaller, Tom Theuns, Claudio Dalla Vecchia, Carlos S. Frenk, I. G. McCarthy, John C. Helly, Adrian Jenkins, Y. M. Rosas-Guevara, Simon D. M. White, Maarten Baes, C. M. Booth, Peter Camps, Julio F. Navarro, Yan Qu, Alireza Rahmati, Till Sawala, Peter A. Thomas, and James Trayford (Nov. 2014). "The EAGLE project: simulating the evolution and assembly of galaxies and their environments". In: *Monthly Notices of the Royal Astronomical Society* 446.1, pp. 521–554. ISSN: 0035-8711. DOI: `10.1093/mnras/stu2058`.

Schlachtenberger, David P. (2014). "The origin of cold gas in the center of massive elliptical galaxies". MA thesis. Ludwig-Maximilians-Universität München.

Springel, Volker (Dec. 2005). "The cosmological simulation code gadget-2". In: *Monthly Notices of the Royal Astronomical Society* 364.4, pp. 1105–1134. ISSN: 0035-8711. DOI: `10.1111/j.1365-2966.2005.09655.x`.

Springel, Volker, Naoki Yoshida, and Simon D.M. White (Apr. 2001). "GADGET: a code for collisionless and gasdynamical cosmological simulations". In: *New Astronomy* 6.2, pp. 79–117. ISSN: 1384-1076. DOI: `https://doi.org/10.1016/S1384-1076(01)00042-2`.

Tacconi, Linda J., Reinhard Genzel, and Amiel Sternberg (2020). "The Evolution of the Star-Forming Interstellar Medium Across Cosmic Time". In: *Annual Review of Astronomy and Astrophysics* 58.1, pp. 157–203. DOI: `10.1146/annurev-astro-082812-141034`.

Teklu, Adelheid F., Rhea-Silvia Remus, Klaus Dolag, Alexander M. Beck, Andreas Burkert, Andreas S. Schmidt, Felix Schulze, and Lisa K. Steinborn (Oct. 2015). "Connecting angular momentum and galactic dynamics: the complex interplay between spin, mass and morphology". In: *The Astrophysical Journal* 812.1, p. 29. DOI: `10.1088/0004-637x/812/1/29`.

Thielemann, F.-K., D. Argast, F. Brachwitz, W. R. Hix, P. Höflich, M. Liebendörfer, G. Martinez-Pinedo, A. Mezzacappa, K. Nomoto, and I. Panov (2003). "Supernova Nucleosynthesis and Galactic Evolution". In: *From Twilight to Highlight: The Physics of Supernovae*. Ed. by Wolfgang Hillebrandt and Bruno Leibundgut. Berlin, Heidelberg: Springer Berlin Heidelberg, pp. 331–343. ISBN: 978-3-540-36427-6.

Tomczak, Adam R., Ryan F. Quadri, Kim-Vy H. Tran, Ivo Labbé, Caroline M. S. Straatman, Casey Papovich, Karl Glazebrook, Rebecca Allen, Gabriel B. Brammer, Glenn G. Kacprzak, Lalitwadee Kawinwanichakij, Daniel D. Kelson, Patrick J. McCarthy, Nicola Mehrtens, Andrew J. Monson, S. Eric Persson, Lee R. Spitler, Vithal Tilvi, and Pieter van Dokkum (Feb. 2014). "Galaxy Stellar Mass Functions from ZFOURGE/CANDELS: an Excess of Low-Mass Galaxies since z = 2 and the Rapid Buildup of Quiescent Galaxies". In: *The Astrophysical Journal* 783.2, p. 85. DOI: `10.1088/0004-637x/783/2/85`.

Tormen, Giuseppe, François R. Bouchet, and Simon D. M. White (Apr. 1997). "The structure and dynamical evolution of dark matter haloes". In: *Monthly Notices of the Royal Astronomical Society* 286.4, pp. 865–884. DOI: `10.1093/mnras/286.4.865`.

van der Wel, A., M. Franx, P. G. van Dokkum, R. E. Skelton, I. G. Momcheva, K. E. Whitaker, G. B. Brammer, E. F. Bell, H.-W. Rix, S. Wuyts, H. C. Ferguson, B. P. Holden, G. Barro, A. M. Koekemoer, Yu-Yen Chang, E. J. McGrath, B. Häussler, A. Dekel, P. Behroozi, M. Fumagalli, J. Leja, B. F. Lundgren, M. V. Maseda, E. J. Nelson, D. A. Wake, S. G. Patel, I. Labbé, S. M. Faber, N. A. Grogin, and D. D. Kocevski (May 2014). "3D-HST+CANDELS: The evolution of the galaxy size-mass distribution since $z = 3$". In: *The Astrophysical Journal* 788.1, p. 28. DOI: `10.1088/0004-637x/788/1/28`.

List of Figures

1.1 Overview of scaling relations of galactic molecular gas and stellar mass from Tacconi et al. 2020 (their Figure 5). Top left: Scaling relation of the molecular gas to stellar mass fraction M_{molgas}/M_* with the offset in specific star formation rate from the star forming main sequence of galaxies. Top right: M_{molgas}/M_* scaling relation with stellar mass. Bottom left: M_{molgas}/M_* scaling relation with redshift. Bottom right: Scaling relation of the molecular to total mass $M_{\mathrm{molgas}}/(M_{\mathrm{molgas}} + M_*)$ with redshift. The black lines denote the binned averages of the distributions. 2

1.2 Cosmic density evolution of neutral atomic and molecular hydrogen, as well as stars in our Universe from Péroux and Howk 2020 (their Figure 4). 5

2.1 A 500 kpc slice through the center of Magneticum Box 4. Dark matter particles are depicted in purple, gas in orange and stars in cyan. 10

2.2 Visualization of the Zoom-in target object Dfrogin at low redshift. Shown is a volume of $(R_{\mathrm{vir}})^3$ centered on the galaxy. Dark matter particles are depicted in purple, gas in orange and stars in cyan. 13

3.1 Cooling contributions of HD, H_2, and H_2^+ as implemented in the chemical model shown for a range of temperatures at a fixed hydrogen number density of 1 cm^{-3}. Taken with kind permission from Maio et al. 2007 (their Figure 2). Note that the H_2^+ contribution is split into the contributions from collisions with neutral atomic hydrogen and electrons respectively with both fits only valid for $T < 10^4$ K. 17

3.2 Total cooling from the chemical network as a function of temperature for a hydrogen density of 1 cm^{-3}, a H_2 fraction of 10^{-5}, and a HD fraction of 10^{-8}. The different curves represent metal abundances of 10^{-3}, 10^{-4}, 10^{-5}, and 10^{-6} respectively as labeled in the plot. This figure was taken from Maio et al. 2007 (their Figure 4). 19

3.3 Comparison of photoionization (top) and -heating (bottom) rates for HI, HeI and HeII in the three different UV background models. Haardt and Madau 2012 in black, Puchwein et al. 2019 in blue, and Faucher-Giguère 2020 in red. 20

3.4 Visualization of the HI self-shielding implementation into the chemical network model. The intensity of the UV background is attenuated by a density dependant factor. Total hydrogen number densities as used in the model computations are shown on the lower x-axis while approximate corresponding physical densities are shown above. 21

4.1 Redshift evolution of comoving cosmic densities for the four different runs of Box 4. LT is the reference run without the chemical network, UM denotes the base chemical network model with coupling to the UVB, UM_shield includes HI and H_2 self-shielding on top of the base model, and UM_shield2 includes a higher density threshold for star formation. 24

4.2 Redshift evolution of comoving cosmic densities in the different simulations compared with data. Stellar mass densities are from a range of observations compiled by Madau and Dickinson 2014. HI densities are selected from Rhee et al. 2017 and references therein. The boxes represent 2σ confidence intervals from for the given redshift ranges from ASPECS (Decarli et al. 2019) and COLDz (Riechers et al. 2019). Note the different density range compared to Figure 4.1. 26

4.3 Redshift evolution of comoving cosmic HI density the different runs compared to data and other cosmological simulations. The range given by Rahmati et al. 2015 is obtained from post-processing of the EAGLE simulation, while Diemer et al. 2019 use Illustris TNG100. 27

4.4 Stellar mass function (SMF) of galaxies in Box 4 with $M_* > 10^{11}\ M_\odot$. The green line is a double Schechter fit to ZFOURGE/CANDELS data from Tomczak et al. 2014. The green shaded area covers the data range and scatter. . . 28

4.5 Comparison of the stellar mass - star formation rate distribution of galaxies in the different test runs and the observed star forming main sequence of galaxies at this redshift (Pearson et al. 2018). Galaxies with no ongoing star formation at this redshift are represented by the vertical dashes at the bottom of the plot. 29

4.6 The stellar mass - stellar angular momentum distribution of galaxies in the different test runs of Box 4. The lines separating different galaxy morphologies are adapted from (Teklu et al. 2015) and scaled to $z = 2$ according to theoretical predictions by Obreschkow et al. 2015. 30

4.7 Comparison of the halo mass - stellar mass distribution of galaxies in the different test runs. Also shown is an empirical model prediction by Moster et al. 2012. Only main halos are shown in this comparison because overdensity based radii like R200 cannot be determined for sub halos and consequently neither can the corresponding masses. 30

4.8 Comparison of the stellar mass - stellar half-mass radius distribution of galaxies in the different test runs of Box 4 with observations at this redshift (van der Wel et al. 2014). 31

5.1 Comparison of Dfrogin's molecular hydrogen mass evolution with redshift in the five different runs with the chemical network at 25x resolution. 34

5.2 Comparison of Dfrogin's track in the M_*-M_{H_2} diagram with observations from the COLD GASS survey (Saintonge et al. 2011). The part of the track for each model that lies within the redshift range of the data (0-0.5) is represented by a solid line, while dashed lines show the evolution at higher redshifts and are thus not directly comparable to the data. 35

5.3 Maximum molecular hydrogen fraction in gas particles bound to Dfrogin by redshift. Note that the model imposes a floor of 10^{-20} on species abundances. 36

5.4 Comparison of Dfrogin's track in the M_*-M_{HI} diagram with observations from the xGASS survey (Catinella et al. 2010). The part of the track for each model that lies within the redshift range of the data (0-0.5) is represented by a solid line, while dashed lines show the evolution at higher redshifts and are thus not directly comparable to the data. 36

5.5 Comparison of Dfrogin's neutral atomic hydrogen mass evolution with redshift between all seven runs at 25x resolution. 37

5.6 Redshift evolution of the abundances in Dfrogin of all chemical network species for the SH5 run. 37

5.7 Radial gas density profiles of Dfrogin at selected redshifts on a double log-scale. Each bin contains 200 gas particles. The color scheme for the seven different runs is the same as in Figure 5.2 with the addition of black and gray lines for the LTDef and LT5 base runs respectively. The vertical black line denotes the physical softening for gas particles at that redshift. 39
5.8 Comparison of the total bound gas mass evolution with redshift in the seven different runs of Dfrogin at 25x resolution. 40
5.9 Physical density of cold gas (top) and abundance ratio of molecular to atomic hydrogen (bottom) for the SH5 run of Dfrogin. Particles colored according to the scale have $T > 10^4$K while gray particles correspond to hot gas. Positions are scaled to the Virial radius, indicated by the black circle, at each redshift. 40
5.10 Physical density of cold gas in all test runs of Dfrogin from $z = 3$ to $z = 0.13$. Particles colored according to the scale have $T > 10^4$K while gray particles correspond to hot gas. Positions are scaled to the Virial radius, indicated by the black circle, at each redshift. 41
5.11 Spatial distribution of hot gas particles that are identified in the LTDef run as part of the target halo Dfrogin, shown for both the LTDef and UMDef simulations. Black circles indicate the virial radius of the respective galaxy. Note that the large virial radius for the LTDef run in the middle panel is likely due to an ongoing merger at this redshift. The range of both plots is identical and covers a $(50R_{\mathrm{vir,UMDef}})^2$ square in code units. 42
5.12 Phase diagram of gas in all test runs of Dfrogin from $z = 3$ to $z = 0.13$. From top to bottom the models shown are: LTDef, LT5, UMDef, UM5, SHDef, SH5, and SHnoUVB all in the familiar color scheme. The vertical black line denotes the density threshold for star formation in each model assuming the average molecular mass to be 1.22. 43
5.13 Comparison of Dfrogin's star formation rate evolution with redshift between all seven runs at 25x resolution. Any data points below the lower limit of the plot correspond to zero star formation in the entire galaxy at that redshift. . 45
5.14 Comparison of Dfrogin's track in the M_*-SFR diagram with xGASS and xCOLDGASS data (Catinella et al. 2010, Saintonge et al. 2011). The part of the track for each model that lies within the redshift range of the data (0-0.5) is represented by a solid line while dashed lines show the evolution at higher redshifts and are thus not directly comparable to the data. 46
5.15 Comparison of Dfrogin's total baryonic mass (gas + stars) evolution with redshift between all seven runs at 25x resolution. 46
5.16 Evolution of the Dfrogin and Asin target galaxies in the M_*-$R_{\mathrm{HM},*}$ plane at 25x resolution for the different test runs. Also shown are fits to observations by van der Wel et al. 2014 for early type galaxies (solid lines) late types (dashed lines) for redshifts 0 (blue) and 2.75 (red). Note that no test run without UV background was performed for Asin. which is why it is missing in the last panel. 47
5.17 Evolution of the Dfrogin and Asin target galaxies in the M_*-j_* plane at 25x resolution for the different test runs. Also shown are scaling relations for disks, s0 type galaxies, and pure bulges from Teklu et al. 2015. Blue lines indicate where these relations lie at redshift 0, while red lines show them scaled to redshift 2 according to Obreschkow et al. 2015. 48
5.18 H_2 mass evolution with redshift in the target region containing Dfrogin across the seven different variations of resolution and star formation density threshold. Note that while the red and pink lines still correspond to the previous SHDef and SH5 runs respectively, all other colors now represent different simulations than in previous figures. 50

5.19 Dfrogin's H_2 (top) and HI (bottom) mass evolution with redshift for different implementations of the UV background. The dark red line shows the shielding run with the Puchwein et al. 2019 UV background model and the orange line indicates the run using the Faucher-Giguère 2020 model. In addition to the two new models, the SH5 run (with the Haardt and Madau 2012 model) and the test run without any UV background are shown. 51

A.1 Comparison of Asin's molecular hydrogen mass evolution with redshift in the four different runs with the chemical network at 25x resolution. 67
A.2 Comparison of Asin's track in the M_*-M_{H_2} diagram with observations from the COLD GASS survey (Saintonge et al. 2011). The part of the track for each model that lies within the redshift range of the data (0-0.5) is represented by a solid line, while dashed lines show the evolution at higher redshifts and are thus not directly comparable to the data. 68
A.3 Comparison of Asin's track in the M_*-M_{HI} diagram with observations from the xGASS survey (Catinella et al. 2010). The part of the track for each model that lies within the redshift range of the data (0-0.5) is represented by a solid line, while dashed lines show the evolution at higher redshifts and are thus not directly comparable to the data. 68
A.4 Comparison of Asin's neutral atomic hydrogen mass evolution with redshift between all six runs at 25x resolution. 69
A.5 Comparison of the total bound gas mass evolution with redshift in the six different runs of Asin at 25x resolution. 69
A.6 Radial gas density profiles of Asin at selected redshifts on a double log-scale. Each bin contains 200 gas particles. The vertical black line denotes the physical softening for gas particles at that redshift. 70
A.7 Physical density of cold gas in all test runs of Asin from $z = 3$ to $z = 0.13$. Particles colored according to the scale have $T > 10^4$K while gray particles correspond to hot gas. Positions are scaled to the Virial radius, indicated by the black circle, at each redshift. 71
A.8 Phase diagram of gas in all test runs of Asin from $z = 3$ to $z = 0.13$. From top to bottom the models shown are: LTDef, LT5, UMDef, UM5, SHDef, SH5, and SHnoUVB all in the familiar color scheme. The vertical black line denotes the density threshold for star formation in each model assuming the average molecular mass to be 1.22. 72
A.9 Comparison of Asin's star formation rate evolution with redshift between all six runs at 25x resolution. Any data points below the lower limit of the plot correspond to zero star formation in the entire galaxy at that redshift. 73
A.10 Comparison of Asin's track in the M_*-SFR diagram with xGASS and xCOLDGASS data (Catinella et al. 2010, Saintonge et al. 2011). The part of the track for each model that lies within the redshift range of the data (0-0.5) is represented by a solid line while dashed lines show the evolution at higher redshifts and are thus not directly comparable to the data. 73

List of Tables

4.1 Simulation parameter comparison for all Box 4 runs. 23
4.2 Comparison of the total number of galaxies above the mass cut and with zero star formation, as well as the number of quiescent galaxies and the corresponding quenched fraction, between all four simulations at redshift 2. The criterion for quiescence, SSFR/$H(z) < 0.3$, was adapted from Franx et al. 2008. 28

5.1 Simulation parameter comparison for the different model implementations in the cosmological zoom-in runs of Dfrogin at the 25x resolution. 33
5.2 Dark matter and gas particle masses and default star formation density threshold in the four resolution levels of the study. 49

A.1 Simulation parameter comparison for the different model implementations in the cosmological zoom-in runs of Asin at the 25x resolution. 67

Appendix A

Asin

Simulation Name	**LTDef**	**LT5**	**UMDef**	**UM5**	**SHDef**	**SH5**
Chemical Network	No	No	Yes	Yes	Yes	Yes
UV Background	Yes	Yes	Yes	Yes	Yes	Yes
Shielding	No	No	No	No	Yes	Yes
SF Threshold [cm^{-3}]	2.0	5.0	2.0	5.0	2.0	5.0

Table A.1: Simulation parameter comparison for the different model implementations in the cosmological zoom-in runs of Asin at the 25x resolution.

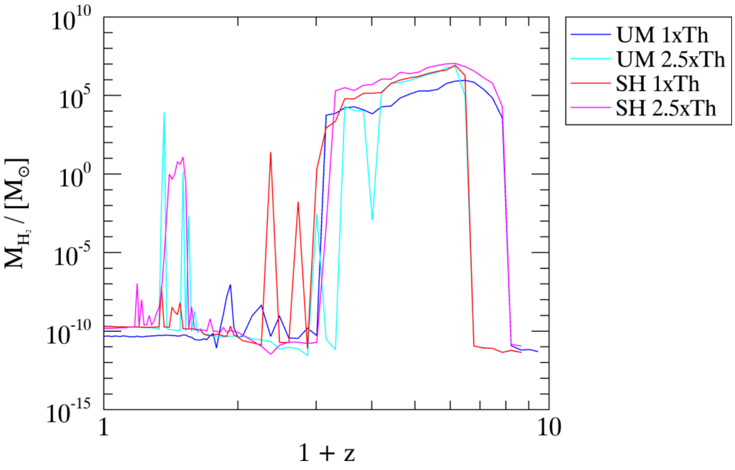

Figure A.1: Comparison of Asin's molecular hydrogen mass evolution with redshift in the four different runs with the chemical network at 25x resolution.

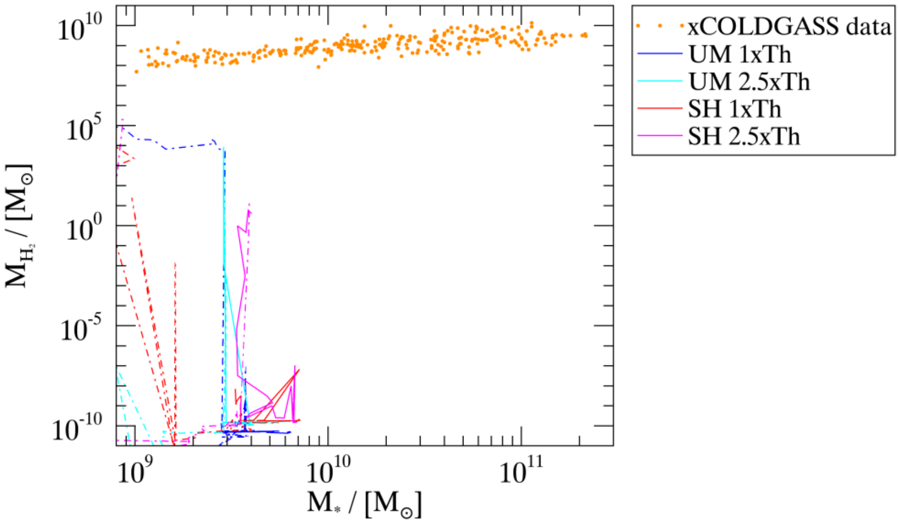

Figure A.2: Comparison of Asin's track in the M_*-M_{H_2} diagram with observations from the COLD GASS survey (Saintonge et al. 2011). The part of the track for each model that lies within the redshift range of the data (0-0.5) is represented by a solid line, while dashed lines show the evolution at higher redshifts and are thus not directly comparable to the data.

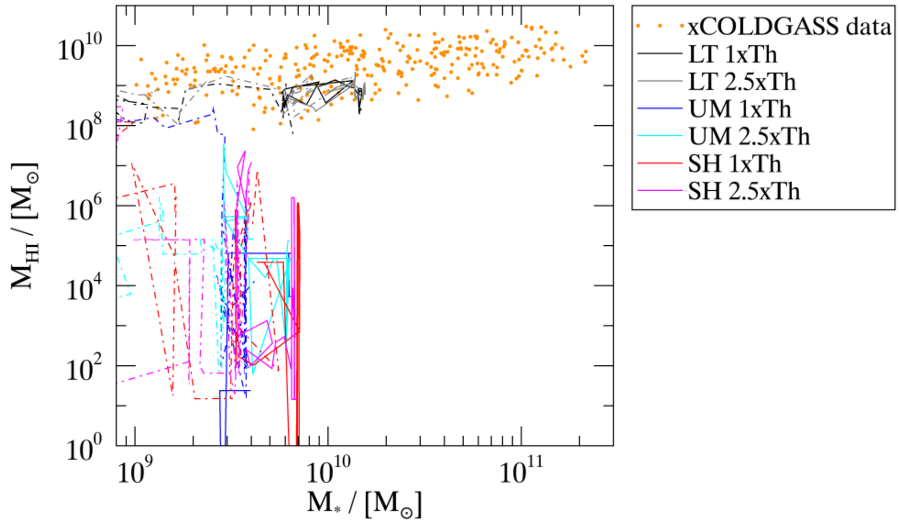

Figure A.3: Comparison of Asin's track in the M_*-M_{HI} diagram with observations from the xGASS survey (Catinella et al. 2010). The part of the track for each model that lies within the redshift range of the data (0-0.5) is represented by a solid line, while dashed lines show the evolution at higher redshifts and are thus not directly comparable to the data.

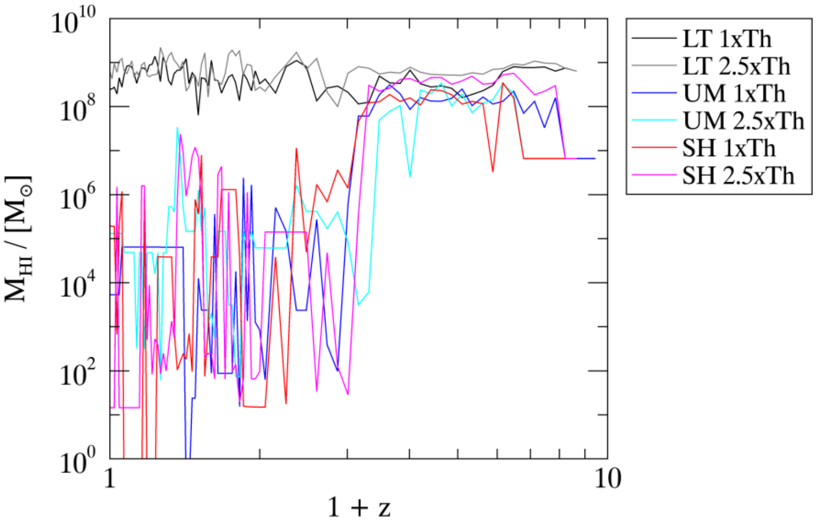

Figure A.4: Comparison of Asin's neutral atomic hydrogen mass evolution with redshift between all six runs at 25x resolution.

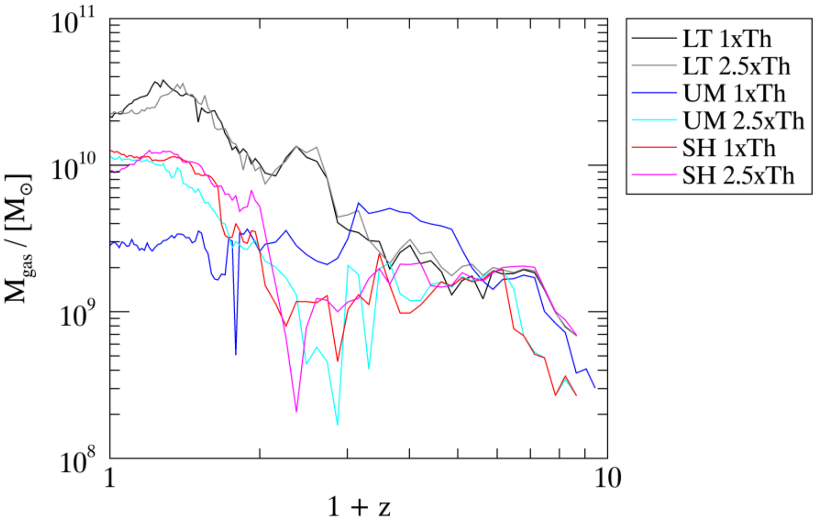

Figure A.5: Comparison of the total bound gas mass evolution with redshift in the six different runs of Asin at 25x resolution.

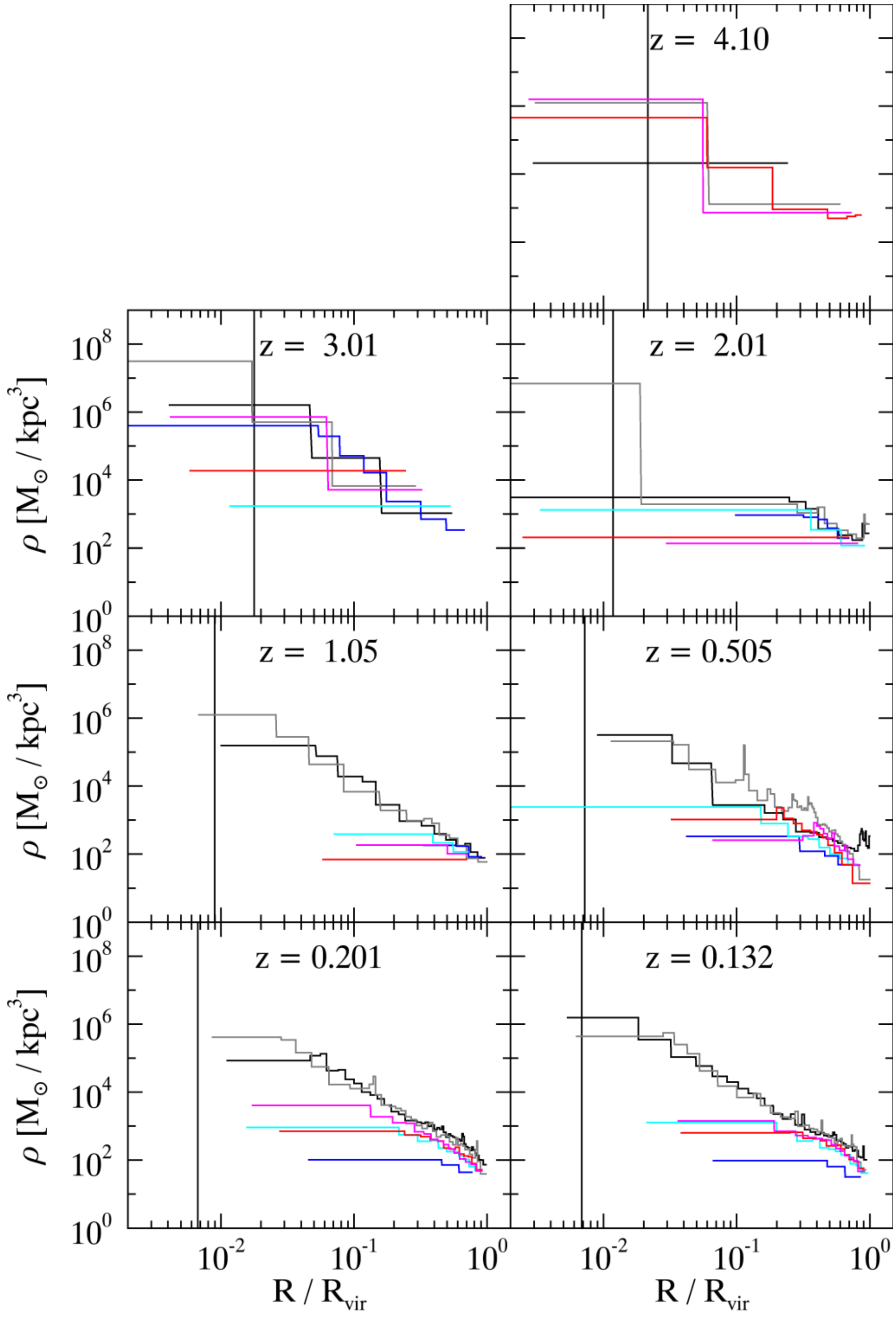

Figure A.6: Radial gas density profiles of Asin at selected redshifts on a double log-scale. Each bin contains 200 gas particles. The vertical black line denotes the physical softening for gas particles at that redshift.

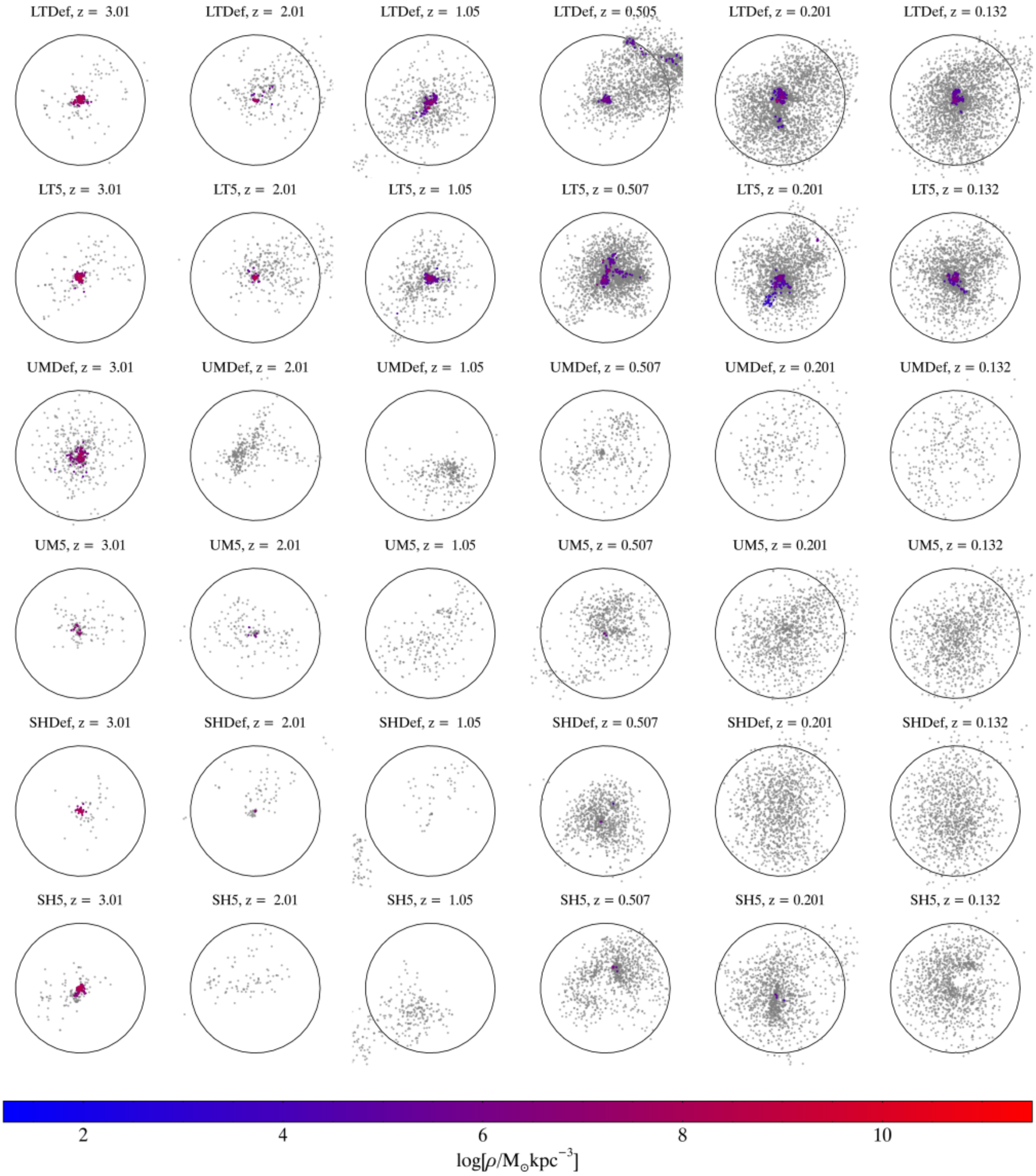

Figure A.7: Physical density of cold gas in all test runs of Asin from $z = 3$ to $z = 0.13$. Particles colored according to the scale have $T > 10^4$K while gray particles correspond to hot gas. Positions are scaled to the Virial radius, indicated by the black circle, at each redshift.

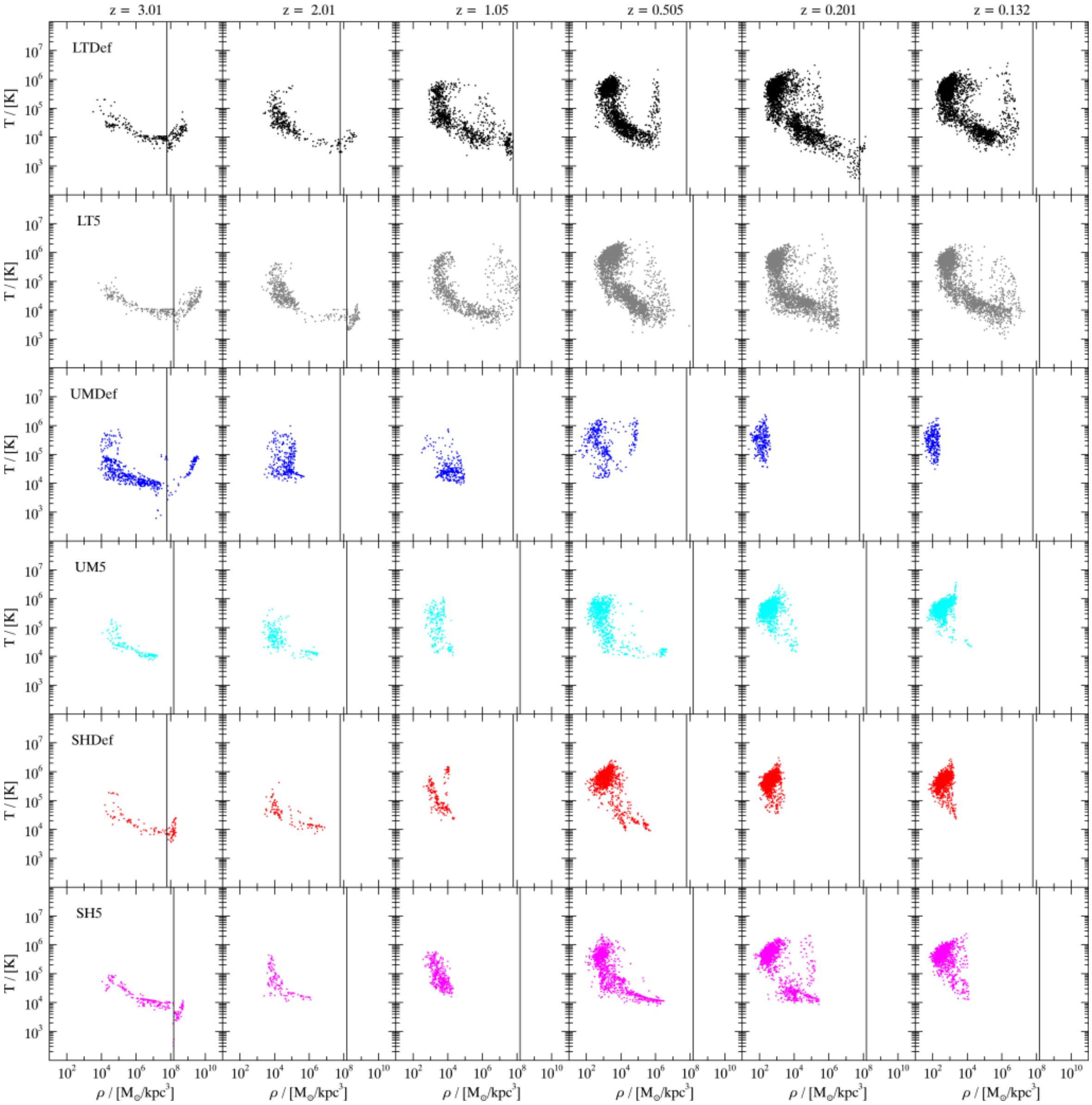

Figure A.8: Phase diagram of gas in all test runs of Asin from $z = 3$ to $z = 0.13$. From top to bottom the models shown are: LTDef, LT5, UMDef, UM5, SHDef, SH5, and SHnoUVB all in the familiar color scheme. The vertical black line denotes the density threshold for star formation in each model assuming the average molecular mass to be 1.22.

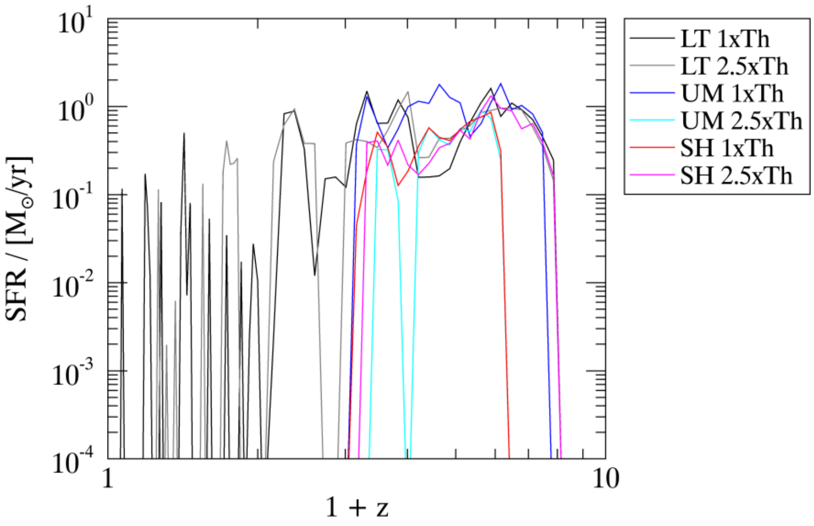

Figure A.9: Comparison of Asin's star formation rate evolution with redshift between all six runs at 25x resolution. Any data points below the lower limit of the plot correspond to zero star formation in the entire galaxy at that redshift.

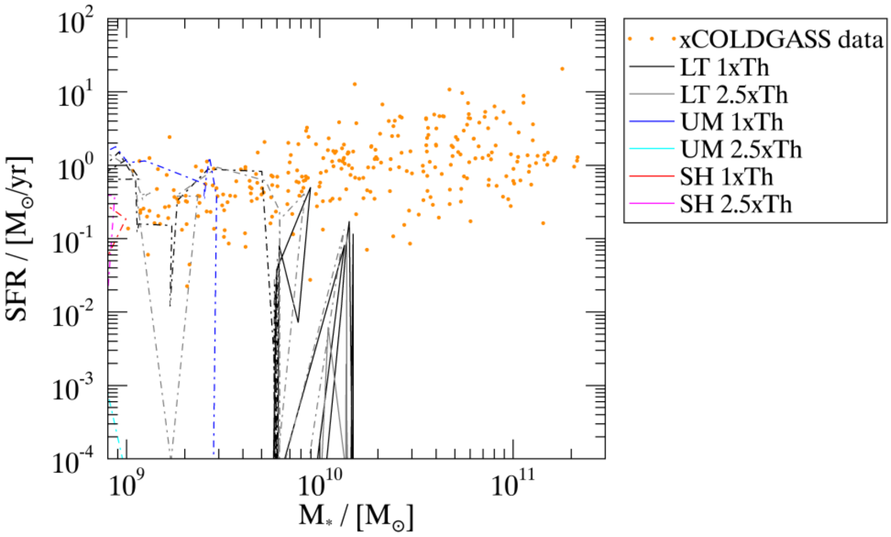

Figure A.10: Comparison of Asin's track in the M_*-SFR diagram with xGASS and xCOLDGASS data (Catinella et al. 2010, Saintonge et al. 2011). The part of the track for each model that lies within the redshift range of the data (0-0.5) is represented by a solid line while dashed lines show the evolution at higher redshifts and are thus not directly comparable to the data.

Acknowledgements

I would like to thank Klaus Dolag and Rhea-Silvia Remus for offering me this project and bringing me into the CAST group, and for managing to create a functioning and enjoyable work environment amidst a global pandemic. Many thanks to Umberto Maio, who wrote the very code on which this work is based, and who provided valuable input on many a Friday morning throughout the entire process. I am grateful also to Milena Valentini, who never missed a meeting and always gave good advice.

Really, I have to thank all of the CAST group members who congregated in our coffee chats; I am sure everyone of you helped me with at least one of the less fun technical problems or the more fun scientific questions I faced during this time. Special thanks to the Galaxies group for helpful and entertaining discussions, scientific, political, and otherwise philosophical.

From the bottom of my heart I want to thank Louisa, partly for proofreading the whole thing, but mainly for being here with me. And last but not least, I would like to give my thanks to my family and to all my friends, new and old, for their support and diversions.

Selbständigkeitserklärung

Ich versichere hiermit, die vorliegende Arbeit mit dem Titel

Evolution and Dynamics of Cold Gas in Simulated Galaxies

selbständig verfasst zu haben und keine anderen als die angegebenen Quellen und Hilfsmittel verwendet zu haben.

Jan Bendix Hagedorn

München, den 15. April 2021